CHALMERS
UNIVERSITY OF TECHNOLOGY

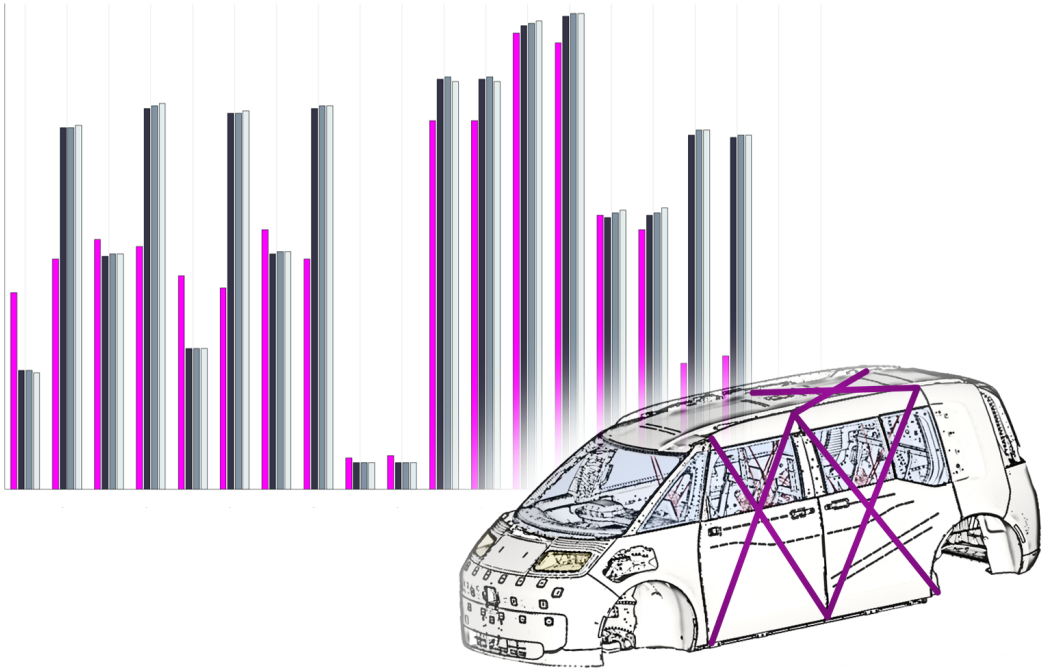

Parameter Study on a Fully Trimmed Body

Opening Distortion Fingerprint of a Finite Element Model imported to Multibody Dynamics through a Modal Neutral File Compared to Test Data

Master's thesis in Applied Mechanics

LISA LINDKVIST
EMMA OLGER

DEPARTMENT OF MECHANICS AND MARITIME SCIENCES

CHALMERS UNIVERSITY OF TECHNOLOGY
Gothenburg, Sweden 2025
www.chalmers.se

Master's Thesis in Applied Mechanics

Parameter Study on a Fully Trimmed Body

Opening Distortion Fingerprint of a Finite Element Model imported to Multibody Dynamics through a Modal Neutral File Compared to Test Data

LISA LINDKVIST
EMMA OLGER

CHALMERS
UNIVERSITY OF TECHNOLOGY

Department of Mechanics and Maritime Sciences
Division of Dynamics
Chalmers University of Technology
Gothenburg, Sweden 2025

Parameter Study on a Fully Trimmed Body
Opening Distortion Fingerprint of a Finite Element Model imported to Multibody Dynamics through a Modal Neutral File Compared to Test Data
LISA LINDKVIST
EMMA OLGER

Industrial Supervisors: Jens Weber and Pravin Ugale, Zeekr Technology Europe
Supervisor: Håkan Johansson, Mechanics and Maritime Sciences
Examiner: Petri Piiroinen, Mechanics and Maritime Sciences

Master's Thesis 2025
Department of Mechanics and Maritime Sciences
Chalmers University of Technology
SE-412 96 Gothenburg
Sweden
Telephone +46 31 772 1000

Cover: Finite element model of the robot-taxi along with an opening distortion fingerprint with different number of degrees-of-freedom.

Typeset in LaTeX
Gothenburg, Sweden 2025

Parameter Study on a Fully Trimmed Body
Opening Distortion Fingerprint of a Finite Element Model imported to Multibody Dynamics through a Modal Neutral File Compared to Test Data
LISA LINDKVIST
EMMA OLGER
Department of Mechanics and Maritime Sciences
Division of Dynamics
Chalmers University of Technology

Abstract

A complete vehicle model in a multibody dynamics simulation is considered constituting a key enabler for virtual development within the automotive industry. In collaboration with Zeekr Technology Europe, a multibody dynamics model of a robot-taxi has been studied. The multibody dynamics model includes a so-called fully trimmed body of a finite element model through a so-called modal neutral file. In particular, the opening distortion fingerprint consisting of diagonals over body openings and cross-sections, has been used as a measure to evaluate how well the simulation model correlate to test data. The main topic of this master's thesis has been to perform a parameter study in order to investigate what parameters affect the correlation.

In addition to simulations, a literature review has been conducted in order to understand the impact from the parameters related to the modal neutral file. From the literature review, examples of component mode synthesis by Guyan and Craig-Bampton on a beam are presented. The examples illustrate that the definition of the interface between the finite element model and the rigid components as well as the modes included in the synthesis have an impact on how well eigenpairs can be represented. Additionally, a physical beam has been utilized in order to understand the impact from rigidbody motions in simulations and on test data. The physical beam example illustrates that the accelerometers used measure the gravity field when being rotated. These rotations must be taken into account for lower frequencies.

The outcomes of the parameter study are that the diagonals over the side doors and the A-pillar section show a poor correlation to the test data, while the remaining diagonals show a similar fingerprint to the one obtained from the test data. Furthermore, none of the studied parameters has shown a significant impact on the fingerprint over the side doors. Nevertheless, the considered frequency range used to obtain the fingerprint has shown to impact the correlation over the side doors. However, all diagonals require further investigation for the fingerprint to be correlated. The further investigation may include a review of the simulation models, a study on combined parameter effects, studying animations of the eigenmodes, dive deeper into the component mode synthesis or review the parameter settings, in particular the frequency range, of the fingerprint.

Keywords: Opening Distortion Fingerprint (ODF), Component Mode Synthesis (CMS), E-line method, Modal Neutral File (MNF), Multibody Dynamics (MBD), solidity, MSC Nastran, MSC Adams, fully trimmed body.

Preface

After studying Mechanical engineering with a master's in Applied Mechanics, this thesis, carried out at the Department of Mechanics and Maritime Sciences at Chalmers University of Technology during the spring of 2025, is the grad finale to our years as students at Chalmers. In this report, the outcome of our master's thesis project is presented.

Conducting the thesis, we have gained understanding of how the theory we have learned over the past few years can be turned into practical examples and applications. In particular, we have through a literature review, gained understanding of component mode synthesis and how it can be used in practice, and we hope that this understanding is mirrored in the report. Additionally, we hope that the report may help other students with examples of how the taught theory for structural mechanics may be used in industry.

Furthermore, it has been interesting to work with an industrial company and being at the forefront of computer aided engineering in the automotive industry. Throughout the spring, we have seen an interest in the project from various representatives from the industry. Before starting the thesis, we would never have thought that this interest would be large enough for us to present parts of our findings at the *10th Before Reality Conference* in Munich, but, yet we were accepted! Presenting at the conference will constitute an unexpected cherry on top of our educational journey as master's students at Chalmers.

Acknowledgements

First, we would like to express our appreciation to our supervisors at Zeekr Technology Europe, Jens Weber, *Principal Technical Expert Solidity*, and Pravin Ugale, *Technical Expert - Road Load Data & MDO*, for supporting and guiding us during the thesis. Your feedback and openness to questions at all times have been invaluable.

A special thank you to our examiner at Chalmers University of Technology - Associate Professor Petri Piiroinen at the department of Mechanics and Maritime Sciences, Chalmers University of Technology - for your continuous check ins and feedback. We also want to thank Professor Håkan Johansson at the department of Mechanics and Maritime Sciences, Chalmers University of Technology, for your insights and feedback on the process.

To the team at Zeekr, thank you for creating a collaborative environment with positiveness and inclusiveness. Lastly, to the people at BETA CAE Systems and Hexagon, thank you for the support throughout the project.

Lisa Lindkvist, Emma Olger, Gothenburg, May 2025

List of Acronyms

Below is the list of acronyms that have been used throughout this thesis listed in alphabetical order:

2D	Two dimensional
ACMS	Automated Component Mode Synthesis
AI	Artificial Intelligence
APsa	A-Pillar section a
APsb	A-Pillar section b
BPsa	B-Pillar section a
BPsb	B-Pillar section b
CAE	Computer Aided Engineering
CEVT	China Euro Vehicle Technology
CMS	Component Mode Synthesis
CO_2	Carbon-dioxide
CPsa	C-Pillar section a
CPsb	C-Pillar section b
DOF	Degree of Freedom
DOFs	Degrees of Freedom
DPsa	D-Pillar section a
DPsb	D-Pillar section b
EV	Electric Vehicle
EVs	Electric Vehicles
EVP	EigenValue Problem
Enga	Engine/front a
Engb	Eingine/front b
FE	Finite Element
FEM	Finite Element Method
FDla	Front Door left a
FDlb	Front Door left b
FDra	Front Door right a
FDrb	Front Door right b
FFT	Fast Fourier Transform
IRS	Improved Reduction System
LHS	Left Hand Side

MBD	Multi Body Dynamics
MAC	Modal Assurance Criterion
MNF	Modal Neutral File
MNFs	Modal Neutral Files
MSS	Multi Stethoscope
N/A	Not Applicable
NaN	Not a Number
NVH	Noise Vibration and Harshness
ODF	Opening Distortion Fingerprint
ODFs	Opening Distortion Fingerprints
ODS	Operational Deflection Shape
ppm	Parts Per Million
RB	Rigid Body
RBM	Rigid Body Mode
RBMs	Rigid Body Modes
RDla	Rear Door left a
RDlb	Rear Door left b
RDra	Rear Door right a
RDrb	Rear Door right b
REEs	Rare Earth Elements
SEA	Sustainable Experience Architecture
SDE	Structural Dynamics Equation
SEP	Statistical Evaluation Parameter
SEREP	System Equivalent Expansion Reduction Process
SOL	SOLution sequence
SRa	Sun Roof a
SRb	Sun Roof b
UN	United Nations

Nomenclature

Below is the nomenclature of indices, sets, parameters, and variables that have been used throughout this thesis.

Indices

i,j	Indices related to specific eigenvalues, eigenvectors or elements
a,b	Indices related to set definitions
p	iteration index
t	Time

Sets

ASET	Set of interface degrees of freedom
BSET	Set of internal degrees of freedom

Conventions

$\hat{\bullet}$	Discrete FE approximation of $\bullet$
$\bullet^{-1}$	Inverse of $\bullet$
$\tilde{\bullet}$	Discrete approximation of $\bullet$ through CMS
$\bar{\bullet}$	Reordered version of $\bullet$
$\dot{\bullet}$	First time derivative of $\bullet$
$\ddot{\bullet}$	Second time derivative of $\bullet$
$\mathfrak{Re}\left\{\bullet\right\}$	Real part of $\bullet$
$:=$	Equal per definition

Parameters

e	Euler's number
i	Imaginary unit
ρ	Density
E	Young's modulus

I_z	Area moment of inertia
L	Total length
O	Origin
δ, Δ, $d\bullet$	Difference in distance
λ	Eigenvalue
$\boldsymbol{M}$	Mass matrix
$\boldsymbol{K}$	Stiffness matrix
$\boldsymbol{u}$	Continuous displacement vector

Variables

l	Elment length
A	Area
$\boldsymbol{q}$	Approximate displacement vector
q	Generalized degree of freedom
ω	Eigenfrequency
$\boldsymbol{\varphi}$	Eigenmode
$\boldsymbol{\Phi}$	Mode matrix
$\boldsymbol{\Omega}$	Collection of eigenfrequencies

Contents

List of Figures

List of Tables

1

Introduction

This master thesis is a collaboration between Chalmers University of Technology (Chalmers) and Zeekr Technology Europe (Zeekr), where a parameter study on a simulation model of a robot-taxi is performed. In this chapter an introduction to the project is given, starting with a background of the scope. Thereafter, a flow chart is presented as a guide on how the simulation is performed, the purpose of the study is stated and the goals of the project are set. Lastly, the demarcations of the project are stated together with ethical aspects that may be needed to consider.

1.1 Background

Zeekr, previously known as China Euro Vehicle Technology (CEVT), is a luxury electric vehicle (EV) brand owned by Geely Holding Group [32]. A new sustainable experience architecture (SEA) platform, the SEA-M platform, was developed by the company in 2022. This platform is built for shared autonomous vehicles. Apart from being a collaboration between Zeekr and Waymo, the first vehicle on the platform is a so-called robot-taxi [31]. This robot-taxi has no B-pillar, in contrast to a traditional vehicle. For an illustration of the typical location of the B-pillar, see Figure 1.1. During the development process that started in 2017, a virtual model has been established. This virtual model is meant to constitute a digital twin of the taxi. The current aim is to correlate this virtual model with test data of a test vehicle representing the robot-taxi.

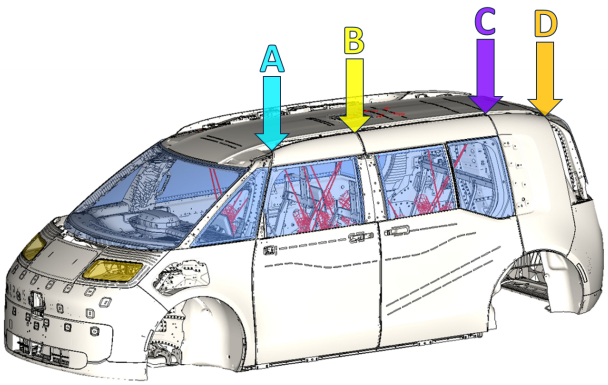

Figure 1.1: The robot-taxi with the typical positions of the A-, B-, C-, and D-pillars highlighted.

In general, a complete vehicle model in a multibody dynamics (MBD) simulation is a key enabler for virtual development in the automotive industry. Due to the wide range of available load cases, this type of simulation delivers data to a number of different computer aided engineering (CAE) disciplines such as durability, solidity, noise vibration and harshness (NVH), and vehicle dynamics. A complete vehicle model is very complex and contains many advanced features like the tire representation including the road profile contact, nonlinear bushings and damper characteristics, bump stops and the flexible model of a fully trimmed body. Therefore it is important to capture this complexity through correlation between simulation model and test vehicle.

Figure 1.2: Example of Belgian pavé [24].

For this master thesis, rigid body (RB) and finite element (FE) models of the robot-taxi, originating from the SEA-M platform, are available. The capability of the existing FE and MBD models of the robot-taxi are continuously improved by correlating test results with simulations. In order to further improve the correlation to test data a major test, working as a reference for the correlation study, has been performed on the robot-taxi. During the test, the response of the body, the side doors and the rear subframe were measured when driving on different test tracks such as Belgian pavé, see Figure 1.2. More than 30 accelerometers were placed on the vehicle. With these accelerometers the distortion in all body openings were measured using the multi stethoscope (MSS) method (Weber, J., personal communication, January 28, 2025). The distortion has been determined from the measurements in each opening with two diagonals, see red diagonals in Figure 1.3.

Up until the start of the thesis work, the FE model has been analyzed in an FE software by measuring the distortion through a MSS [38]. The MSS considers two diagonals per carbody opening [37], see Figure 1.3. The time history of the distortion from the MSS has been sorted in descending order and a mean value of a userdefined percentage of the highest values has been evaluated [38]. This mean value for each diagonal is shown in a bar plot, and this bar plot constitutes the opening distortion fingerprint (ODF). It has previously been established that in this context, a portion of 20-30 percent of the values is appropriate [37]. The foundation for the master thesis is to analyze the digital twin of the robot-taxi, with MSS, in an MBD software.

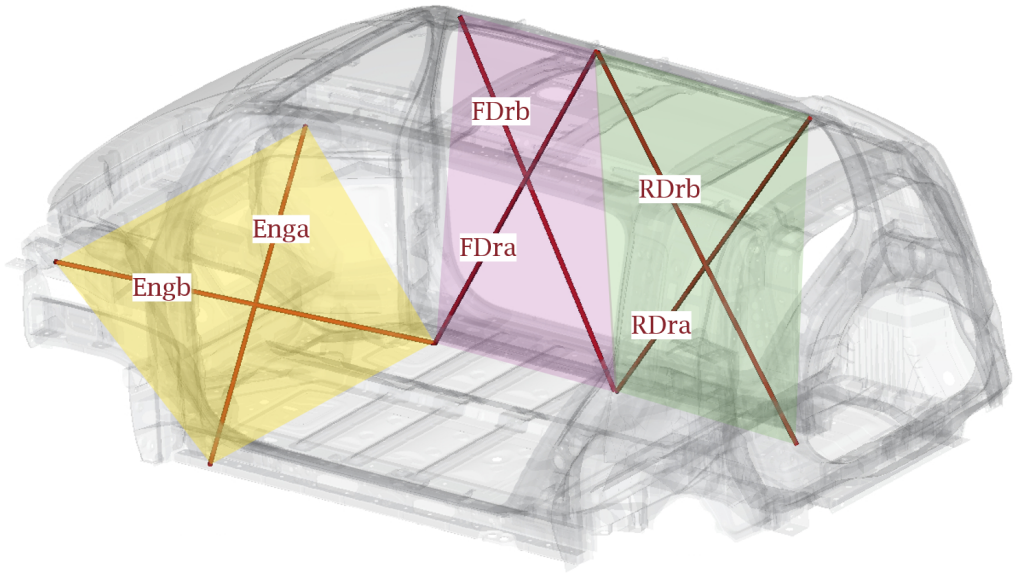

Figure 1.3: Example of multi stethopscope diagonals over the robot-taxi.

Importing the FE model of a simplified body without MSS, into MBD, has been done before by exporting the FE model as a modal neutral file (MNF) [38]. One novel aspect of the thesis is that the MNF model represents a fully trimmed body model including the MSS. A fully trimmed body model is a model including all key features in the compartment, such as the seats and the steering wheel. The MNF originates from an existing FE model consist of more than five million elements, where each element is of order $1 \cdot 10^{-3}$ m. Another new aspect is that the MSS results are correlated with test data. The excitation has previously been applied in the FE

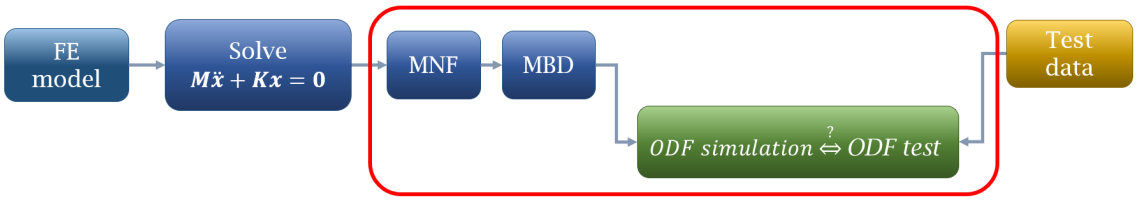

Figure 1.4: Parameter study flow chart. In the second step $\boldsymbol{M}$ and $\boldsymbol{K}$ denote the mass and stiffness matrices of the FE model of the fully trimmed body.

environment, but with this new setup it will be applied in the MBD environment. This virtual model should be even closer to reality by including e.g. gravity, contact between the tires and the road profile, and all chassis components with their non-linear characteristics. The red rectangle in the flow chart in Figure 1.4 presents the new aspects treated in the thesis. The overall evaluation steps includes processing and solving of the FE model, condensing the FE model into an MNF which is an input into the MBD simulation, and lastly comparing the results to test data.

1.2 Purpose

The purpose of the master thesis is to perform a comprehensive parameter study and investigate what parameters that affect the correlation between the test and simulation results. The main criterion to asses the impact of a certain parameter is the distortion in all body openings using ODF.

1.3 Goals

In order to ensure the ability of identifying parameters that may affect the correlation, a deeper understanding of the theory behind the MNF creation is crucial. Furthermore, a thorough understanding of the ODF evaluation method is essential in order to assess whether the results correlate, and thereby assess whether the purpose is fulfilled. Hence, the following preparatory goals are defined:

a. Investigate component mode synthesis (CMS) that is the basis of MNF creation,

b. Gain understanding of the numerical methods used by the solvers,

c. Gain understanding of the numerical methods used during post-processing.

In addition to the preparatory goals, defined goals regarding the parameter study are:

d. Study the impact of at least five parameters,

e. State whether each studied parameter has an impact on the correlation or not,

f. Identify parameters with major impact on the correlation.

1.4 Demarcations

This thesis only considers correlation between existing test data and the virtual MBD model in MSC Adams (hereafter referred to as Adams) [19] describing the robot-taxi. The meshing of the models are kept during the parameter study. Only the FE model of the fully trimmed body is transformed into modal neutral files (MNFs), which are considered for the correlation study. The FE model is only studied in the pre-processor Ansa [2] and the post-processor Meta [3], where the solver MSC Nastran (hereafter referred to as Nastran) [23] is used. The damping is applied as modal damping in the MBD environment. In addition to this, only the velocity of the vehicle and the tire models may be changed in the MBD environment.

Additionally, the correlation study considers ODF only for evaluation between the virtual model and the test data. Therefore, only the so-called E-line method used in the ODF tool is considered. For the parameter study, only the z-component of the E-line method is considered. The frequency response is limited by upper and lower

frequency limits of the accelerometers used in the test. In Adams, the car model is only driven clockwise on Belgian pavé for 25 seconds with existing driver and road models. Simulation results are then compared with the existing data for Belgian pavé from Hällered Proving Ground, Sweden. The thesis work has been conducted during 20 weeks between January and June 2025.

1.5 Ethical aspects

In relation to any project, it is important to be aware of possible ethical concerns. The most important consideration is that the work should be of benefit for people, in accordance to the guidelines from Chalmers [7]. Zeekr has a vision of supporting diversity, transparency and sustainability [39], which should minimize the risk of unethical steps in the supply chain and be in line with working towards the UN goals [34] 5 (equality), 8 (decent working conditions), 9 (sustainable industry), and 11 (sustainable societies). In relation to the robot-taxi studied in this thesis work, the robot-taxi is meant to be of transportational benefit for people, which is in line with Chalmers' guidelines. Furthermore, the robot-taxi is meant to become autonomous in a few years, which implies further benefits for people as well as additional ethical considerations.

Self-driving vehicles are predicted to be of benefit for people since the human factor is estimated to cause about 95% of all vehicle accidents on European roads [11]. Removing the human factor could reduce the number of accidents and thereby improve road safety. If, however, an autonomous vehicle would be involved in a road accident it is important to consider liability in relation to the accident. Another important consideration regarding autonomous vehicles is that they must be able to respect human dignity and freedom of choice [11], which could violate the road safety and reasoning regarding responsibility.

In order to treat ethical concerns in relation to artificial intelligence (AI), which is used by autonomous vehicles, guidelines have been developed by the European Commission [10]. These guidelines state that AI systems should empower human beings, be resistant and secure, respect privacy, be transparent, non-discriminatory and fair as well as be of benefit for all human beings including future generations. Furthermore, the responsibility and accountability of the vehicle should be accounted for [10]. If these guidelines are fulfilled, it can be considered ethically motivated to use AI for autonomous vehicles. Training an AI requires large datasets and such datasets could be influenced by biases in terms of data collection, labeling and algorithms. There are methods to reduce biases in datasets using AI [8], but it is important to keep in mind that some techniques use AI to reduce the bias, which implies that the expertise of AI must be trusted. In turn, this could contradict the purpose of using AI to remove biases in large data sets.

Even though ethical concerns of AI used for autonomous vehicles are important and relevant, the robot-taxi treated in this thesis work is currently non-autonomous and therefore the ethical concerns of the datasets for autonomous driving is beyond the topic of this thesis. However, in line with the ethical guidelines of the European

Commission [10] and the regulations from Chalmers [7], transparency of the use of AI is crucial. Consistent with the guidelines and recalling that AI should be used for human benefit, the use of AI for the thesis has been limited to proposals of re-phrasing sentences and locating built-in functions in the programming languages Matlab and Python. More information on the use of AI is presented in section 4.4.

Apart from the ethics of AI, ethics regarding the vehicle itself can be discussed. Electric vehicles (EVs), such as the robot-taxi, could reduce the emissions of carbon-dioxide (CO_2) [9] and thereby contribute to the United Nations (UN) goal number 13 of fighting the climate change [34]. Working towards the thirteenth goal and towards reducing the CO_2-emissions is considered to be be of benefit for people and thereby ethical according to Chalmers's regulations, even though the batteries require so-called rare earth elements (REEs). The REEs are seldom found in concentrated deposits, which is challenging from an environmental point of view. In addition to this, there are only a few providers dominating the global supply chains [26], which could be problematic from an availability perspective. It is also important to mention that the way in which electricity is produced has an impact on the environmental benefits and reduction of CO_2 emissions of an EV. In the context of electricity, the electricity used during the research and development of the vehicle can also be mentioned. However, the production of electricity is also considered to be outside the scope of this thesis.

Furthermore, the thesis work include ethical obligations to ensure accuracy and reliability of simulation results and test data. Manipulation of the test data in order to receive a better correlation would be unethical in the sense that it could benefit the company in the short run. In the long run, manipulated results could imply incorrect dimensioning of the vehicle, and in worst case failure of critical components, which would violate the safety and put humans in danger. Biases and fairness in the criteria used to evaluate the model should also be taken into consideration. One method for evaluating parts of the model may not be fair for the whole model, or only show a certain response that is not necessarily representative in a bigger perspective.

Misunderstandings are less likely to happen when clearly stating the conclusions of the results and how the results are obtained. Clarity in conclusions and results also allow for re-creations of results, i.e if it is possible to obtain similar results in other settings, the reliability of the study increases, and therefore also the trustworthiness. Lastly, to ethically account for the results is also important. If errors in calculations or assumptions are found after the study, the models need to be updated in order to be as accurate as possible.

2

Theory

As mentioned in the purpose and goal sections, a deeper understanding of the methods used for the study is needed. Hence, the theory chapter starts with an introduction of bodies and an introduction on how structures can be modeled. Thereafter, CMS is reviewed together with how it may be used in Nastran and how an MNF is created. The damping modeling used in Adams is described and lastly, the ODF measure is studied.

2.1 Describing bodies in motion

In simulations and analytical calculations, bodies can be described as rigid or flexible. The difference constitutes of whether the body itself deforms or not. A body can also be described in different coordinate frames, which is important to consider when the body rotates or translates.

2.1.1 Rigid bodies

In order to simplify the modeling of motions and forces, bodies are assumed to be rigid. A rigid body (RB) is created by assuming that the body is unable to deform when exposed to forces, i.e the body cannot be stretched, compressed or bent [28, 25]. Two points in an RB are assumed to be equidistant when the RB is exposed to rotation or translation [28]. The possible rotations are about each axis, and the possible translations are along each axis. The translations and rotations constitute the six degrees of freedom (DOFs) an RB can move in. The RB assumption can be used for simulation of smaller parts in a bigger system where the deformation is negligible in comparison to the deformation of other parts. Another option is to use the RB assumption for multiple parts in a system to observe the general behavior.

2.1.2 Flexible bodies

In contrast to a RB, a flexible body allows points within the body to move relative to each other. One enabler for representing a flexible body is the finite element method (FEM), where the body is divided into smaller elements in a process referred to as discretization or meshing. Introducing flexible bodies in an MBD simulation, such

as Adams, can increase the credibility of the simulation. A flexible body can either be created in Adams or be imported as a so-called MNF [16], as in this thesis.

2.1.3 Coordinate frames

To express the position of a body or system in space, coordinate frames must be introduced as a reference for angular and translational measurements. A frame of reference that is assumed to have no rotation or translation in space, is the primary inertial frame or astronomical frame of reference. The primary inertial frame includes the basic framework for Newton's laws of mechanics that constitutes the basic laws of physics. A reference frame assumed to be still in space is considered to be fixed, and is also called a global coordinate frame. Measurements made with respect to a global coordinate frame are considered to be absolute [28, 25].

Coordinate frames can also be local. A local coordinate frame is allowed to rotate arbitrarily and translate with a constant velocity, below the speed of light, with respect to a global coordinate frame. This can be shown using so-called Galilean transformations [6, 25]. From Galilean transformations, the so-called Galilean relativity gives that the governing laws of all fundamental motions, including Newton's laws, are equal in all coordinate frames related to each other [6]. Using the so-called Lorentz transformation, it can be shown that a local coordinate frame is valid regardless of speed [6].

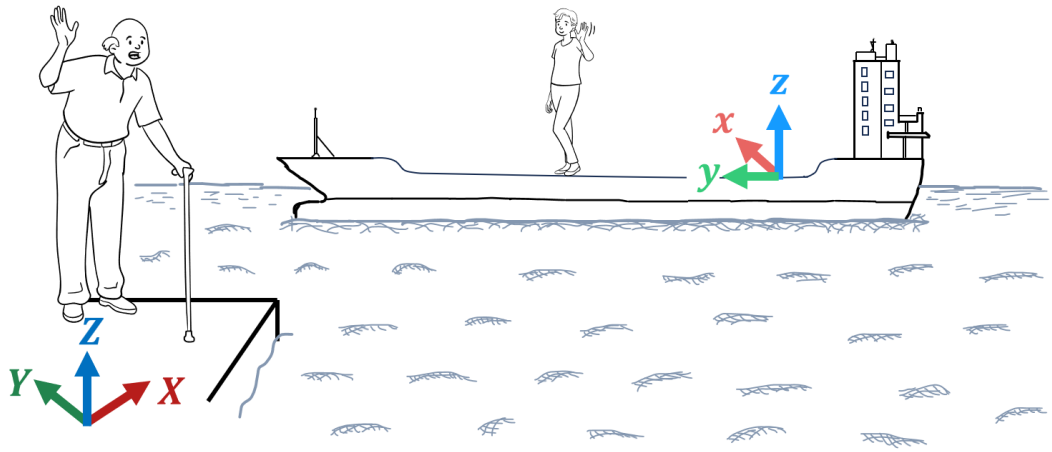

Figure 2.1: Example of a global coordinate system denoted with uppercase letters on the dock, and a local coordinate system denoted with lowercase letters on the tanker.

An example of the difference between a global fixed coordinate frame and a local body-fixed coordinate frame is the different perspectives on a moving tanker, see illustration in Figure 2.1. In the figure, the global coordinate frame is placed at the dock and the local coordinate frame is located at the moving tanker. If a passenger on the tanker is walking, the passenger will move relative to the tanker. If a person looks at the tanker from the dock, the person will perceive the moving passenger

with a velocity higher than the passenger is perceiving its own velocity. This comes from that the by-standing person perceives the velocity of the tanker in addition to the velocity at which the passenger is walking. The passenger, on the other hand, perceives a motion with respect to a local coordinate frame placed on the tanker. Constantly looking at the dock while walking, the passenger perceives a higher or lower velocity depending on whether the walk is forward or backward on the tanker.

2.1.4 Rotational matrices

For mathematical representations of rotations in a body, for example a car, rotations are specified about an axis which can be body-fixed (local) or space-fixed (local or global depending on the context). For a body-fixed coordinate frame in three dimensions, a rotation causes the local coordinate frame to rotate with respect to the global frame. Consequently, if a body rotates about the x-axis and then the new y-axis, the resulting coordinates of the body will differ between the space-fixed (global) and body-fixed (local) coordinate frames [5].

In order to understand the phenomenon of rotation, an example i performed starting in two dimensions with a rotation about the Z-axis, see angle φ in Figure 2.2. In the figure, uppercase letters represent the original axes and the lower case letters represent the deformed system. The new base vectors describing the coordinate system after rotation becomes [5]

$$\begin{aligned} \boldsymbol{e}_x &= \cos(\varphi)\boldsymbol{e}_X + \sin(\varphi)\boldsymbol{e}_Y, \\ \boldsymbol{e}_y &= -\sin(\varphi)\boldsymbol{e}_X + \cos(\varphi)\boldsymbol{e}_Y \end{aligned} \tag{2.1}$$

where φ denotes the rotational angle and $\boldsymbol{e}_X$ and $\boldsymbol{e}_Y$ denote the original base vectors. Om matrix form, the new base vectors $\boldsymbol{e}_x$ and $\boldsymbol{e}_y$ can be described as

$$\begin{bmatrix} \boldsymbol{e}_x \\ \boldsymbol{e}_y \end{bmatrix} = \underbrace{\begin{bmatrix} \cos(\varphi) & \sin(\varphi) \\ -\sin(\varphi) & \cos(\varphi) \end{bmatrix}}_{=R_\varphi} \begin{bmatrix} \boldsymbol{e}_X \\ \boldsymbol{e}_Y \end{bmatrix} \tag{2.2}$$

the rotational matrix is here called R_φ with the subscript denoting the rotational angle.

Since there is only one axis to rotate around in two dimensions, the rotational order is insignificant. If the system rotates with the angles φ_1 and φ_2, the total resulting rotation is $\varphi = \varphi_1 + \varphi_2$. The rotational matrix is commutable, i.e $R_\varphi = R_{\varphi_1} R_{\varphi_2} = R_{\varphi_2} R_{\varphi_1}$ [5].

In three dimensions, the rotational matrices, where the subscript represent the axis of rotation, are described as [5]

$$R_X(\theta_X) = \begin{bmatrix} 1 & 0 & 0 \\ 0 & \cos(\theta_X) & \sin(\theta_X) \\ 0 & -\sin(\theta_X) & \cos(\theta_X) \end{bmatrix}, \tag{2.3}$$

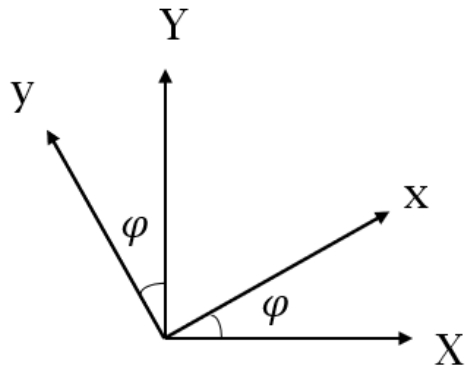

Figure 2.2: Coordinate rotation in two dimensions. X and Y denote the original frame, while x and y represent the frame rotated by an angle φ.

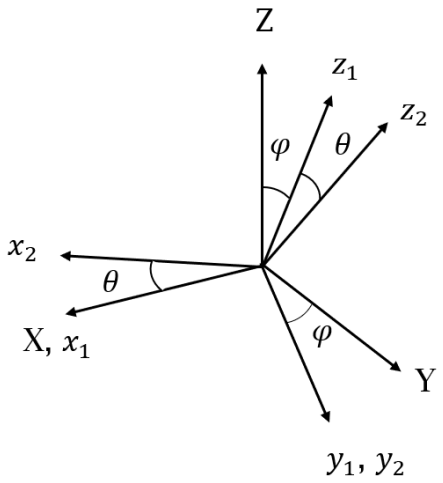

Figure 2.3: Example of rotation in three dimensions. X, Y and Z denote the original frame, while x_1, y_1 and z_1 represent the frame rotated by an angle φ about the X-axis. The final frame, after rotating angle θ about the y_1-axis is x_2, y_2 and z_2.

$$R_Y(\theta_Y) = \begin{bmatrix} \cos(\theta_Y) & 0 & -\sin(\theta_Y) \\ 0 & 1 & 0 \\ \sin(\theta_Y) & 0 & \cos(\theta_Y) \end{bmatrix}, \tag{2.4}$$

$$R_Z(\theta_Z) = \begin{bmatrix} \cos(\theta_Z) & \sin(\theta_Z) & 0 \\ -\sin(\theta_Z) & \cos(\theta_Z) & 0 \\ 0 & 0 & 1 \end{bmatrix}. \tag{2.5}$$

If several rotations are considered, the rotational matrices are multiplied together from the left. For example, in Figure 2.3, a system with the original space-fixed axes X, Y, Z rotates an angle φ about the X-axis, which results in a transformation to the new axes x_1, y_1, z_1. Then, rotating the system the angle θ about the y_1-axis

will result in the system x_2, y_2, z_2. Mathematically this converts to

$$\begin{bmatrix} x_1 \\ y_1 \\ z_1 \end{bmatrix} = R_X(\varphi) \begin{bmatrix} X \\ Y \\ Z \end{bmatrix}, \tag{2.6}$$

$$\begin{bmatrix} x_2 \\ y_2 \\ z_2 \end{bmatrix} = R_{y_1}(\theta) \begin{bmatrix} x_1 \\ y_1 \\ z_1 \end{bmatrix}, \tag{2.7}$$

$$\begin{bmatrix} x_2 \\ y_2 \\ z_2 \end{bmatrix} = \underbrace{R_{y_1}(\theta) R_X(\varphi)}_{R(\varphi,\theta)} \begin{bmatrix} X \\ Y \\ Z \end{bmatrix}. \tag{2.8}$$

Here, R denotes the full rotational matrix describing an initial rotation φ about X, and then a rotation θ about the new axis y_1. If more rotations are performed, the additional rotational matrices are multiplied from the left for the body-fixed coordinate system as seen in equation (2.8).

2.2 Eigenvalue problem in structural dynamics

The structural dynamics equation (SDE) of free vibration for an undamped system reads

$$\boldsymbol{M}\ddot{\boldsymbol{u}}(t) + \boldsymbol{K}\boldsymbol{u}(t) = \boldsymbol{0} \tag{2.9}$$

with $\boldsymbol{M}$ and $\boldsymbol{K}$ denoting the mass and stiffness matrix, respectively. The vector $\boldsymbol{u(t)}$ describes the deformation. Similarly, the vector $\ddot{\boldsymbol{u}}(t)$ define the corresponding accelerations. The undamped SDE of free vibrations can be decomposed using the harmonic assumption [35] of a discretization $\boldsymbol{q}$

$$\boldsymbol{u}(t) \approx \boldsymbol{q}(t) = \boldsymbol{\varphi} \cdot \cos(\omega t) = \boldsymbol{\varphi} \cdot \mathfrak{Re}\left\{e^{\mathrm{i}\omega t}\right\}. \tag{2.10}$$

Here, $\boldsymbol{\varphi}$ represents a time-invariant vector describing a deformed shape, ω is the frequency of the free vibration and i denotes the imaginary unit. Furthermore, $\mathfrak{Re}\left\{e^{\mathrm{i}\omega t}\right\}$ denotes the real part of the complex exponential function $e^{\mathrm{i}\omega t}$. From this harmonic assumption, the velocity can be expressed as $\dot{\boldsymbol{u}}(t) \approx \dot{\boldsymbol{q}}(t) = \boldsymbol{\varphi} \cdot \mathfrak{Re}\left\{\mathrm{i}\omega e^{\mathrm{i}\omega t}\right\}$, and finally the acceleration vector read

$$\ddot{\boldsymbol{u}}(t) \approx \ddot{\boldsymbol{q}}(t) = \boldsymbol{\varphi} \cdot \mathfrak{Re}\left\{-\omega^2 e^{\mathrm{i}\omega t}\right\}. \tag{2.11}$$

Inserting the harmonic expressions of the position in equation (2.10) and acceleration in equation (2.11), into the undamped SDE of free vibration in equation (2.9) gives

$$-\omega^2 \boldsymbol{M}\boldsymbol{\varphi} \cdot \mathfrak{Re}\left\{e^{\mathrm{i}\omega t}\right\} + \boldsymbol{K}\boldsymbol{\varphi} \cdot \mathfrak{Re}\left\{e^{\mathrm{i}\omega t}\right\} = \boldsymbol{0}, \tag{2.12}$$

which is equivalent to

$$\left(\boldsymbol{K}\boldsymbol{\varphi} - \omega^2 \boldsymbol{M}\boldsymbol{\varphi}\right) \mathfrak{Re}\left\{e^{\mathrm{i}\omega t}\right\} = \boldsymbol{0}. \tag{2.13}$$

Using the zero-product property, equation (2.13) is satisfied if $\boldsymbol{K}\boldsymbol{\varphi} - \omega^2\boldsymbol{M}\boldsymbol{\varphi} = \mathbf{0}$ or if $\mathfrak{Re}\left\{e^{\mathrm{j}\omega t}\right\} = \mathbf{0}$. The time-invariant deformation shapes are obtained when

$$\boldsymbol{K}\boldsymbol{\varphi} - \omega^2\boldsymbol{M}\boldsymbol{\varphi} = \mathbf{0}. \tag{2.14}$$

It is noted that equation (2.14) is satisfied for the trivial solution when $\boldsymbol{\varphi} = \mathbf{0}$. However, since this solution implies no deformation, the trivial solution is irrelevant for determining the deformation shape. Instead, the eigenvalue problem (EVP)

$$\boldsymbol{K}\boldsymbol{\varphi} = \omega^2\boldsymbol{M}\boldsymbol{\varphi} \iff \boldsymbol{M}^{-1}\boldsymbol{K}\boldsymbol{\varphi} = \omega^2\boldsymbol{\varphi} \tag{2.15}$$

is obtained. In general, several solution pairs $\left\{\omega_i^2, \boldsymbol{\varphi}_i\right\}$ exist. The eigenfrequencies ω_i are the square-root of the obtained eigenvalues ω_i^2, and the corresponding eigenvectors $\boldsymbol{\varphi}_i$ constitute the time-invariant deflection shapes.

2.3 Component mode synthesis

Apart from different ways of solving an EVP, there are methods to reduce the size of the EVP and thereby reduce the computational cost of the solution process. Within the field of structural dynamics, Guyan reduction, dynamic reduction, improved reduction system (IRS), system equivalent expansion reduction process (SEREP), modal truncation, CMS by Craig–Chang, Krylov subspace methods, balanced truncation, CMS by Craig–Bampton, CMS by MacNeal and CMS by Rubin, are common methods of reducing the size of an EVP [12].

Each method has different advantages and uses different approaches to reduce the size of the EVP. For example CMS by Craig-Chang is an implicit reduction method that utilize so-called free-interface modes and so-called attachment modes [33]. The free-interface modes are obtained by solving the undamped SDE of free vibrations. In order to obtain the attachment modes, a unit force is imposed to a few physical coordinates [33]. In case the substructure is unconstrained, rigid body modes (RBMs) are included in the reduction [15, 33]. In contrast to the Craig-Chang reduction method, the CMS by MacNeal uses both fixed- and free-interface modes. The fixed- and free-interface modes are referred to as hybrid modes. Apart from the hybrid modes, the MacNeal reduction method utilizes inertia relief attachment modes [27].

However, all of the previously mentioned methods to reduce the size of the EVP cannot be considered within the scope of this thesis. Since Craig-Bampton reduction (i.e. CMS by Craig-Bampton) is considered to be a reliable reduction method [35]. Additionally, Craig-Bampton reduction is used by Nastran (Andreasson, M., personal communication, April 2, 2025) the method will be explained and exemplified in detail, see sections 2.3.2 and 3.3. The Craig-Bampton reduction is closely connected to Guyan reduction [35], which is a simpler reduction method. Hence the Guyan reduction method is presented prior to the Craig-Bamtopn reduction, see sections 2.3.1 and 3.2.

In order to asses how well the mode shapes computed through reduction methods correlate to the expected shape from solving the full EVP, the modal assurance criterion (MAC) can be used [35]. The MAC is computed as

$$MAC = \frac{\left(\tilde{\boldsymbol{\varphi}}^T \hat{\boldsymbol{\varphi}}\right)^2}{||\tilde{\boldsymbol{\varphi}}||_2^2 ||\hat{\boldsymbol{\varphi}}||_2^2} \tag{2.16}$$

where $\tilde{\boldsymbol{\varphi}}$ denotes the state-space (time independent) eigenvector from the reduced solution and $\hat{\boldsymbol{\varphi}}$ denotes the time independent vector from the solution of the full EVP from equation (3.1). In the denominator, $||\bullet||_2$ denotes the $\mathbb{L}_2$-norm. The MAC provides a number between 0 and 1, where 1 means that the vectors are co-linear and thereby identical. In contrast, 0 means that the modes are orthogonal and therefore completely unrelated [35].

2.3.1 Guyan reduction

Guyan reduction is an exact static condensation method based on the idea of dividing the DOFs of the discretized solution vector $\boldsymbol{q}$ into one set $\boldsymbol{q}_a$, associated to an interface between substructures, and one set $\boldsymbol{q}_b$ associated to the studied subsystem itself [35], see Figure 2.4. After reduction, the substructure constitute a so-called superelement [35]. The discretized displacement vector $\boldsymbol{q}$ can then be described as

$$\boldsymbol{q} = \begin{Bmatrix} \boldsymbol{q}_a \\ \boldsymbol{q}_b \end{Bmatrix}. \tag{2.17}$$

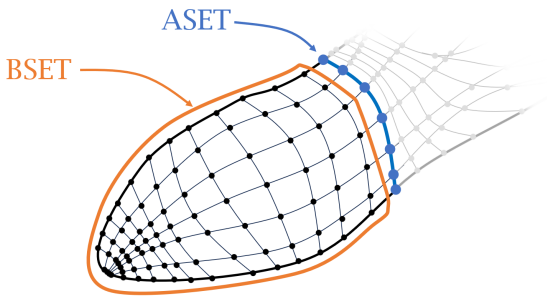

Figure 2.4: Example of ASET nodes defining the interface, and BSET nodes representing the internal nodes of the substructure for an arbitrary domain. Here it is assumed that all DOFs of a certain node belong to the same set.

The static undamped SDE (i.e. $\boldsymbol{K}\boldsymbol{q} = \boldsymbol{f}$ where $\boldsymbol{f}$ is an external applied force) can then be partitioned as

$$\boldsymbol{K}\boldsymbol{q} = \begin{bmatrix} \boldsymbol{K}_{aa} & \boldsymbol{K}_{ab} \\ \boldsymbol{K}_{ba} & \boldsymbol{K}_{bb} \end{bmatrix} \begin{Bmatrix} \boldsymbol{q}_a \\ \boldsymbol{q}_b \end{Bmatrix} = \begin{Bmatrix} \boldsymbol{f}_a \\ \boldsymbol{f}_b \end{Bmatrix} = \boldsymbol{f}, \tag{2.18}$$

where $\boldsymbol{f}_a$ and $\boldsymbol{f}_b$ denotes the forces acting on the ASET and BSET respectively [35]. The second row of equation (2.18) implies that

$$\boldsymbol{q}_b = \boldsymbol{K}_{bb}^{-1}\left(-\boldsymbol{K}_{ba}\boldsymbol{q}_a + \boldsymbol{f}_b\right) \tag{2.19}$$

which inserted into the first row of equation (2.18) gives

$$\begin{aligned} \boldsymbol{K}_{aa}\boldsymbol{q}_a + \boldsymbol{K}_{ab}\left[\boldsymbol{K}_{bb}^{-1}\left(-\boldsymbol{K}_{ba}\boldsymbol{q}_a + \boldsymbol{f}_b\right)\right] &= \boldsymbol{f}_a \\ &\Longleftrightarrow \\ \left[\boldsymbol{K}_{aa} - \boldsymbol{K}_{ab}\boldsymbol{K}_{bb}^{-1}\boldsymbol{K}_{ba}\right]\boldsymbol{q}_a &= \boldsymbol{f}_a - \boldsymbol{K}_{ab}\boldsymbol{K}_{bb}^{-1}\boldsymbol{f}_b. \end{aligned} \tag{2.20}$$

Hence, the behavior of the interface DOFs of the static undamped SDE can be obtained without solving the full system. More precisely, only the DOFs included in the ASET are solved for, resulting in a smaller system of equations than the full problem. Now, introducing the matrix

$$\boldsymbol{S} = -\boldsymbol{K}_{bb}^{-1}\boldsymbol{K}_{ba}, \tag{2.21}$$

and noting that the transpose of $\boldsymbol{S}$ can be described as

$$\boldsymbol{S}^T = -\boldsymbol{K}_{ba}^T\boldsymbol{K}_{bb}^{-T} = -\boldsymbol{K}_{ab}\boldsymbol{K}_{bb}^{-1} \tag{2.22}$$

since $\boldsymbol{K}$ is symmetric, equation (2.20) can be described as

$$\left[\boldsymbol{K}_{aa} + \boldsymbol{K}_{ab}\boldsymbol{S}\right]\boldsymbol{q}_a = \boldsymbol{f}_a + \boldsymbol{S}^T\boldsymbol{f}_b. \tag{2.23}$$

Furthermore, it is noted that

$$\begin{aligned} \boldsymbol{0} &= \boldsymbol{S}^T\boldsymbol{K}_{ba} - \boldsymbol{S}^T\boldsymbol{K}_{ba} = \boldsymbol{S}^T\boldsymbol{K}_{ba} - \boldsymbol{S}^T\boldsymbol{I}\boldsymbol{K}_{ba} \\ &= \boldsymbol{S}^T\boldsymbol{K}_{ba} - \boldsymbol{S}^T\boldsymbol{K}_{bb}\boldsymbol{K}_{bb}^{-1}\boldsymbol{K}_{ba} \\ &\overset{(2.21)}{=} \boldsymbol{S}^T\boldsymbol{K}_{ba} + \boldsymbol{S}^T\boldsymbol{K}_{bb}\boldsymbol{S}. \end{aligned} \tag{2.24}$$

Therefore, the contribution $\left[\boldsymbol{S}^T\boldsymbol{K}_{ba} + \boldsymbol{S}^T\boldsymbol{K}_{bb}\boldsymbol{S}\right]\boldsymbol{q}_a = \boldsymbol{0}$ can be added to the left hand side (LHS) of equation (2.23):

$$\begin{aligned} \left[\boldsymbol{K}_{aa} + \boldsymbol{K}_{ab}\boldsymbol{S}\right]\boldsymbol{q}_a + \left[\boldsymbol{S}^T\boldsymbol{K}_{ba} + \boldsymbol{S}^T\boldsymbol{K}_{bb}\boldsymbol{S}\right]\boldsymbol{q}_a &= \boldsymbol{f}_a + \boldsymbol{S}^T\boldsymbol{f}_b \\ &\Longleftrightarrow \\ \left[\boldsymbol{K}_{aa} + \boldsymbol{S}^T\boldsymbol{K}_{ba} + \boldsymbol{K}_{ab}\boldsymbol{S} + \boldsymbol{S}^T\boldsymbol{K}_{bb}\boldsymbol{S}\right]\boldsymbol{q}_a &= \boldsymbol{f}_a + \boldsymbol{S}^T\boldsymbol{f}_b \\ &\Longleftrightarrow \\ \begin{bmatrix}\boldsymbol{I} & \boldsymbol{S}^T\end{bmatrix}\begin{bmatrix}\boldsymbol{K}_{aa} & \boldsymbol{K}_{ab} \\ \boldsymbol{K}_{ba} & \boldsymbol{K}_{bb}\end{bmatrix}\begin{bmatrix}\boldsymbol{I} \\ \boldsymbol{S}\end{bmatrix}\boldsymbol{q}_a &= \begin{bmatrix}\boldsymbol{I} & \boldsymbol{S}^T\end{bmatrix}\begin{Bmatrix}\boldsymbol{f}_a \\ \boldsymbol{f}_b\end{Bmatrix}. \end{aligned} \tag{2.25}$$

Now, constructing the static condensation transformation matrix [35],

$$\boldsymbol{T} = \begin{bmatrix}\boldsymbol{I} \\ \boldsymbol{S}\end{bmatrix}, \tag{2.26}$$

equation (2.25) and thereby also the exact static condensation from equation (2.20), can be described as

$$\boldsymbol{T}^T\begin{bmatrix}\boldsymbol{K}_{aa} & \boldsymbol{K}_{ab} \\ \boldsymbol{K}_{ba} & \boldsymbol{K}_{bb}\end{bmatrix}\boldsymbol{T}\boldsymbol{q}_a = \boldsymbol{T}^T\begin{Bmatrix}\boldsymbol{f}_a \\ \boldsymbol{f}_b\end{Bmatrix} \tag{2.27}$$

or

$$\underbrace{\boldsymbol{T}^T\boldsymbol{K}\boldsymbol{T}}_{=\bar{\boldsymbol{K}}}\boldsymbol{q}_a = \underbrace{\boldsymbol{T}^T\boldsymbol{f}}_{=\bar{\boldsymbol{f}}}. \tag{2.28}$$

Provided that the number of DOFs in the ASET are considerably fewer than the number of DOFs of the full system, the system $\bar{\boldsymbol{K}}\boldsymbol{q}_a = \bar{\boldsymbol{f}}$, is considerably smaller than the full system. When solving this smaller problem $\bar{\boldsymbol{K}}\boldsymbol{q}_a = \bar{\boldsymbol{f}}$, the mode shapes of the ASET are obtained [35]. Furthermore, combining equations (2.19), (2.21) and (2.26) gives

$$\boldsymbol{q} = \begin{Bmatrix}\boldsymbol{q}_a \\ \boldsymbol{q}_b\end{Bmatrix} = \boldsymbol{T}\boldsymbol{q}_a + \begin{Bmatrix}\boldsymbol{0} \\ \boldsymbol{K}_{bb}^{-1}\boldsymbol{f}_b\end{Bmatrix}, \tag{2.29}$$

it is shown that also the movement (i.e. mode shapes) of the BSET DOFs can be obtained without solving a larger system. In particular, it is noticed that the movement of the BSET DOFs is obtained by the pure transformation $\boldsymbol{q} = \boldsymbol{T}\boldsymbol{q}_a$ for the special case of no external forces acting on the BSET.

Guyan reduction of the undamped SDE ($\boldsymbol{M}\ddot{\boldsymbol{u}} + \boldsymbol{K}\boldsymbol{u} = \boldsymbol{f}$) is obtained by transforming the mass and stiffness matrices as well as the displacement, acceleration and external force vectors with the static condensation transformation matrix $\boldsymbol{T}$ as

$$\underbrace{\boldsymbol{T}^T\boldsymbol{M}\boldsymbol{T}}_{=\bar{\boldsymbol{M}}}\overbrace{\ddot{\boldsymbol{q}}_a}^{\ddot{\boldsymbol{q}}} + \underbrace{\boldsymbol{T}^T\boldsymbol{K}\boldsymbol{T}}_{=\bar{\boldsymbol{K}}}\overbrace{\boldsymbol{q}_a}^{\boldsymbol{q}} = \underbrace{\boldsymbol{T}\boldsymbol{f}}_{=\bar{\boldsymbol{f}}} \tag{2.30}$$

and solve the reduced system $\bar{\boldsymbol{M}}\ddot{\boldsymbol{q}}_a + \bar{\boldsymbol{K}}\boldsymbol{q}_a = \bar{\boldsymbol{f}}$. For the Guyan reduction, the inertial term (i.e. the term including $\boldsymbol{M}$) will be approximately condensed by neglecting the so-called coupling effects between the ASET and BSET DOFs. The Guyan reduction will hence provide an approximation of the solution to the discretized EVP [35].

2.3.2 Craig-Bampton reduction

Studying a two-dimensional (2D) beam, it is seen that the Guyan reduction could capture the eigenfrequencies and mode shapes well, c.f. the example in section 3.2. Furthermore, it has been seen that the number of DOFs included in the ASET and the distribution of these DOFs, has an impact on how well the eigenfrequencies (and mode shapes) of the solution of the full EVP can be captured.

In particular, if all translational DOFs of the 2D beam are included in the ASET, the eigenfrequencies and mode shapes are (almost) equal to the ones of solving the full EVP, see the example in section 3.2.1. However, it can be difficult to physically motivate why all translational DOFs should be included in the ASET, and thereby constitute the interface. Besides, a reduction to less than half of the size can be desired for large systems. One way to keep the ASET physically meaningful and interpretable, while reducing the system further, is to use the Craig-Bampton reduction. Craig-Bampton reduction can be seen as an extension of Guyan reduction and may be able to more accurately represent the eigenfrequencies and mode shapes.

The Craig-Bampton reduction uses the extended reduction matrix

$$\boldsymbol{R} = \begin{bmatrix} \boldsymbol{I} & \boldsymbol{0} \\ \boldsymbol{S} & \boldsymbol{\Phi}_{bb} \end{bmatrix} \tag{2.31}$$

where $\boldsymbol{S}$ is defined by equation (2.21) and contains the so-called static correction modes. The matrix $\boldsymbol{\Phi}_{bb}$ contains so-called fixed interface modes that are the result of solving the undamped SDE (equation (2.9)) for the BSET (internal) DOFs only [35], i.e. by solving

$$\boldsymbol{K}_{bb}\boldsymbol{\Phi}_{bb} = \boldsymbol{M}_{bb}\boldsymbol{\Phi}_{bb}\boldsymbol{\Omega}_{bb}^2. \tag{2.32}$$

Here, the eigenvectors are collected into the matrix $\boldsymbol{\Phi}_{bb}$ as

$$\boldsymbol{\Phi}_{bb} = \begin{bmatrix} | & | & \\ \boldsymbol{\varphi}_{1,bb} & \boldsymbol{\varphi}_{2,bb} & \cdots \\ | & | & \end{bmatrix} \tag{2.33}$$

and the associate eigenvalues are collected into the diagonal matrix $\boldsymbol{\Omega_{bb}}$ as

$$\boldsymbol{\Omega}_{bb} = \begin{bmatrix} \omega_{1,bb} & 0 & 0 \\ 0 & \omega_{2,bb} & 0 \\ 0 & 0 & \ddots \end{bmatrix}. \tag{2.34}$$

Replacing the Guyan reduction matrix $\boldsymbol{T}$ in equation (2.30) by the Craig-Bampton reduction matrix $\boldsymbol{R}$ defined in equation (2.31), the Craig-Bampton reduction is obtained:

$$\underbrace{\boldsymbol{R}^T\boldsymbol{M}\boldsymbol{R}}_{=\bar{\boldsymbol{M}}}\overbrace{\ddot{\boldsymbol{q}}_a}^{\ddot{\boldsymbol{q}}} + \underbrace{\boldsymbol{R}^T\boldsymbol{K}\boldsymbol{R}}_{=\bar{\boldsymbol{K}}}\overbrace{\boldsymbol{q}_a}^{\boldsymbol{q}} = \underbrace{\boldsymbol{R}\boldsymbol{f}}_{=\bar{\boldsymbol{f}}}. \tag{2.35}$$

In particular, if the full matrix $\boldsymbol{\Phi}_{bb}$ (i.e. all fixed interface modes $\boldsymbol{\varphi}_{1,bb} - \boldsymbol{\varphi}_{n_{BSET},bb}$ where n_{BSET} denotes the number of DOFs in the BSET) are included in the Craig-Bampton reduction matrix $\boldsymbol{R}$, there is no reduction in size of the problem to solve. In order to obtain a reduced solution, the fixed interface modes can be divided into slow and fast modes and neglecting the fast modes [35]. The slow modes are associated with low eiegenfrequencies and are the ones to be accounted for.

2.4 Nastran solver

To facilitate understanding of how the industrial solver Nastran operates, descriptions of how an MNF is created and numerical methods are specified. A numerical method that may be used in creating an MNF is Lanczos, which is explained together with CMS used in the MNF creation.

2.4.1 MNF creation

An MNF is created through specification in a so-called ecd-file that is sent through Nastran. In the ecd-file, the solution sequence (SOL) 103 is stated at the beginning,

which means that a modal analysis is performed on the specified geometry [20]. Thereafter, specific parameters to create an MNF are stated together with the so-called EIGRL statement.

The EIGRL statement defines an eigenvalue analysis, which is solved with Lanczos method. The variables that can be stated in the EIGRL are among others the lower and higher frequency of interest, and the number of modes to be calculated [20]. However, in the file, the domain solver is set to automated component mode synthesis (ACMS) which proceeds the Lanczos method for finding the eigenpairs (i..e the eigenvectors and corresponding eigenvalues). The ACMS method is faster at finding the eigenpairs than Lanczos method, and the resulting eigenpairs are similar. The stiffness reduction is exact when using ACMS, while the mass reduction introduces approximations, mainly due to the frequency cut-off used for calculating the eigenvectors [14]. The Lanczos and ACMS methods are described in detail in sections 2.4.2.1 and 2.4.2.2.

In the MNF creation file, the ASET DOFs are also specified by defining the nodes included and which DOFs that are to be included. Lastly, the model is defined by different include files corresponding to different parts of the model and properties. For example in the thesis work, there are include files of the material database and the body in white which is the frame of the vehicle body.

To create the MNF, the MNF creation file is sent to Nastran which creates a file of format `.mnf`. The MNF includes the physical mass matrix, a stiffness matrix, a modal mass matrix, a modal load matrix, and a diagonal matrix of ASET unit boundary displacements [22]. The MNF also includes information of the node locations and the mode shapes [30].

2.4.2 Numerical methods in Nastran

In Nastran, the eigenpairs of the EVP defined by equation (2.15) can be found using a tridiagonal method or the Lanczos method. The tridiagonal method is recommended when all eigenpairs should be extracted, while Lanczos is an iterative method that should be used when only a few eigenpairs are desired. One reason for this is that for Lanczos method, the effort of solving the EVP is linearly proportional to the number of requested eigenmodes. In other words, Lanczos method has the benefit of limiting the computational cost when a few eigenpairs are needed. However, if all eigenpairs are of interest, the tridigonal method should be more efficient [21].

Nastran offers two tridiagonal methods: Givens and Householder. The methods reduce and transform the matrix of interest into a tridiagonal matrix. If the mass matrix is singular, modified methods of Givens or Householder may be used with different transformation schemes [21]. For the Givens and Householder tridiagonalization methods, the orthogonal so-called QR transformation is utilized. The eigenvalues of the resulting matrix from the QR transformation constitute the eigenvalues of the original EVP, as a result of preservation of the eigenvalues under orthogonal transformation [21].

The eigenvalues of the QR transformation are stored in a diagonal matrix. In order to find the diagonal form of the original tridiagonal matrix faster, the origin may be shifted. In Nastran, the so-called Wilkinson's quadratic shift is used, where each diagonal element are subtracted by a certain value. Additionally, zeros in the tridiagonal matrix are utilized since uncoupling may be used [21]. However, for MNF creation, only eigenpairs up to a certain frequency are desired and hence Lanczos method should be utilized for the applications related to the thesis work.

2.4.2.1 Lanczos method

The basics of Lanczos method is presented in Algorithm 1. As follows from the pseudo code, the method is based on an initiation followed by iteration until each eigenvector has converged. Depending on the exact method used, the initialization and update steps vary slightly. More specifically, Nastran uses a version of Lanczos method referred to as the shifted block Lanczos method [21]. In order to understand the shifted block algorithm used by Nastran, a Lanczos method is presented, followed by the shifted Lanczos, and finally an extension to the shifted block algorithm.

Algorithm 1 Basics of Lanczos method.

1. Initialization
Initialize starting vector(s), and
Initialize scalars

2. Iterate
for $j = 1, 2, 3, ..., n$ **do** ▷ n is the number of eigenpairs to be extracted.
Iterate until eigenvector j converges.
end for

Basic Lanczos

For Lanczos method, the initialization step in Algorithm 1 include a starting vector $\boldsymbol{q}_1$, an additional vector $\boldsymbol{q}_0 = \boldsymbol{0}$ and a scalar $\beta = 0$ [21]. The starting vector $\boldsymbol{q}_1$ can be arbitrarily chosen [13]. For the iteration until convergence described in Algorithm 1, the eigenvector $\boldsymbol{q}_j$ is determined through iteration over another variable p. The updated eigenvector $\boldsymbol{q}_j^{p+1}$ is determined as [21]

$$\boldsymbol{q}_j^{p+1} = \frac{\boldsymbol{M}^{-1}\boldsymbol{K}\boldsymbol{q}_j^p - \alpha_j^p \boldsymbol{q}_j^p - \beta_j^p \boldsymbol{q}_j^{p-1}}{\beta_j^{p+1}} := \frac{\boldsymbol{r}_j^{p+1}}{\beta_j^{p+1}}, \tag{2.36}$$

where $\boldsymbol{M}$ and $\boldsymbol{K}$ denote the mass and stiffness matrices of the EVP described by equation (2.15). Furthermore, α_j^p, β_j^p and β_j^{p+1} are scalars that should be selected such that the updated vector $\boldsymbol{q}_j^{p+1}$ is mass normal and mass orthogonal to the previously converged vectors $\boldsymbol{q}_i$ where $i < j$ [13]. In Nastran, the scalars are selected such that the resulting eigenvectors are mass orthonormal if the calculations are performed without round-off errors. The updated eigenvector $\boldsymbol{q}_j^{p+1}$ is computed in four steps [21]:

1. $\alpha_j^p = \left(\boldsymbol{q}_j^p\right)^T \boldsymbol{M}^{-1}\boldsymbol{K}\boldsymbol{q}_j^p$,
2. $\boldsymbol{r}_j^{p+1} = \boldsymbol{M}^{-1}\boldsymbol{K}\boldsymbol{q}_j^p - \alpha_j^p\boldsymbol{q}_j^p - \beta_j^p\boldsymbol{q}_j^{p-1}$,
3. $\beta_j^{p+1} = ||\boldsymbol{r}_j^{p+1}||$, and
4. $\boldsymbol{q}_j^{p+1} = \boldsymbol{r}_j^{p+1}/\beta_j^{p+1}$.

Note that $||\bullet||$ here denotes the norm of $\bullet$. In order to find the corresponding eigenvalues, the scalars $\alpha_k, k = 1, ..., j$ and $\beta_l, l = 2, ..., j$ can be used. The scalars are put into a matrix $\boldsymbol{T}_j$

$$\boldsymbol{T}_j = \begin{bmatrix} \alpha_1 & \beta_2 & & & & & & \\ \beta_2 & \alpha_2 & \beta_3 & & & & & \\ & \beta_3 & \alpha_3 & \beta_4 & & & & \\ & & & \ddots & & & & \\ & & & \beta_i & \alpha_i & \beta_{i+1} & & \\ & & & & & \ddots & & \\ & & & & & & & \beta_j \\ & & & & & & \beta_j & \alpha_j \end{bmatrix}, \tag{2.37}$$

and the eigenvalues corresponding to the computed eigenvectors $\boldsymbol{q}_j$, correspond to the eigenvalues of the tridiagonal matrix $\boldsymbol{T}_j$.

Shifted Lanczos

The Lanczos algorithm previously described, provides good approximations for large eigenvalues, but a poorer approximation for the smaller eigenvalues. One reason for this is that the small eigenvalues often are clustered together, while the larger eigenvalues are more separated. Since the lowest eigenvalues often are of interest, Lanczos algorithm is used on an inverted and shifted EVP. One way of shifting the EVP with a shift σ is by redefining the EVP as [21]

$$\boldsymbol{M}(\boldsymbol{K} - \sigma\boldsymbol{M})^{-1}\boldsymbol{M}\boldsymbol{q} = \frac{1}{\omega^2 - \sigma}\boldsymbol{M}\boldsymbol{q}, \tag{2.38}$$

where ω denotes the eigenfrequency of interest. The shift σ should be selected close to the eigenvalue (ω^2) of interest, and will then provide rapid convergence for the the desired eigenpair, and possibly also for a group of eigenpairs close to the shift [21].

As for the basic Lanczos algorithm, the initialization step of the shifted Lanczos algorithm include selection of a starting vector $\boldsymbol{q}_1$, definition of an additional vector $\boldsymbol{q}_0 = \boldsymbol{0}$ as well as a scalar $\beta_1 = 0$. However, there is a difference in how the starting vector is selected. For the shifted Lanczos algorithm, the starting vector $\boldsymbol{q}_1$ is selected in three steps [21]

1. Start from an arbitrary vector $\boldsymbol{r}_0$,
2. Define $\boldsymbol{r}_1 = \left(\boldsymbol{K} - \sigma\boldsymbol{M}\right)^{-1}\boldsymbol{M}\boldsymbol{r}_0$, and
3. Mass normalize $\boldsymbol{r}_1$ to obtain $\boldsymbol{q}_1 = \boldsymbol{r}_1/\sqrt{\boldsymbol{r}_1^T\boldsymbol{M}\boldsymbol{r}_1}$.

Similarly as for the basic Lanczos method, the iteration step from Algorithm 1 of the shifted Lanczos method include an iterative update of the estimated eigenvector $\boldsymbol{q}_j^p$ using four update steps and another vector $\boldsymbol{r}_j^{p+1}$ [21]:

1. $\alpha_j^p = \left(\boldsymbol{q}_j^p\right)^T \boldsymbol{M}\left(\boldsymbol{K} - \boldsymbol{\sigma}\boldsymbol{M}\right)^{-1}\boldsymbol{M}\boldsymbol{q}_j^p$,
2. $\boldsymbol{r}_j^{p+1} = \left(\boldsymbol{K} - \sigma\boldsymbol{M}\right)^{-1}\boldsymbol{M}\boldsymbol{q}_j^p - \alpha_j^p\boldsymbol{q}_j^p - \beta_j^p\boldsymbol{q}_j^{p-1}$,
3. $\beta_j^{p+1} = \sqrt{\left(\boldsymbol{r}_j^{p+1}\right)^T\boldsymbol{M}\boldsymbol{r}_j^{p+1}}$, and
4. $\boldsymbol{q}_j^{p+1} = \boldsymbol{r}_j^{p+1}/\beta_j^{p+1}$.

The approximate eigenvalue of the full problem is found from

$$\omega^2 = \sigma + \frac{1}{\theta}, \tag{2.39}$$

where θ is the eigenvalue of $\boldsymbol{T}_j$ in equation (2.37). All eigenvectors are mass orthogonal (also known as $\boldsymbol{M}$-orthogonal) since the Lanczos vectors $(q_1, q_2, ...)$ are mass orthogonal [21], as in equation (2.36).

Block algorithm

The previously described basic Lanczos algorithms may have difficulties to find eigenvalues of higher multiplicity due to that the algorithm only can calculate one eigenvector at a time. Eigenvectors of multiple eigenvalues of the same value may also appear in the tridiagonal matrix $\boldsymbol{T}_j$ as a result of round-off errors. As previously described, the shifted Lanczos algorithm, can handle clustered eigenvalues. However, each iteration step requires solving of a sparse linear system of equations together with a matrix multiplication with the mass matrix $\boldsymbol{M}$, and hence the algorithm implies storing of large matrices, which results in a significant computational cost [21].

In order to solve for multiple eigenvalues at the time without requiring too much memory to store matrices, the block Lanczsos method has been developed. This algorithm combines the shifted and inverted Lanczos algorithm in a block code. The initialization step, see Algorithm 1, of the block algorithm includes

1. Defining a matrix $\boldsymbol{R}_0$ with starting values of the eigenvectors. The matrix should have k columns, where k correspond to the number of eigenpairs that should simultaneously be solved for.
2. From $\boldsymbol{R}_0$, the matrix $\boldsymbol{R}_1$ is defined using a shift as $\boldsymbol{R}_1 = \left(\boldsymbol{K} - \sigma\boldsymbol{M}\right)^{-1}\boldsymbol{M}\boldsymbol{R}_0$.

3. Factorization into one upper triangular matrix $\boldsymbol{B}_0$ of size $k \times k$ and one mass orthonormal matrix $\boldsymbol{Q}_1$ such that $\boldsymbol{R}_1 = \boldsymbol{Q}_1 \boldsymbol{B}_0$.

4. Define two additional matrices $\boldsymbol{Q}_0 = \boldsymbol{0}$ and $\boldsymbol{B}_1 = \boldsymbol{0}$.

In Algorithm 1, the iteration step includes iterating over j blocks with k eigenvectors being determined in each block. The iterative update for block j and iteration p can be formulated as

1. Define $\boldsymbol{A}_j^p = \left(\boldsymbol{Q}_j^p\right)^T \boldsymbol{M} \left(\boldsymbol{K} - \sigma \boldsymbol{M}\right)^{-1} \boldsymbol{M} \boldsymbol{Q}_j^p$.

2. Evaluate $\boldsymbol{R}_j^{p+1} = \left(\boldsymbol{K} - \sigma \boldsymbol{M}\right)^{-1} \boldsymbol{M} \boldsymbol{Q}_j^p - \boldsymbol{Q}_j^p \boldsymbol{A}_j^p - \boldsymbol{Q}_j^{p-1} \left(\boldsymbol{B}_j^p\right)^T$.

3. Determine the new upper triangular and mass orthonormal matrices from $\boldsymbol{R}_j^{p+1} = \boldsymbol{Q}_j^{p+1} \boldsymbol{B}_j^{p+1}$.

The block Lanczos algorithm has the advantage of computing several eigenvalues of the original EVP together if the multiplicity of an eigenvalue is less then, or equal to k. From the block Lanczos algorithm, k number of eigenvectors can be solved for simultaneously, which reduces the calculation cost by the factor $1/k$ compared to the simple Lanczos algorithm [21].

The matrix for finding the approximate eigenvalues are now block triangular such that

$$\boldsymbol{T}_j = \begin{bmatrix} \boldsymbol{A}_1 & \boldsymbol{B}_2^T & & & & & \\ \boldsymbol{B}_2 & \boldsymbol{A}_2 & \boldsymbol{B}_3^T & & & & \\ & & \ddots & & & & \\ & & \boldsymbol{B}_i & \boldsymbol{A}_i & \boldsymbol{B}_{i+1}^T & & \\ & & & & \ddots & & \\ & & & & & & \boldsymbol{B}_j^T \\ & & & & & \boldsymbol{B}_j & \boldsymbol{A}_j \end{bmatrix} \tag{2.40}$$

with $\boldsymbol{B}_j$ being upper triangular, $\boldsymbol{T}_j$ becomes a band matrix with bandwidth $k+1$. The eigenvalues of $\boldsymbol{T}_j$ are found by first reducing it to be of tridiagonal form and then extracting the eigenvalues [21].

2.4.2.2 Automated component mode synthesis

ACMS is a multi-level modal reduction technique used by Nastran. The ACMS can be used for large models as well as for analyses requiring a large number of vibration modes since it offers a good approximation of the mode shapes. Through usage of reduced mass and stiffness matrices, the ACMS is an efficient method for solving large EVPs [18].

Similarly as for the Guyan and Craig-Bampton reduction, the ACMS results in approximate solutions since mode truncation is used. Unlike Guyan and Craig-

Bampton reduction, residual vectors may be included in the reduction to mitigate the approximation. One benefit of ACMS is that the calculation time is faster than other EVP solutions such as Lanczos method [18], which is explained in section 2.4.2.1. ACMS provides however an approximation to the full Lanczos solution of the EVP [17].

Compared to other CMS methods, ACMS uses automatically generated components instead of solving the full EVP for the ASET DOFs [17]. The breakdown of the large matrices may be through Craig-Bampton reduction [35]. The automatically generated components are divided through domain decomposition and can consist of hundreds of smaller matrices. Each component is then interpreted as a superelement in Nastran [29]. The accuracy of the ACMS approximation may be increased by a user defined parameter, stating the cut-off frequency as a scaling factor of the frequency of interest selected in the EIGRL statement. In Nastran, the default frequency is twice as large as the maximum frequency specified in the EIGRL statement in the MNF creation file [17].

2.5 Modal damping

A potentially important part of simulation modeling is the damping. Damping can be defined in different ways such as Rayleigh damping, Cauchy damping and modal damping [35]. For the MNF imported into the MBD simulations, modal damping is used since it has been used by Zeekr before the start of the thesis work and changing the damping model is considered to be a major modeling change, which is out of the scope of the thesis.

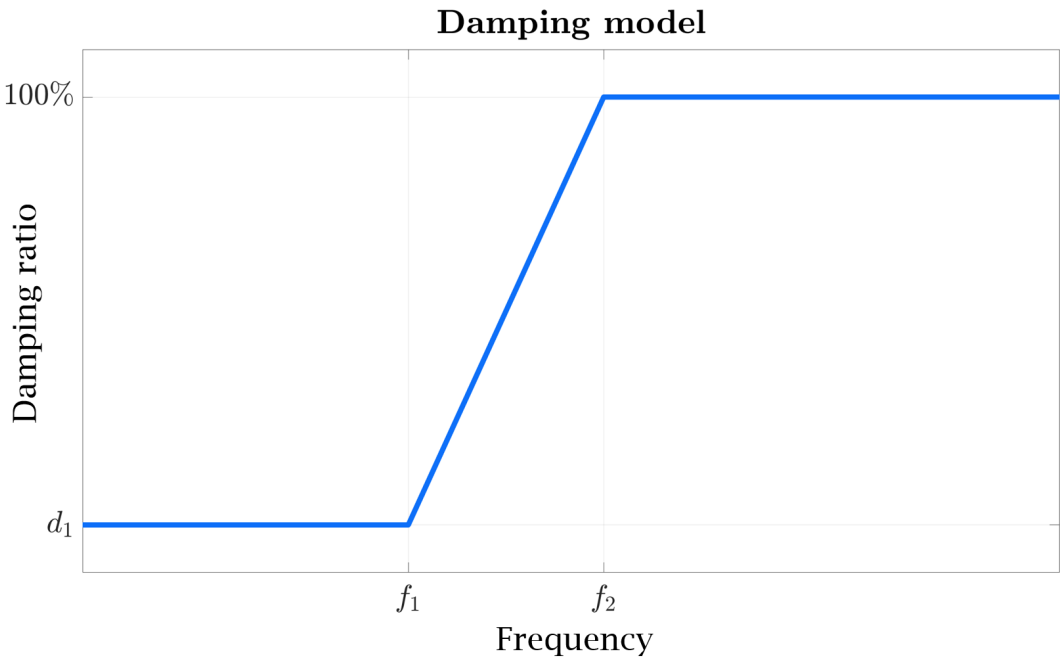

Figure 2.5: Graphical representation of how the damping ratio is defined in the MBD simulations.

Modal damping is the simplest assumption of a damped system. It is assumed that the damping matrix $\boldsymbol{D}_m$ (as in the damped SDE: $\boldsymbol{M}\ddot{\boldsymbol{q}} + \boldsymbol{D}_m\dot{\boldsymbol{q}} + \boldsymbol{K}\boldsymbol{q} = \boldsymbol{f}$) is a diagonal matrix. The diagonal assumption is motivated with the facts that the distribution of the damping is commonly ill-defined and that the assumption has shown to be consistent with an assumption of a so-called lightly damped system [13]. For the MBD simulation, the damping matrix is built up as [15]

$$\boldsymbol{D}_m = \begin{bmatrix} \mathbf{0}_{3\times6} & \mathbf{0}_{3\times1} & \dots & \mathbf{0}_{3\times1} & \mathbf{0}_{3\times1} \\ \mathbf{0}_{3\times6} & \mathbf{0}_{3\times1} & \dots & \mathbf{0}_{3\times1} & \mathbf{0}_{3\times1} \\ \mathbf{0}_{1\times6} & 2\zeta_1\sqrt{k_{11}m_{11}} & \dots & 0 & 0 \\ \mathbf{0}_{1\times6} & 0 & \dots & 0 & 0 \\ \vdots & \vdots & \ddots & \vdots & \vdots \\ \mathbf{0}_{1\times6} & 0 & \dots & 2\zeta_{n-1}\sqrt{k_{(n-1)(n-1)}m_{(n-1)(n-1)}} & 0 \\ \mathbf{0}_{1\times6} & 0 & \dots & 0 & 2\zeta_n\sqrt{k_{nn}m_{nn}} \end{bmatrix} \tag{2.41}$$

where ζ_i denotes the damping ratio while m_{ii} and k_{ii} denotes the element corresponding to the diagonal values in the mass and stiffness matrix respectively. In the MBD simulation, the damping ratio can be a function of time or system state [15]. For the thesis work, the damping ratio varies with the frequency according to Figure 2.5. In other words, the damping ratio d_1 is used up until a frequency f_1. Then, the damping ratio is linearly ramped up to 100% at the frequency f_2.

2.6 Opening distortion fingerprint

The stiffness of the car body has been an assessment criteria for conventional vehicles, but with electrical vehicles the battery changes the stiffness throughout the car body [36]. Important to note is that the stiffness must be sufficient to prevent frame twist and local deflections, which also impact the comfort for the passengers [1]. Investigating the stiffness in the closure openings and across the vehicle, local weak spots can be identified. One way to evaluate the local stiffness is through measuring the distortion with MSS [36].

For this thesis, the so-called E-line method has been used to evaluate the distortion of the car body. The distortion is measured by introducing diagonals representing the MSS, see Figures 2.6, 2.7 and 2.8. For the E-line method, a local coordinate system is introduced in each diagonal. Its origin is placed over the undeformed structure, see Figure 2.9. Advantages with the E-line method are that the local relative displacement is measured in the x, y and z directions. The orientation of the local coordinate system results in the out of plane distortion in the local y-component, and the in plane distortion is in the local x- and z-components [38]. As seen in Figure 2.9, the local z-component points in the direction of the diagonal between point 1 and point 2.

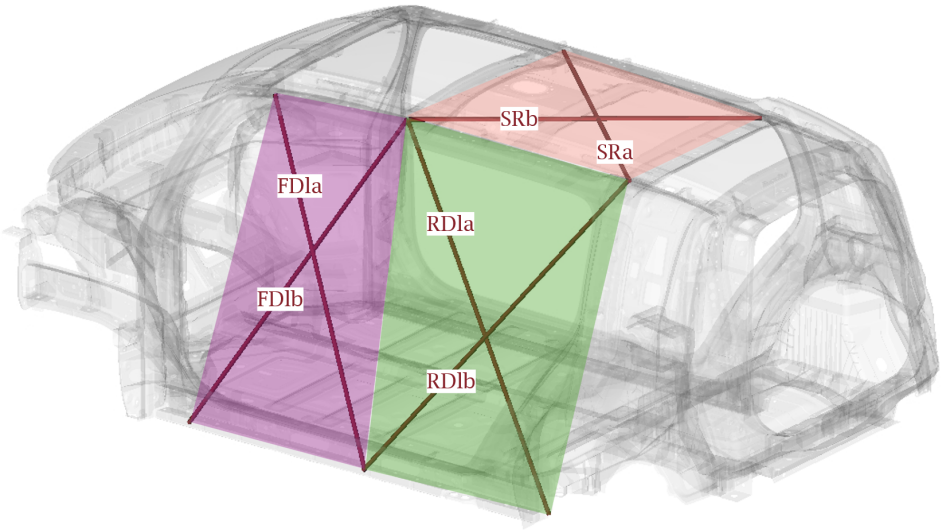

Figure 2.6: Schematic MSS of the left hand side of the robot-taxi.

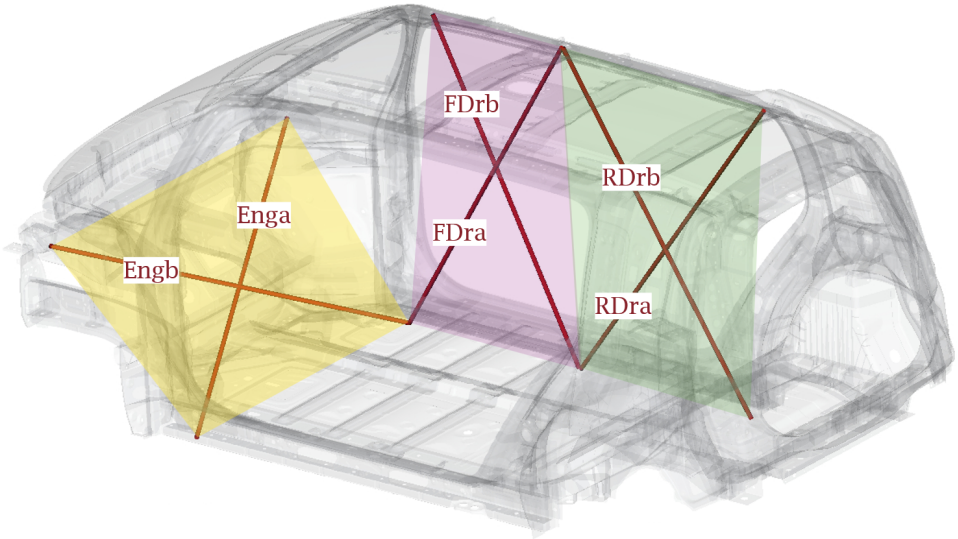

Figure 2.7: Schematic MSS of the right hand side of the robot-taxi.

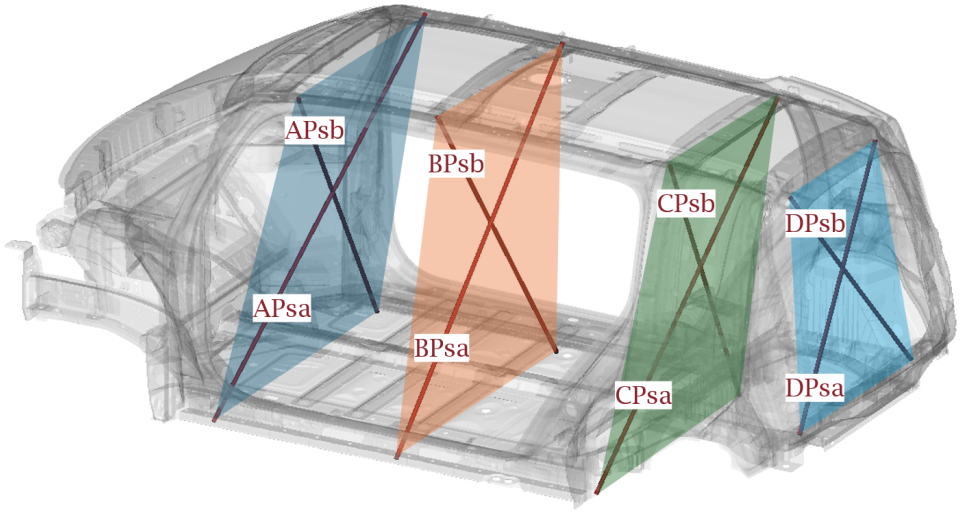

Figure 2.8: Schematic MSS of the cross-sections of the robot-taxi.

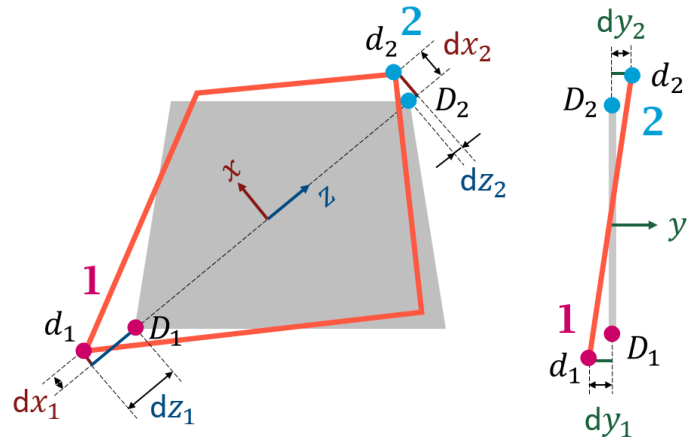

(a) **(b)**

Figure 2.9: Diagonal distortion evaluated with the E-line method over an arbitrary opening on the vehicle, (a) from a rear view, and (b) from a side view.

2.6.1 Rigid body motion

Measuring distortion according to the E-line method may result in so-called artificial values, see $\delta_{artificial}$ in Figure 2.10(a), which is unwanted when comparing data. It is here called artificial since it is does not correspond to an actual elongation of the diagonal. This artificial displacement due to rotation is captured in local coordinates since the accelerometer, used for measuring the deformation, changes position. Deformation due to pure rotation is illustrated in Figure 2.10(a), where A is the original position and A' is the position after rotation. If the motion is purely translational, the distances denoted Δ_A and Δ_O in Figure 2.10(b) are equal.

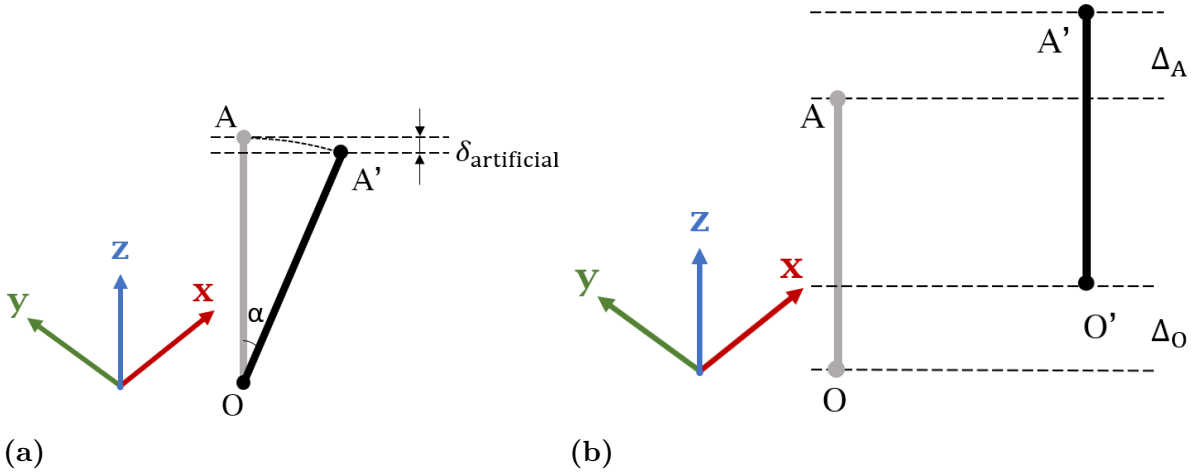

(a) (b)

Figure 2.10: Schematics of (a) pure rotational RB movement, and (b) pure translational RB movement.

For the case of both translational and rotational deformation, the rotational angle is of importance for evaluation of the so-called true deformation. In Figure 2.11, the influence of the angle is illustrated. When the rotational angle is small, the artificial contribution is small and negligible, see Figure 2.11(a). If the rotational angle is larger, the artificial contribution can not be neglected, see Figure 2.11(b).

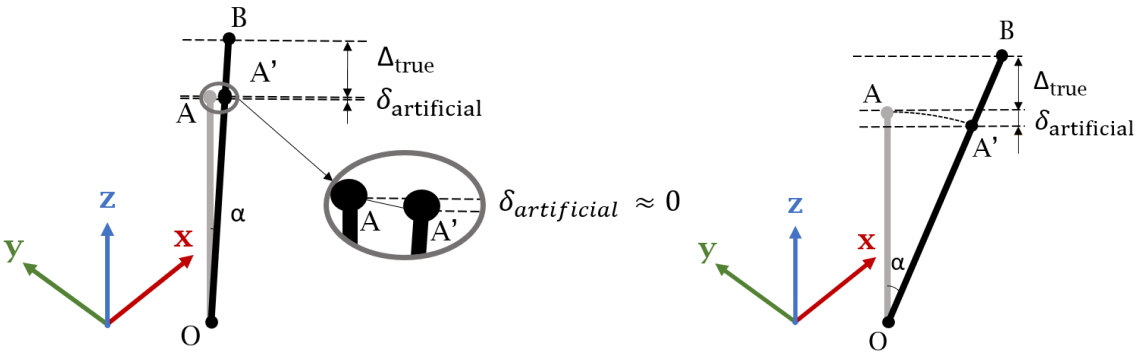

(a) (b)

Figure 2.11: Schematics of (a) rotational movement combined with elongation for small, and (b) large rotational angle.

Mathematically, the new coordinates can be seen in equation (2.2). For small angles, liniarization gives $\cos(\alpha) \approx 1$ and $\sin(\alpha) \approx \alpha$, resulting in a small displacement that can be neglected. Larger angles, on the other hand, results in displacements that must be taken into consideration.

2.6.2 Statistical evaluation parameter

The Statistical Evaluation Parameter (SEP) sorts the values of the distortion time history from highest to lowest. The user can thereafter choose a percentage of the highest values to include. On the included values, a mean value is then calculated

[38, 37, 4]. For example, an SEP value of 30% means that 30% of the highest values of all time steps are considered for evaluating the mean value. Choosing the percentage ensures that the extremums of the time signal do not entirely dominate the mean value [38]. For ODF creation, an SEP value of 30% has shown to be robust [38].

3

Beam examples

In order to further understand the theory presented in chapter 2, some numerical examples on a beam are presented. The first sections concern a virtual beam of unit parameters. This virtual beam is first discretized and thereafter subjected to CMS by Guyan, followed by CMS by Craig-Bampton in order to exemplify how e.g. the selection of the ASET and the number of fixed interface modes included in the CMS affect the solution. In order to assess how well the mode shapes correlate to each other, the MAC is used. Additionally, in order to allow for visual inspection, the displayed CMS mode shapes are normalized such that the maximum value is 1 and such that the first deflection points downwards. However, the mode shapes accounted for in the reduction matrices are mass-normalized.

After studying the virtual beam, a physical beam is studied in order to exemplify how RB motions can be observed. Furthermore, the sections on the physical beam exemplifies how accelerometers of the same kind as the ones used for measurements on the robot-taxi, measure. Additionally, the restrictions imposed by the accelerometers are highlighted. Lastly, the filtering and integration needed in order to obtain displacements are exemplified along with analytical references on which displacements that can be expected.

3.1 Eigenvalue problem of a beam

The stiffness and mass matrices can be described for a certain discretization. This procedure will be illustrated using a 2D beam divided into 15 elements, see Figure 3.1. For this specific beam discretization, each node include one degree of freedom (DOF) corresponding to vertical translation (c.f. y_1) and one DOF corresponding to in-plane rotation (c.f. θ_1). The translational and rotational DOFs y_i and θ_i for each node in Figure 3.1 can be collected into a vector $\boldsymbol{q}$. The vector $\boldsymbol{q}$ constitutes an approximation of the exact beam displacements, i.e. $\boldsymbol{u} \approx \boldsymbol{q}$. The discretized solution $\boldsymbol{q}$ should approach the exact position vector $\boldsymbol{u}$ as the number of elements increases.

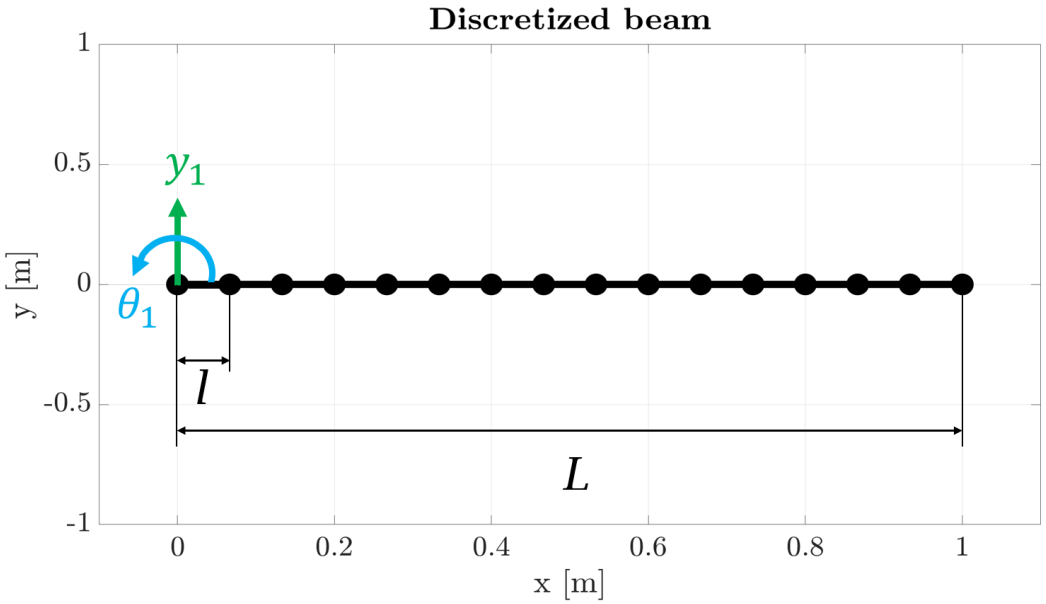

Figure 3.1: Beam discretization with 15 elements, corresponding to 16 nodes. On the leftmost node (node 1), the DOFs have been emphasized.

The DOFs are systematically numbered and collected into a vector $\boldsymbol{q}$. For the dicretized beam in Figure 3.1 the displacement vector is described as

$$\boldsymbol{u} \approx \boldsymbol{q}(t) = \begin{Bmatrix} y_1 \\ \theta_1 \\ y_2 \\ \theta_2 \\ \vdots \\ y_n \\ \theta_n \end{Bmatrix} \mathfrak{Re}\left\{e^{\mathrm{i}\omega t}\right\} = \underbrace{\begin{Bmatrix} q_1 \\ q_2 \\ q_3 \\ q_4 \\ \vdots \\ q_{2n-1} \\ q_{2n} \end{Bmatrix}}_{=\hat{\boldsymbol{\varphi}}} \mathfrak{Re}\left\{e^{\mathrm{i}\omega t}\right\}. \tag{3.1}$$

In the vector representation, the translational DOFs have been numbered q_{2n-1} with n, $n = 1, 2, ..., 16$, denoting the consecutive node number. Similarly, all rotational DOFs are numbered q_{2n}. The corresponding acceleration vector reads

$$\ddot{\boldsymbol{q}} = -\omega^2 \begin{Bmatrix} q_1 \\ q_2 \\ q_3 \\ q_4 \\ \vdots \\ q_{2n-1} \\ q_{2n} \end{Bmatrix} \mathfrak{Re}\left\{e^{\mathrm{i}\omega t}\right\}. \tag{3.2}$$

The corresponding mass- and stiffness matrices can be assembled from element contributions. For the beam in Figure 3.1, the element matrices read

$$\boldsymbol{M}_e = \frac{\rho A l}{420}\begin{bmatrix} 156 & 22l & 54 & -13l \\ & 4l^2 & 13l & -3l^2 \\ & & 156 & -22l \\ \text{sym} & & & 4l^2 \end{bmatrix}, \tag{3.3}$$

and

$$\boldsymbol{K}_e = \frac{EI_z}{l^3}\begin{bmatrix} 12 & 6l & -12 & 6l \\ & 4l^2 & -6l & 2l^2 \\ & & 12 & -6l \\ \text{sym} & & & 4l^2 \end{bmatrix} \tag{3.4}$$

respectively [35, 13]. The material density is denoted by ρ, A refers to the beam cross-sectional area and l to the element length (see Figure 3.1). Furthermore, E denotes the Young's modulus of the material and I_z constitutes the area moment of inertia in the xy-plane. Each element contribute to its ambient DOFs. For example, the element matrix of element 1 (the leftmost element in Figure 3.1) contributes to q_1, q_2, q_3 and q_4 in equation (3.1), and in general element i contributes to q_{2i-1}, q_{2i}, $q_{2(i+1)-1}$ and $q_{2(i+1)}$. Following this procedure, the full mass and stiffness matrices become sparse symmetric matrices of size 32×32 ($number\ of\ dofs\ \times\ number\ of\ dofs$):

$$\boldsymbol{M} = \frac{\rho A l}{420}\begin{bmatrix} 156 & 22l & 54 & -13l & 0 & 0 & 0 & \dots & 0 & 0 \\ & 4l^2 & 13l & -3l^2 & 0 & 0 & 0 & \dots & 0 & 0 \\ & & 156+156 & -22l+22l & 54 & -13l & 0 & \dots & 0 & 0 \\ & & & 4l^2+4l^2 & 13l & -3l^2 & 0 & \dots & 0 & 0 \\ & & & & \ddots & \ddots & & & \vdots & \vdots \\ & & & & & \ddots & \ddots & & & \\ & & & & & & \ddots & \ddots & 0 & 0 \\ & & & & & & 156+156 & -22l+22l & 54 & -13l \\ & & & & & & & 4l^2+4l^2 & 13l & -3l^2 \\ & & & & & & & & 156 & -22l \\ \text{sym} & & & & & & & & & 4l^2 \end{bmatrix}_{32\times 32}, \tag{3.5}$$

and

$$\boldsymbol{K} = \frac{EI_z}{l^3}\begin{bmatrix} 12 & 6l & -12 & 6l & 0 & 0 & 0 & \dots & 0 & 0 \\ & 4l^2 & -6l & 2l^2 & 0 & 0 & 0 & \dots & 0 & 0 \\ & & 12+12 & -6l+6l & -12 & 6l & 0 & \dots & 0 & 0 \\ & & & 4l^2+4l^2 & -6l & 2l^2 & 0 & \dots & 0 & 0 \\ & & & & \ddots & \ddots & & & \vdots & \vdots \\ & & & & & \ddots & \ddots & & & \\ & & & & & & \ddots & \ddots & 0 & 0 \\ & & & & & & 12+12 & -6l+6l & -12 & 6l \\ & & & & & & & 4l^2+4l^2 & -6l & 2l^2 \\ & & & & & & & & 12 & -6l \\ \text{sym} & & & & & & & & & 4l^2 \end{bmatrix}_{32\times 32} \tag{3.6}$$

respectively. For the discretized beam in Figure 3.1, the first five modes and corresponding frequencies (i.e. the eigenpairs $\{\omega_i, \boldsymbol{\varphi}_i\}$, $i = \{1, 2, 3, 4, 5\}$ from the EVP) are presented in Figure 3.2. From the figure it follows that the first two eigenfrequencies are zero and correspond to RBMs. Additionally, it is noticed that the fifth mode (the green graph) is slightly edgy, which indicates that the discretization is on the border of properly capturing the shape of the fifth mode.

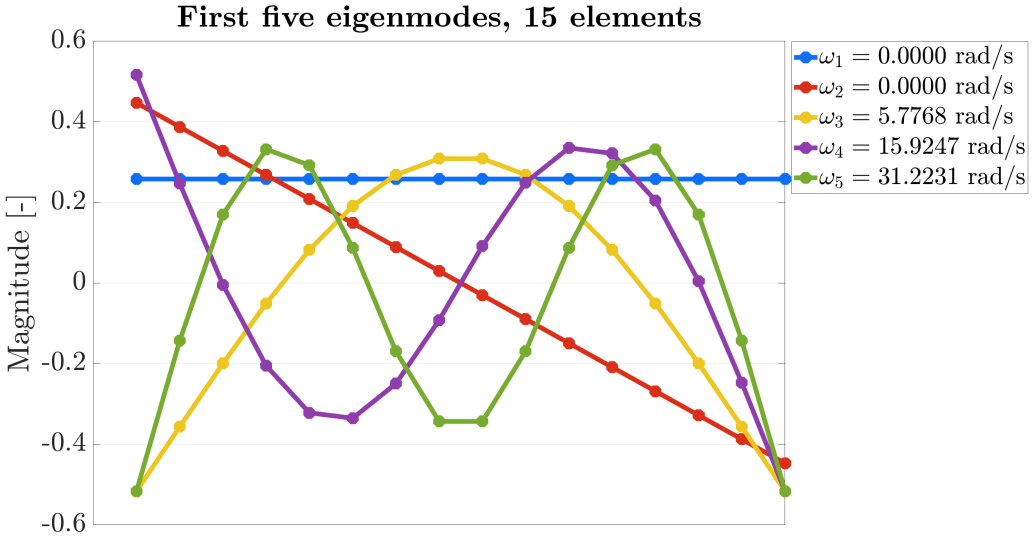

Figure 3.2: First five eigenmodes and corresponding eigenfrequencies of the discretized beam in Figure 3.1. Unit parameters are used, i.e. $L = 1$ m, $EI_z = 1$ Pam^4 and $\rho A = 1$ kg/m.

In other words, Figure 3.2, illustrates that the selected discretization affects how many and how well the mode shapes can be captured. In order to further emphasize and investigate this, the dependence of the discretization has been studied for the first, second, tenth and hundredth flexible modes (i.e. mode number 3, 4, 12 and 102 respectively). The results are presented in Figure 3.3. From the figure it follows that all studied eigenfrequencies are affected by the discretization. Additionally, the

computed frequencies decreases as the number of elements increases, which suggests that a poorer discretization overestimates the frequency.

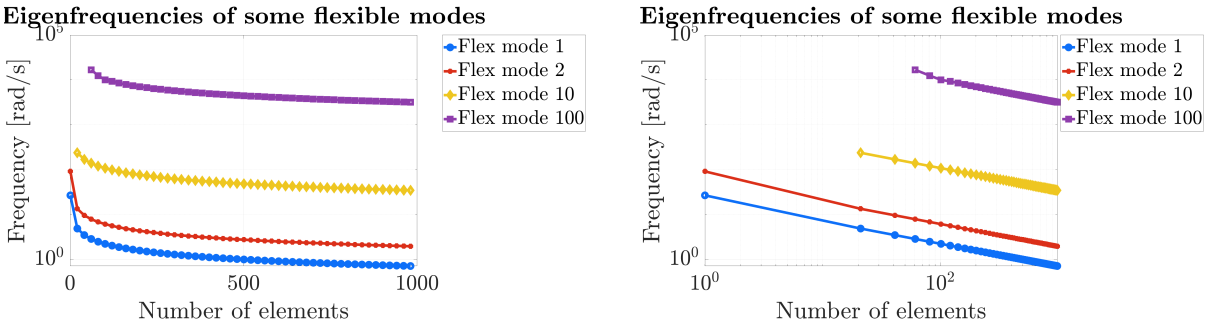

(a) **(b)**

Figure 3.3: Eigenfrequencies of mode number 3, 4, 12 and 102 respectively (flexible mode number 1, 2, 10 and 100 respectively) for different discretizations. Represented (a) with a logarithmic y-axis, and (b) in a log-log plot.

Another important observation from Figure 3.3(a) is that the reduction in frequency is most prominent in the transition between 1 and 21 elements. In this context, it is also important to consider the resulting mode shapes. Figure 3.4 illustrates the corresponding mode shapes for a discretization of one element and one discretization of 21 elements. From Figure 3.4(a) it clearly follows that the discretization is insufficient to capture the shape of even the first two flexible modes. However, from Figure 3.4(b) it follows that 21 elements capture the shapes of the two flexible modes. Figure 3.4(b) also illustrates that the tenth flexible mode is insufficiently captured using a discretization of 21 elements.

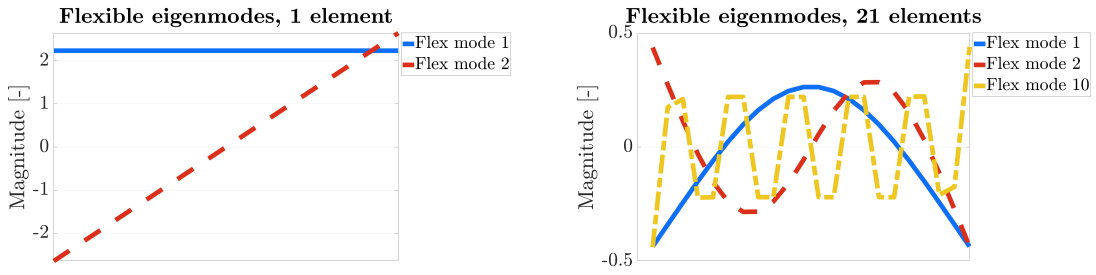

(a) **(b)**

Figure 3.4: Some flexible modes using a discretization with (a) one element, and (b) 21 elements.

3.2 Guyan reduction exemplified

Once again considering the discretized 2D beam in Figure 3.1 with mass and stiffness matrices according to equation (3.5) and (3.6) respectively, an illustration of Guyan

reduction and how the selection of ASET DOFs affect the solution, is presented. As an initial example, it is assumed that the beam is to be connected to something else in both ends, which results in the ASET being defined by the DOFs of the first and last node in Figure 3.1. See also Figure 3.5 for an illustration of the selected ASET DOFs.

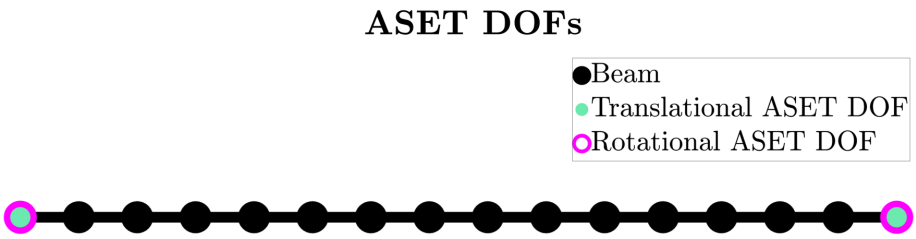

Figure 3.5: Illustration of ASET DOFs for the Guyan reduction example.

The ASET DOFs illustrated in Figure 3.5 correspond to DOFs number 1, 2, 31 and 32 using the DOF numbering described in section 3.1. As previously described, the discretized solution vector $\boldsymbol{q}$ is assumed to be built up following the structure from equation (2.17), i.e. it is assumed that the first n_a DOFs (where n_a denotes the number of DOFs in the ASET) correspond to the ASET DOFs. The displacement vector of the discretized beam from section 3.1, is ordered differently, and hence reordering of the DOFs is needed. The new displacement vector then becomes

$$\hat{\boldsymbol{q}} = \begin{Bmatrix} q_1 \\ q_2 \\ q_{31} \\ q_{32} \\ \hdashline q_3 \\ q_4 \\ q_5 \\ \vdots \\ q_{30} \end{Bmatrix} = \begin{Bmatrix} \boldsymbol{q}_a \\ \hdashline \boldsymbol{q}_b \end{Bmatrix}. \tag{3.7}$$

The corresponding reordered mass and stiffness matrices read

$$\hat{\boldsymbol{M}} = \begin{bmatrix} \boldsymbol{M}_{aa} & \boldsymbol{M}_{ab} \\ \boldsymbol{M}_{ba} & \boldsymbol{M}_{bb} \end{bmatrix}, \tag{3.8}$$

and

$$\hat{\boldsymbol{K}} = \begin{bmatrix} \boldsymbol{K}_{aa} & \boldsymbol{K}_{ab} \\ \boldsymbol{K}_{ba} & \boldsymbol{K}_{bb} \end{bmatrix} \tag{3.9}$$

respectively. The aa-partition of the mass and stiffness matrix respectively are constructed extracting the elements corresponding to the ASET DOFs. In this case, the elements corresponding to row 1, 2, 31 and 32 as well as column 1, 2, 31 and 32

are to be extracted from equations (3.5) and (3.6) such that

$$\boldsymbol{M}_{aa} = \frac{\rho A l}{420}\begin{bmatrix} 156 & 22l & 0 & 0 \\ & 4l^2 & 0 & 0 \\ & & 156 & -22l \\ \text{sym} & & & 4l^2 \end{bmatrix}, \quad \boldsymbol{K}_{aa} = \frac{EI_z}{l^3}\begin{bmatrix} 12 & 6l & 0 & 0 \\ & 4l^2 & 0 & 0 \\ & & 12 & -6l \\ \text{sym} & & & 4l^2 \end{bmatrix}. \tag{3.10}$$

Similarly, the *bb*-partition is constructed extracting the elements corresponding to the BSET DOFs, i.e. the elements on line 3-30 and column 3-30, from equation (3.5) and (3.6) respectively. Then the partitions read

$$\boldsymbol{M}_{bb} = \frac{\rho A L}{420}\begin{bmatrix} 312 & 0 & 54 & -13l & 0 & \dots & 0 \\ & 8l^2 & 13l & -3l^2 & 0 & \dots & 0 \\ & & \ddots & \ddots & & & \vdots \\ & & & \ddots & \ddots & & 0 \\ & & & & & 312 & 0 \\ \text{sym} & & & & & & 8l^2 \end{bmatrix}_{28\times 28}, \tag{3.11}$$

and

$$\boldsymbol{K}_{bb} = \frac{EI_z}{l^3}\begin{bmatrix} 24 & 0 & -12 & 6l & 0 & \dots & 0 \\ & 8l^2 & -6l & 2l^2 & 0 & \dots & 0 \\ & & \ddots & \ddots & & & \vdots \\ & & & \ddots & \ddots & & 0 \\ & & & & & 24 & 0 \\ \text{sym} & & & & & & 8l^2 \end{bmatrix}_{28\times 28} \tag{3.12}$$

respectively. The coupling partitions *ba* are constructed extracting the elements corresponding to the rows of the BSET DOFs and the columns of the ASET DOFs respectively, resulting in

$$\boldsymbol{M}_{ba} = \begin{bmatrix} 54 & 13l & 0 & 0 \\ -13l & -3l^2 & \vdots & \vdots \\ 0 & 0 & 0 & 0 \\ \vdots & \vdots & 54 & -13l \\ 0 & 0 & 13l & -3l^2 \end{bmatrix}_{28\times 4} \tag{3.13}$$

and

$$\boldsymbol{K}_{ba} = \begin{bmatrix} -12 & -6l & 0 & 0 \\ 6l & 2l^2 & \vdots & \vdots \\ 0 & 0 & 0 & 0 \\ \vdots & \vdots & -12 & -6l \\ 0 & 0 & -6l & 2l^2 \end{bmatrix}_{28\times 4}. \tag{3.14}$$

Since $\boldsymbol{M}$ and $\boldsymbol{K}$ both are symmetric, it holds that

$$\boldsymbol{M}_{ab} = \boldsymbol{M}_{ba}^T, \quad \boldsymbol{K}_{ab} = \boldsymbol{K}_{ba}^T. \tag{3.15}$$

With $\boldsymbol{K}_{bb}$ and $\boldsymbol{K}_{ba}$ defined, the static correction modes $\boldsymbol{S}$ can be determined form equation (2.21). The static correction modes are defined by the columns of $\boldsymbol{S}$ visualized in Figure 3.6. Also four FE solutions, corresponding to solving the static SDE from equation (2.18) with prescribed unit displacements in the directions of the four ASET DOFs defined by Figure 3.5 and equation (3.7) respectively, are included in the figure as black lines. It is seen that the static correction modes exist for the BSET nodes only and that the static correction modes coincide with the static FE solution.

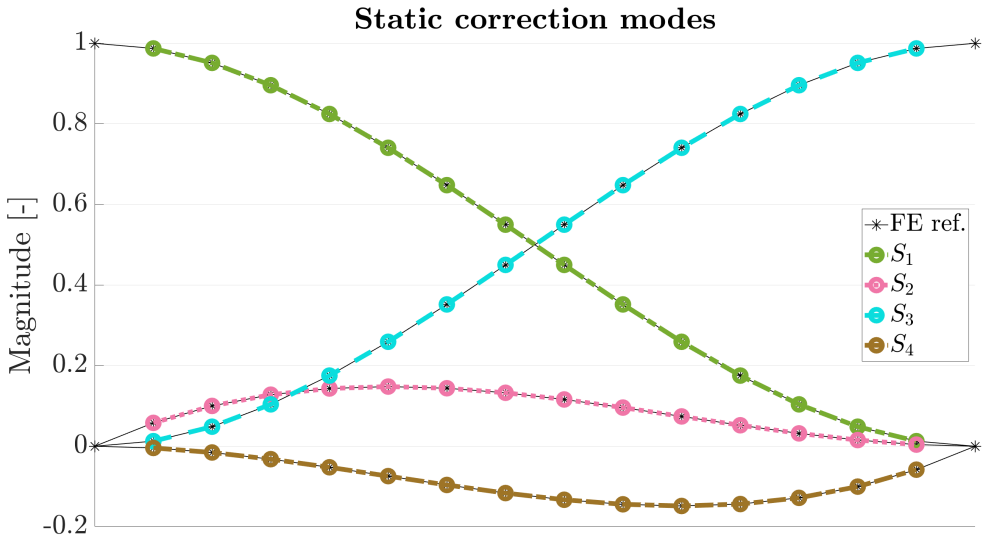

Figure 3.6: Static correction modes. The black lines show the results of an FE reference solution solving for an unit displacement in each ASET DOF. S_i refers to column i of $\boldsymbol{S}$ from equation (2.21).

With the reordered mass and stiffness matrices defined by equations (3.8)-(3.15), the Guyan reduction matrix $\boldsymbol{T}$ defined by equations (2.21), (2.26), (3.12) and (3.14) can be used to transform the system according to equation (2.30). Then the reduced problem becomes

$$\bar{\boldsymbol{M}}\ddot{\boldsymbol{q}}_a + \bar{\boldsymbol{K}}\boldsymbol{q}_a = \boldsymbol{0}, \tag{3.16}$$

with

$$\bar{\boldsymbol{M}}_{4\times4} = \boldsymbol{T}^T\hat{\boldsymbol{M}}\boldsymbol{T}, \quad \text{and} \quad \bar{\boldsymbol{K}}_{4\times4} = \boldsymbol{T}^T\hat{\boldsymbol{K}}\boldsymbol{T}. \tag{3.17}$$

Noteworthy, the size of the EVP described by equation (3.16) is of size four times four, to be compared with solving the full EVP that is of size thirty-two by thirty-two. Solving numerically for the ASET DOFs with unit parameters (the same material parameters as for Figure 3.2), the ASET displacements $\boldsymbol{q}_{a,i}$ and eigenvectors

$\tilde{\boldsymbol{\varphi}}_i$ read

$$\begin{aligned} \boldsymbol{q}_{a,1} &= \underbrace{\begin{Bmatrix} -0.1051 \\ -0.8949 \\ -1.0000 \\ -0.8949 \end{Bmatrix}}_{=\tilde{\varphi}_1} \cdot \cos\left(\omega_1 t\right), \quad \boldsymbol{q}_{a,2} = \underbrace{\begin{Bmatrix} 0.6761 \\ -1.0000 \\ -0.3239 \\ -1.0000 \end{Bmatrix}}_{=\tilde{\varphi}_2} \cdot \cos\left(\omega_2 t\right), \\ \boldsymbol{q}_{a,3} &= \underbrace{\begin{Bmatrix} -0.1667 \\ 1.0000 \\ -0.1667 \\ -1.0000 \end{Bmatrix}}_{=\tilde{\varphi}_3} \cdot \cos\left(\omega_3 t\right), \quad \boldsymbol{q}_{a,4} = \underbrace{\begin{Bmatrix} -0.0833 \\ 1.0000 \\ 0.0833 \\ 1.0000 \end{Bmatrix}}_{=\tilde{\varphi}_4} \cdot \cos\left(\omega_4 t\right) \end{aligned} \tag{3.18}$$

with eigenvalues

$$\omega_1 = 0 \text{ rad/s}, \quad \omega_2 = 0 \text{ rad/s}, \quad \omega_3 = 6.92 \text{ rad/s}, \text{ and } \quad \omega_4 = 23.66 \text{ rad/s}. \tag{3.19}$$

With the mode shapes of the ASET known (equation (3.18)), the motion of the BSET can be represented using the transpose of the static correction transformation matrix $\boldsymbol{T}$ according to

$$\tilde{\boldsymbol{q}} = \boldsymbol{T}^T \boldsymbol{q}_a. \tag{3.20}$$

After reordering back to the representation of equation (3.1), i.e. to representing DOF i at position i in the vector, the eigenmodes and eigenfrequencies of Figure 3.7 are obtained. A comparison to the expected outcome from solving the full EVP (see also Figure 3.2) is presented in Figure 3.8.

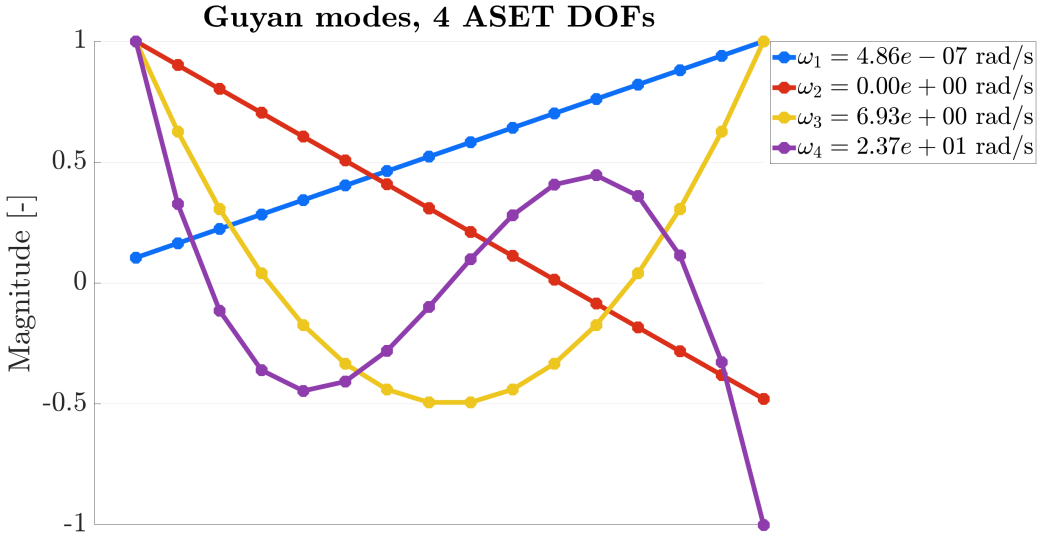

Figure 3.7: Modes after Guyan reduction with ASET DOFs according to Figure 3.5.

From Figures 3.7 and 3.8 it follow that the two first modes from the Guyan reduction have eigenfrequencies close to 0 rad/s and correspond to RBMs. Two RBMs are

expected from solving the full problem, but from Figure 3.8 it follows that the exact motions differ. For example, from Figure 3.8(a) it follows that the full solution gives a pure RB translation, while the reduced solution appears to be a mix between translation and rotation. Studying the third and fourth eigenmodes of the Guyan reduced problem, see Figure 3.8(c) and 3.8(d) respectively, it follow that the shape from the Guyan reduction is similar to the solution of the full EVP and that the obtained eigenfrequencies of the reduced problem are larger than for the solution of the full problem.

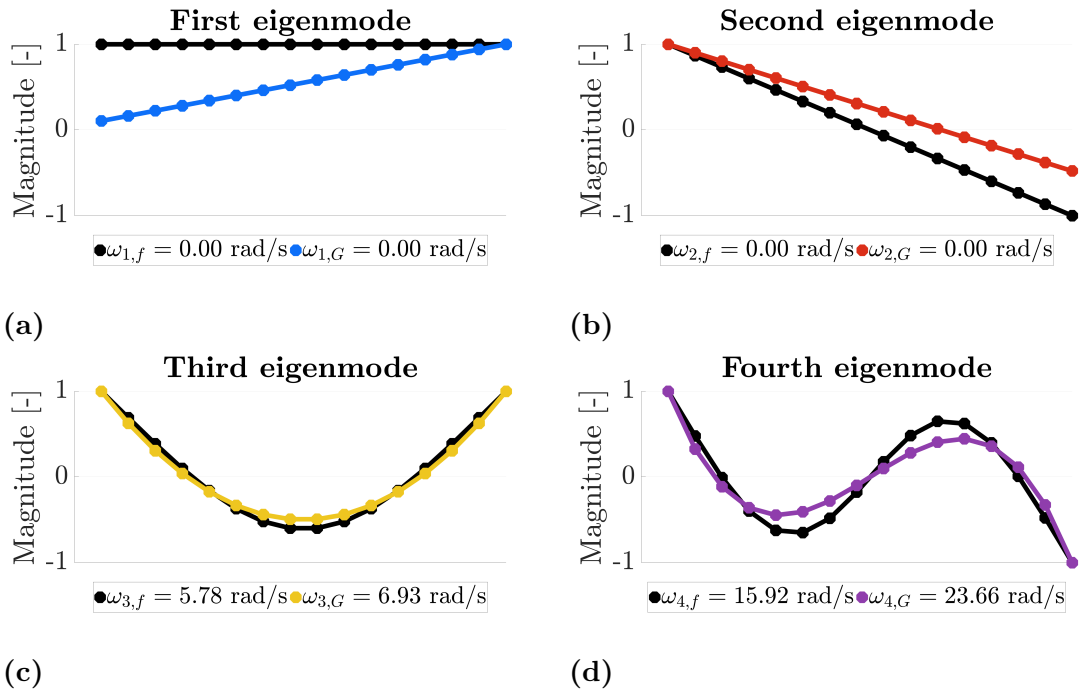

Figure 3.8: In (a) first, (b) second, (c) third and (d) fourth eigenmode after Guyan reduction with ASET DOFs according to Figure 3.5. For each mode, the unreduced (i.e. full) solution is included in black.

The MAC has been evaluated between each mode originating from the Guyan reduction and the corresponding mode from the full solution, see Table 3.1. In the table, the second column assess whether the translational DOFs (i.e. the DOFs visualized in Figure 3.8) correlate, the third column assess whether the rotational DOFs correlate and the fourth column considers all DOFs in the eigenvector. From the table it follows that the state-space eigenvectors are similar for all modes. The rotation of the second mode is identical to the full solution, and the rotation of the third mode is very similar to the rotation of the full solution. Furthermore, the translation is (almost) equal for the third mode. In total it seems like the second and third modes are captured most accurately and that the first mode is least similar to the full solution, which makes sense considering Figure 3.8.

Table 3.1: MAC for the Guyan modes compared to the corresponding modes from the solution of the full problem.

Mode number	Translation	Rotation	Total MAC
1	0.80	0.70	0.26
2	0.75	1.00	0.97
3	0.99	0.96	0.96
4	0.95	0.86	0.86

3.2.1 Number of ASET degrees of freedom

In order to assess whether the number of ASET DOFs has an impact on the performance of the Guyan reduction, the number of ASET DOFs have been increased in five steps from the LHS of the beam. The the studied configurations are presented in Figure 3.9. Here, performance concerns how well the eigenvectors from the Guyan reduction correlate to eigenvectors from solving the full EVP. The obtained eigenfrequencies of the flexible modes are represented in Figure 3.10.

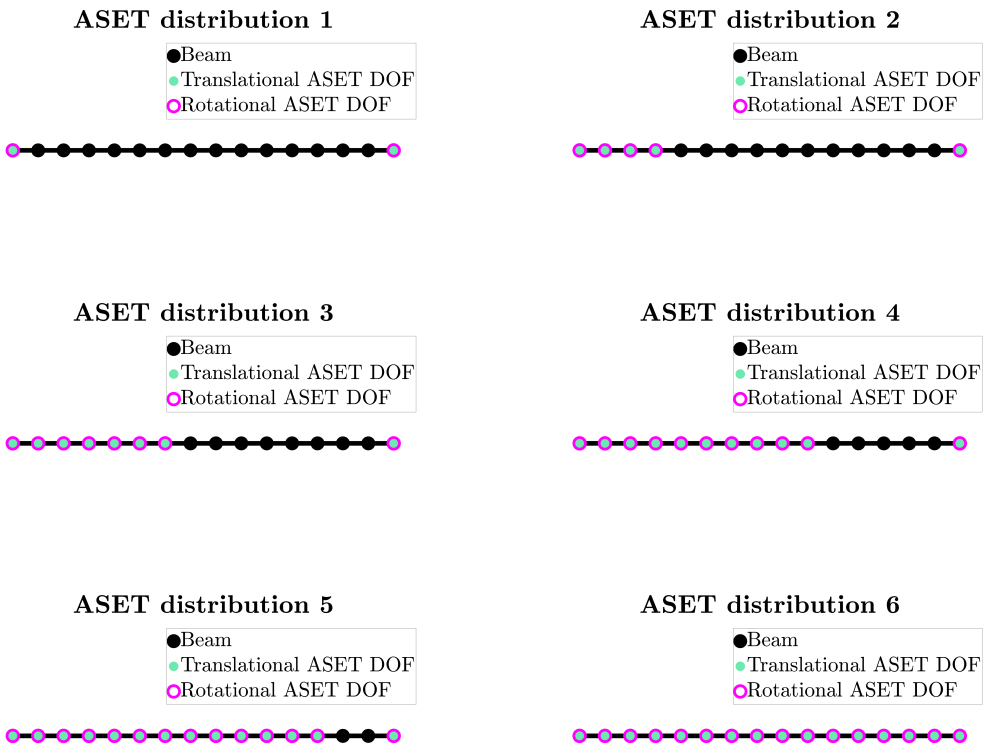

Figure 3.9: Considered ASET distributions with increasing number of ASET DOFs.

From Figure 3.10 it follows that the number of modes included in the reduction has an impact on how well the eigenfrequencies of the flexible modes can be represented

by a Guyan reduced solution. In general it is observed that an increased number of ASET DOFs results in a more accurate representation of more modes. In particular including all possible DOFs in the ASET results in a perfect match to all studied eigenfrequencies. Furthermore, in Appendix A.1 it can be seen that the MAC of all modes are a perfect match to the ones obtained from solving the full problem. However, it is important to keep in mind that the reduced EVP will be of size $n_{ASET} \times n_{ASET}$ where n_{ASET} denoted the number of ASET DOFs included in the reduction. Hence, including all DOFs in the ASET only transforms the problem.

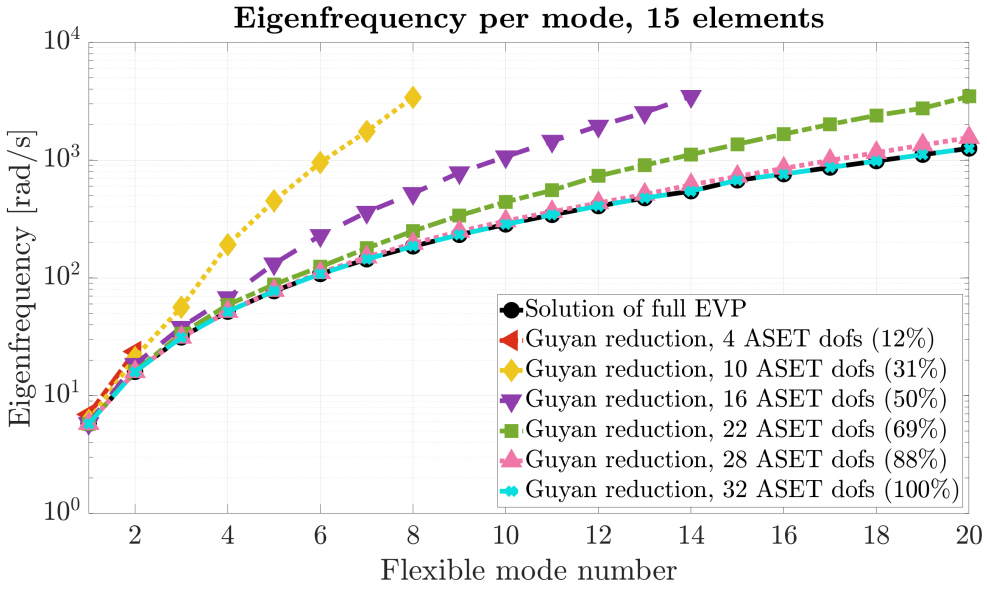

Figure 3.10: Eigenfrequency of flexible mode number 1-20 (i.e. for mode number 3-20) for different number of ASET DOFs included in the Guyan reduction. ASET distributions according to Figure 3.9.

3.2.2 Distribution of ASET degrees of freedom

It has been shown that the number of DOFs in the ASET has an impact on how well the solution of the full EVP described by equation (2.14) can be represented by a Guyan reduction described by equation (3.16). In order to investigate whether the distribution of ASET DOFs has an impact on the results, the distributions presented in Figure 3.11 have been considered. Note that for all configurations in Figure 3.11, 50% of the total number of DOFs are included in the ASET. Additionally, the first configuration equal **Distribution 3** in Figure 3.9.

The results of the Guyan reduction for **configuration 1-9** from Figure 3.11 are presented in Figure 3.12. From Figure 3.12 it follows that also the distribution of ASET DOFs has an impact on how well the eigenfrequencies are captured. For **configuration 8**, i.e. when the ASET constitutes of rotational DOFs only, no eigenfrequencies are obtained due to matrix singularity, which indicates that at least one translational DOF must be included in the ASET. An important observation from the figure is that symmetry (c.f. **configuration 3** and **4**) gives equal results in terms of eigenfrequencies. Another important observation is that including all

translational DOFs in the ASET (see **configuration 7**) results in eigenfrequencies that visually equal the ones obtained from solving the full EVP.

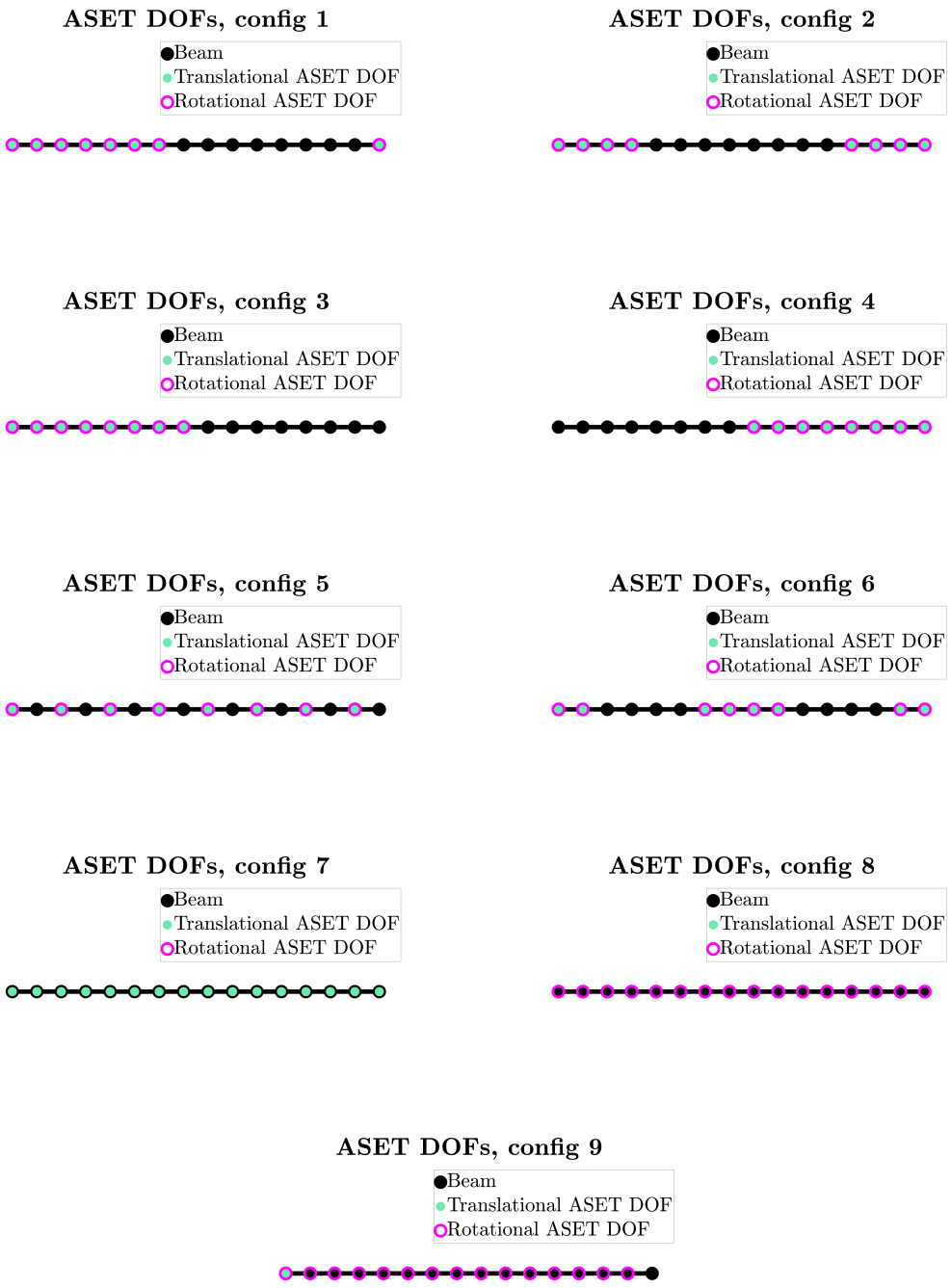

Figure 3.11: ASET configurations for studying the impact of the distribution of ASET DOFs for Guyan reduction. Note that all configurations include 50% of the DOFs for the ASET.

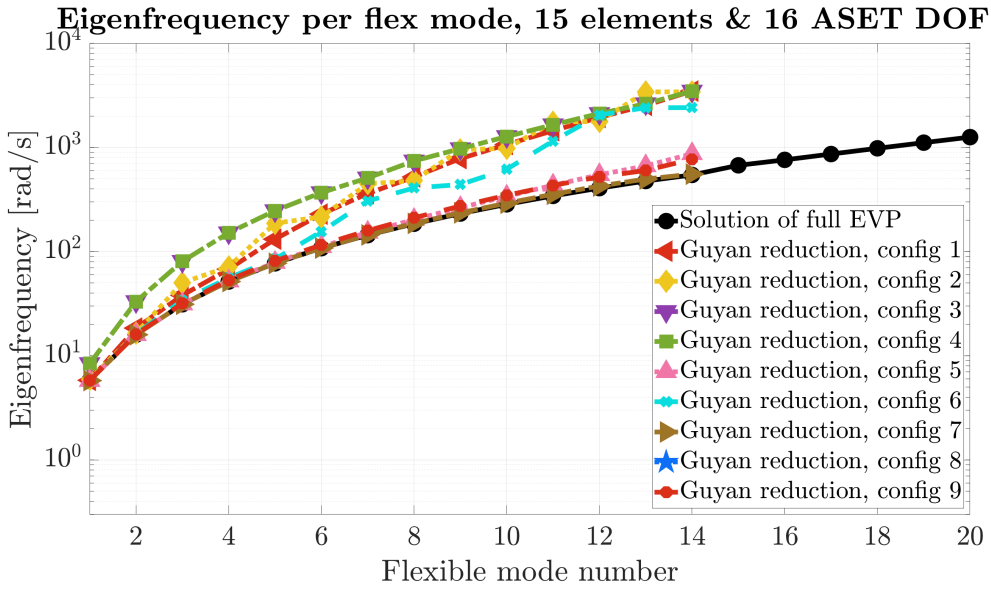

Figure 3.12: Eigenfrequency per flexible mode number 1-20 for the ASET configurations in Figure 3.11.

In order to assess whether configuration 7 from Figure 3.11 provides a perfect solution even though the size of the EVP is reduced by half, the MAC has been evaluated (recall equation (2.16)). The results are presented in Table 3.2. From the table it follows that the motion of the first mode, which is a rigid body mode (RBM), is captured very poorly, but the translational DOFs are captured to at least 96% for all flexible modes, which is considered to constitute a very good match. In total, the flexible modes are captured up to at least 88%, and in particular it can be noted that the shape of the first 7 flexible modes are captured perfectly.

Table 3.2: MAC for configuration 7 from Figure 3.12.

Mode number	Translation	Rotation	Total MAC
1	0.24	0.70	0.03
2	0.41	1.00	0.89
3	1.00	1.00	1.00
4	1.00	1.00	1.00
5	1.00	1.00	1.00
6	1.00	1.00	1.00
7	1.00	1.00	1.00
8	1.00	1.00	1.00
9	1.00	1.00	1.00
10	1.00	0.99	0.99
11	1.00	0.98	0.98
12	1.00	0.97	0.97
13	1.00	0.94	0.94
14	1.00	0.91	0.91

Continued on next page

Table 3.2 – continued from previous page

Mode number	Translation	Rotation	Total MAC
15	0.99	0.88	0.88
16	0.96	0.96	0.96

3.3 Craig-Bampton exemplified

In order to illustrate the Craig-Bampton reduction, the discretized beam from Figure 3.1 is studied once again. Initially, the ASET is defined by all DOFs at the two end nodes as visualized in Figure 3.5 and 3.9, respectively. As for the Guyan reduction, the DOFs must be reordered in order to obtain the structure of $\hat{\boldsymbol{M}}$ and $\hat{\boldsymbol{K}}$ from equation (3.8) and (3.9), respectively.

Furthermore, for the initial example, four fixed interface modes are to be included in the reduction matrix $\boldsymbol{R}$. The first four modes, originating from solving equation (2.32) with $\boldsymbol{M}_{bb}$ and $\boldsymbol{K}_{bb}$, defined by equations (3.11) and (3.12), are visualized in Figure 3.13. The mode shapes originating from the studied beam with 15 elements are displayed in red, yellow, purple and green respectively. A reference solution using 500 elements is also included in black. When comparing the shape and eigenvalues from the different discretizations, it can be seen that the number of elements affects both the shape and the eigenfrequency of each mode. Furthermore, it follows from Figure 3.14 that the eigenfrequencies are affected by the discretization even though the shape has converged. This is a difference compared to the static correction modes from Figure 3.6 that constitute an exact approximation of the static reference solution.

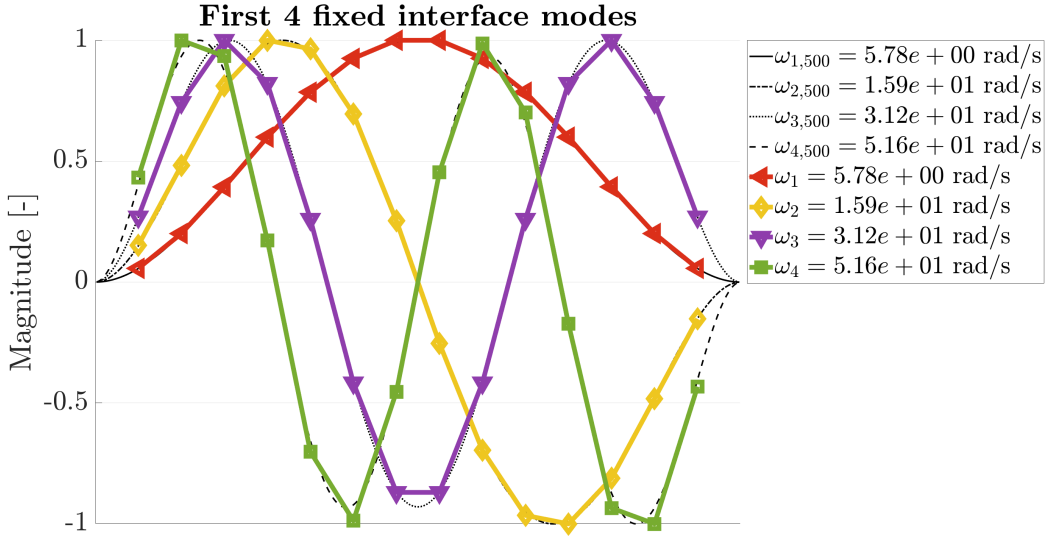

Figure 3.13: Four first fixed interface modes originating from solving equation (2.32).

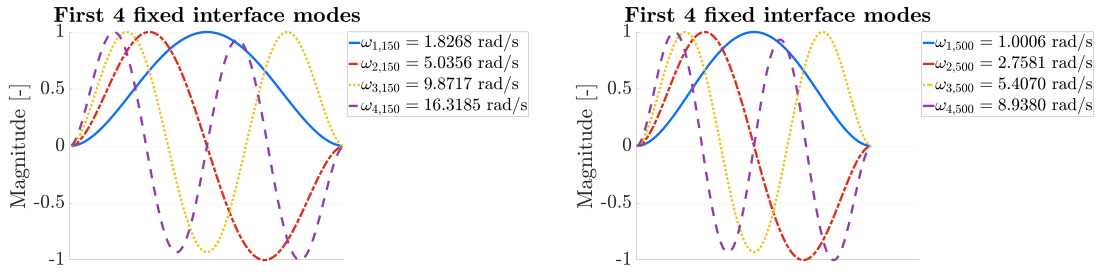

(a) **(b)**

Figure 3.14: First four fixed interface modes and corresponding frequencies. EVP solved with (a) 150 elements and (b) 500 elements.

However, continuing with the discretization including 15 elements, the colored modes from Figure 3.13 can be plugged into the reduction matrix $\boldsymbol{R}$ along with the static correction modes presented in Figure 3.6. Now, $\bar{\boldsymbol{M}}$ and $\bar{\boldsymbol{K}}$ from equation (2.35), can be obtained as

$$\bar{\boldsymbol{M}}_{8\times 8} = \boldsymbol{R}^T \hat{\boldsymbol{M}} \boldsymbol{R}, \quad \bar{\boldsymbol{K}}_{8\times 8} = \boldsymbol{R}^T \hat{\boldsymbol{K}} \boldsymbol{R}. \tag{3.21}$$

Again considering free vibrations, the EVP described by equation (3.16) can be solved. The size of the EVP to solve is now 8×8 since four static correction modes and four fixed interface modes have been included in the reduction. For unit parameters, the solution of the 8×8 EVP read

$$\tilde{\boldsymbol{\Phi}} = \begin{bmatrix} | & | & | & | & | & | & | & | \\ \tilde{\boldsymbol{\varphi}}_1 & \tilde{\boldsymbol{\varphi}}_2 & \tilde{\boldsymbol{\varphi}}_3 & \tilde{\boldsymbol{\varphi}}_4 & \tilde{\boldsymbol{\varphi}}_5 & \tilde{\boldsymbol{\varphi}}_6 & \tilde{\boldsymbol{\varphi}}_7 & \tilde{\boldsymbol{\varphi}}_8 \\ | & | & | & | & | & | & | & | \end{bmatrix}$$

$$= \begin{bmatrix} -0.1077 & -0.6768 & 0.2152 & 0.1274 & 0.0918 & -0.0715 & 0.0313 & 0.0257 \\ -0.8923 & 1.0000 & -1.0000 & -1.0000 & -1.0000 & 1.0000 & -1.0000 & -1.0000 \\ -1.0000 & 0.3232 & 0.2152 & -0.1274 & 0.0918 & 0.0715 & 0.0313 & -0.0257 \\ -0.8923 & 1.0000 & 1.0000 & -1.0000 & 1.0000 & 1.0000 & 1.0000 & -1.0000 \\ -0.0000 & -0.0000 & -0.2291 & -0.0000 & 0.4110 & -0.0000 & 0.5927 & 0.0000 \\ 0.0000 & -0.0000 & -0.0000 & 0.1838 & 0.0000 & 0.1215 & 0.0000 & -0.2015 \\ 0.0000 & 0.0000 & 0.0062 & 0.0000 & -0.1416 & 0.0000 & 0.0879 & 0.0000 \\ -0.0000 & -0.0000 & -0.0000 & -0.0065 & -0.0000 & -0.1147 & 0.0000 & -0.0522 \end{bmatrix} \tag{3.22}$$

with corresponding eigenvalues

$$\tilde{\boldsymbol{\Omega}} = \begin{bmatrix} \tilde{\omega}_1 \\ \tilde{\omega}_2 \\ \tilde{\omega}_3 \\ \tilde{\omega}_4 \\ \tilde{\omega}_5 \\ \tilde{\omega}_6 \\ \tilde{\omega}_7 \\ \tilde{\omega}_8 \end{bmatrix} = \begin{bmatrix} 0.0000 \\ 0.0000 \\ 5.7791 \\ 15.9390 \\ 31.3547 \\ 51.8246 \\ 150.3267 \\ 219.5918 \end{bmatrix} \text{ rad/s}. \tag{3.23}$$

With the reduced EVP solved, the motion of the BSET DOFs can be obtained using the reduction matrix $\boldsymbol{R}$ according to

$$\tilde{q} = \boldsymbol{R}^T \boldsymbol{q}_a, \tag{3.24}$$

and then the motion of mode i can be obtained as

$$\boldsymbol{q}_{a,i} = \tilde{\boldsymbol{\varphi}} \cos\left(\tilde{\omega}_i t\right). \tag{3.25}$$

Transforming back to the original 32 DOFs according to equation (3.24), as for the Guyan reduction, the mode shapes represented in Figure 3.15 are obtained. Similarly as for the Guyan reduction, it is observed that the first two modes are RBMs with eigenfrequeiencies close to 0 rad/s, which is expected. However, as for the Guyan reduction, there are no pure translational or rotational RBMs, which is expected from solving the full EVP. Furthermore, from Figure 3.15 it follows that for the third and fourth modes (the first and second flexible mode) the shape and eigenfrequencies are (almost) identical to the ones obtained by solving the full 32 DOF EVP, see black mode shapes in the figure. Additionally, the fifth and sixth mode appear to be very similar to the full reference solution in both mode shape and eigenfrequency. In contrast to those observations, the seventh and eight eigenmodes show differences in shape and corresponding eigenfrequency.

From Figure 3.15 it follows that the first four flexible eigenmodes, i.e. mode three to six in the figure, match the full solution. Furthermore, it is observed that the RBMs and higher flexible modes, i.e. mode one, two, seven and eight, differ from the full solution. In order to asses to what extent the eigenmodes correlate to the full solution, the MAC has been evaluated according to equation (2.16) and the results are presented in Table 3.3. From the table it follows that the correspondence in translation and rotation is above 0.56 for all modes. Furthermore, it can be seen that mode number three to six have a MAC of 1.00, which implies that the mode shapes are equal. Hence it seems like a Craig-Bampton reduction with four fixed interface modes and ASET DOFs according to Figure 3.5, can capture the first four flexible eigenmodes accurately.

Table 3.3: MAC for modes of Craig-Bampton reduction compared to the corresponding modes from the solution of the full problem.

Mode number	**Translation**	**Rotation**	**Total MAC**
1	0.80	0.70	0.26
2	0.75	1.00	0.97
3	1.00	1.00	1.00
4	1.00	1.00	1.00
5	1.00	1.00	1.00
6	1.00	1.00	1.00
7	0.78	0.61	0.61
8	0.74	0.56	0.56

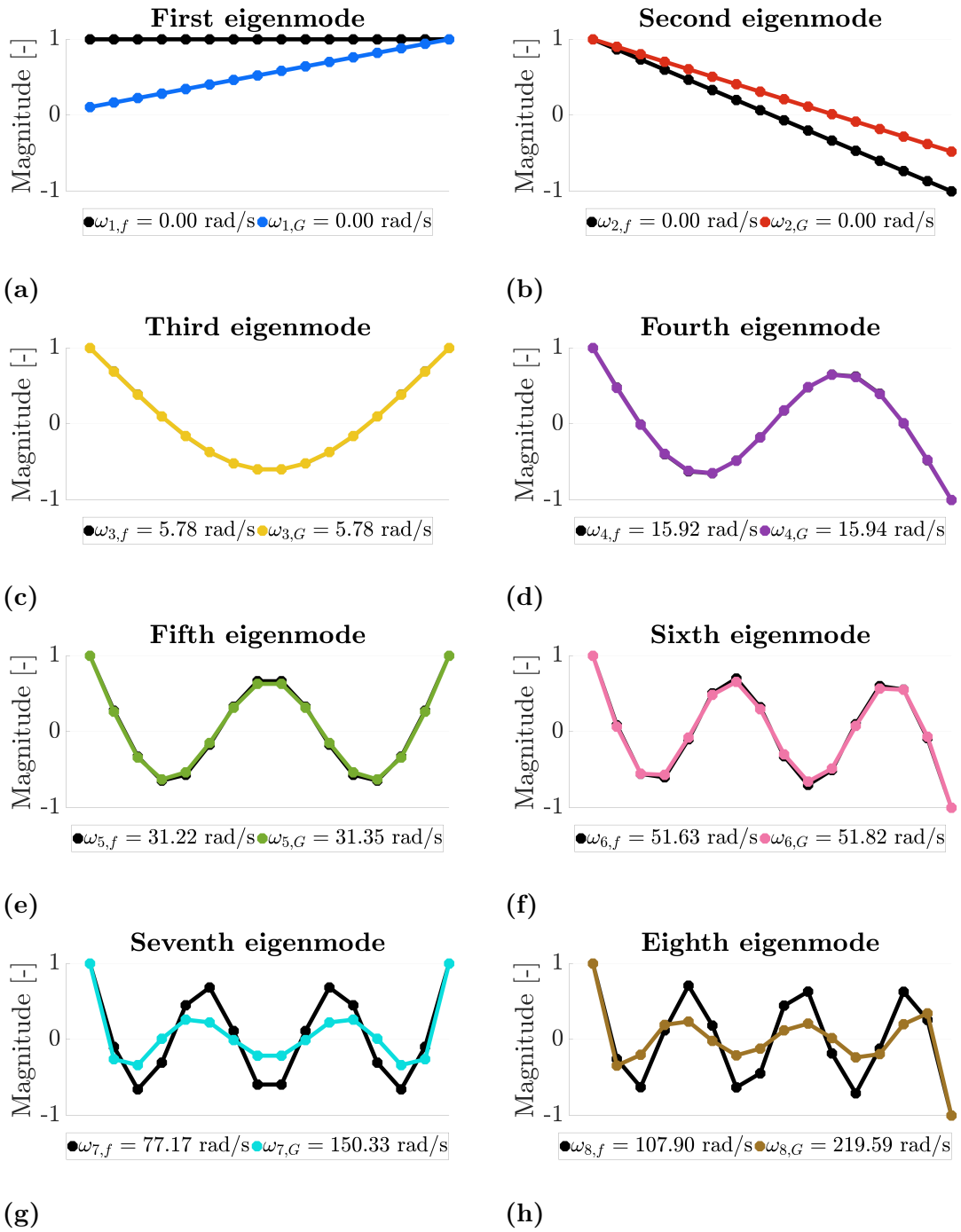

Figure 3.15: In (a) first, (b) second, (c) third, (d) fourth, (e) fifth, (f) sixth, (g) seventh, and (h) eight eigenmode after Craig-Bampton reduction including the four fixed interface modes represented in Figure 3.13 with ASET DOFs according to Figure 3.5. For each mode, the unreduced (i.e. full) solution is included in black.

3.3.1 Including more modes in the reduction

In order to investigate the dependence on the number of fixed interface modes included in the reduction, the EVP has been reduced with the four ASET DOFs depicted in Figure 3.5 and with different number of modes included in the reduction

matrix $\boldsymbol{R}$. The eigenfrequencies of the first twenty flexible modes are presented in Figure 3.16. From the figure it follows that the number of fixed interface modes included in the reduction has an impact on which (and how many) flexible modes that can be accurately represented by the CMS. In particular, it can be seen that the Guyan reduction (which is nothing but a Craig-Bampton with 0 fixed interface modes), is close to the expected eigenfrequency of the first mode, but slightly larger than what is expected from solving the full EVP.

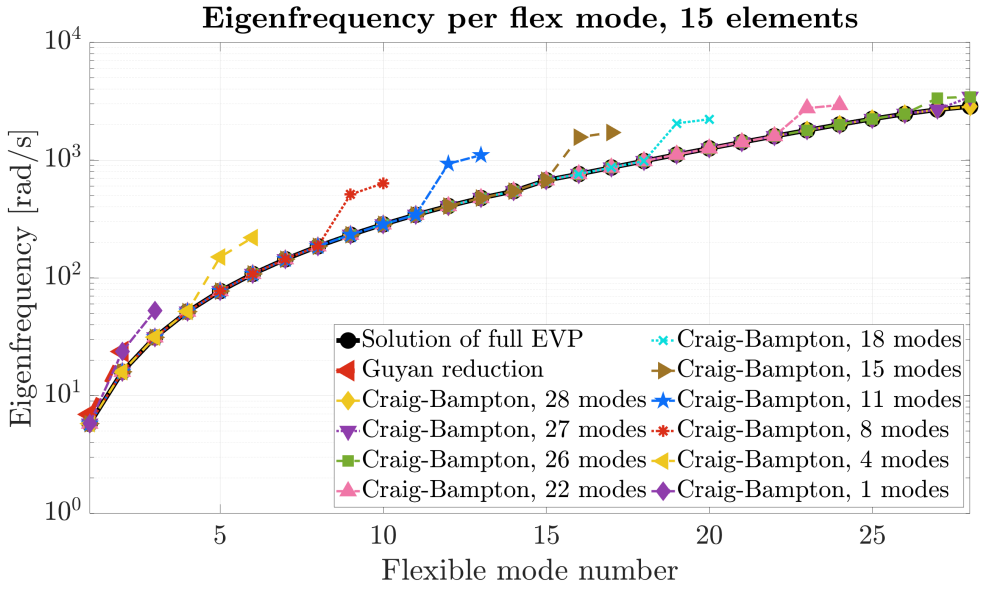

Figure 3.16: Eigenfrequency of the flexible modes for different number of fixed interface modes included in the Craig-Bampton reduction. ASET distribution according to Figure 3.5.

In contrast, including all possible 28 fixed interface modes results in a visually perfect match to the full solution. In order to asses whether this is the case, the MAC has been evaluated according to equation (2.16). From the MAC evaluation it follows that all flexible modes are represented perfectly, which is expected since including all possible fixed interface modes implies a transformation of the EVP, but no reduction is size. In order to assess how many fixed interface modes are needed to accurately represent flexible modes up to a certain number, the relationship has been visualized in Figure 3.17. From Figure 3.17 it follows that, for the selection of ASET DOFs represented in Figure 3.5, it seems like the required number of fixed interface modes correspond to the number of the highest flexible mode that should be accurately represented.

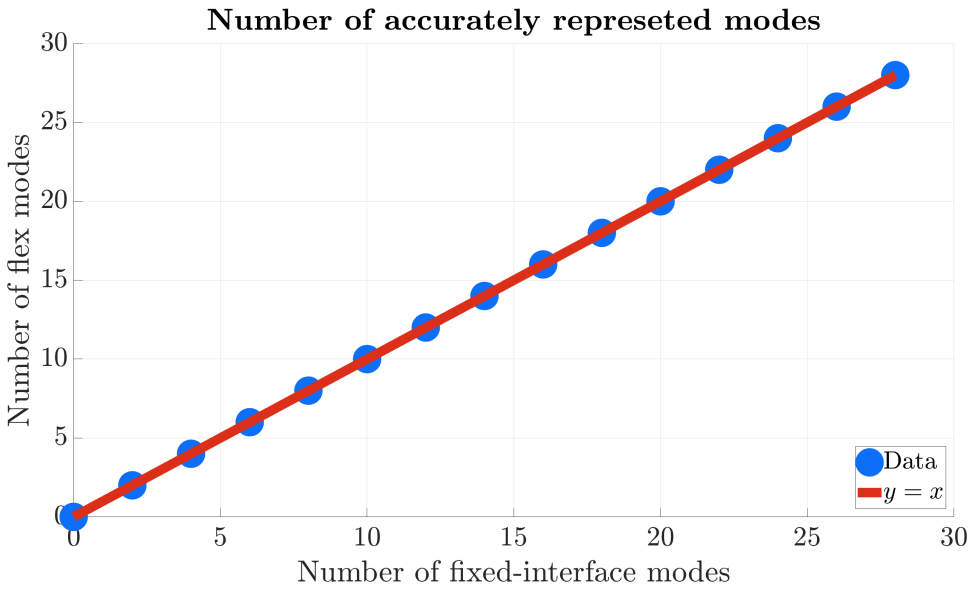

Figure 3.17: Number of flexible modes that can be accurately represented vs. fixed interface modes included in the reduction for the distribution in Figure 3.5.

3.3.2 Different number of ASET degrees of freedom

For the Guyan reduction, it has been seen that the distribution of ASET DOFs has an impact on how well the eigenfrequencies and shapes of the flexible modes can be represented. In order to assess whether the number of ASET DOFs has an impact on which modes can be represented accurately, **distribution 2** from Figure 3.9 (which includes ten ASET DOFs) has been considered. The resulting eigenfrequencies are represented in Figure 3.18.

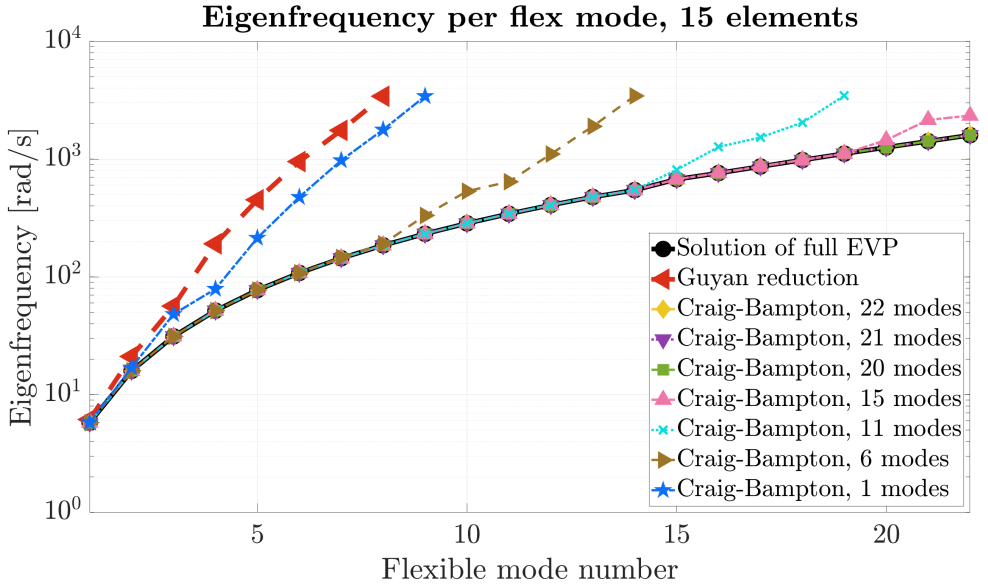

Figure 3.18: Eigenfrequency per flexible mode for different number of fixed interface modes and Craig-Bampton reduction for the ASET distribution 2 in Figure 3.9.

Comparing Figure 3.18 to Figure 3.16 suggests that the number of ASET DOFs affect the number of fixed interface modes that need to be included in the reduction in order to accurately represent the eigenfrequencies. The number of flexible modes that can be represented from a certain number of fixed interface modes has been studied, see appendix B.1 for an illustration similar to the Figure 3.18, and the results are presented in Figure 3.19. From Figure 3.19 it follows, as expected from comparing Figure 3.18 with Figure 3.16, that the assumption of $y = x$ is no longer a good representation of how many flexible modes y that can be accurately represented for a certain number of fixed interface modes x. Instead, two linear regressions have been made. One of the linear regressions has been made using the built-in Matlab® function `polyfit` (see the red graph in the figure) and the second one using the relation

$$k = \frac{\Delta y}{\Delta x}, \tag{3.26}$$

where k denotes the slope. Both methods result in a slope close to 1.3 and hence it seems like fewer fixed interface modes are needed in order to accurately represent a certain number of flexible modes for the ASET being defined by ten DOFs than for the case of the ASET being defined by four DOFs.

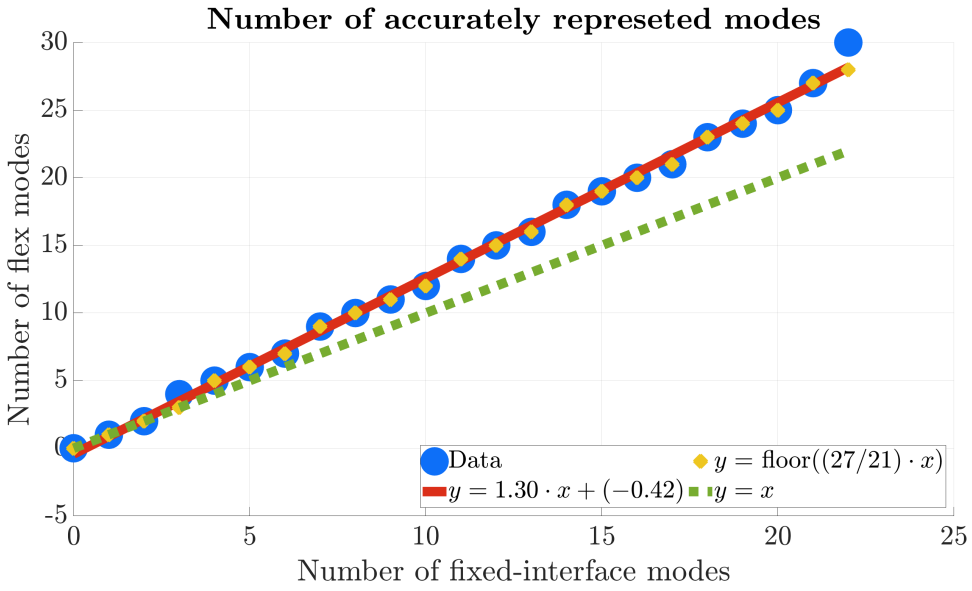

Figure 3.19: Number of flexible modes that can be accurately represented vs. fixed interface modes included in the reduction for distribution 2 in Figure 3.9.

3.3.3 Different distribution of ASET degrees of freedom

Apart from indicating that the number of ASET DOFs has an impact on the number of flexible modes that can be accurately represented, the Guyan reduction illustrated that also the distribution of the ASET DOFs affects how well and which flexible modes that can be accurately represented. As a final example of the Craig-Bampton reduction, the distribution of the ASET DOFs is investigated. The new ASET distribution is presented in Figure 3.20 and the results of the reduction are presented in Figure 3.21.

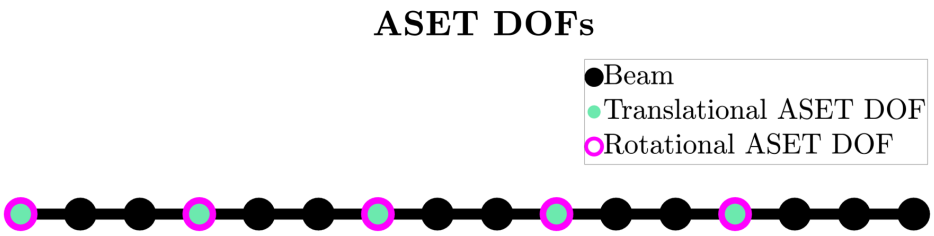

Figure 3.20: Additional ASET distribution including 10 DOFs.

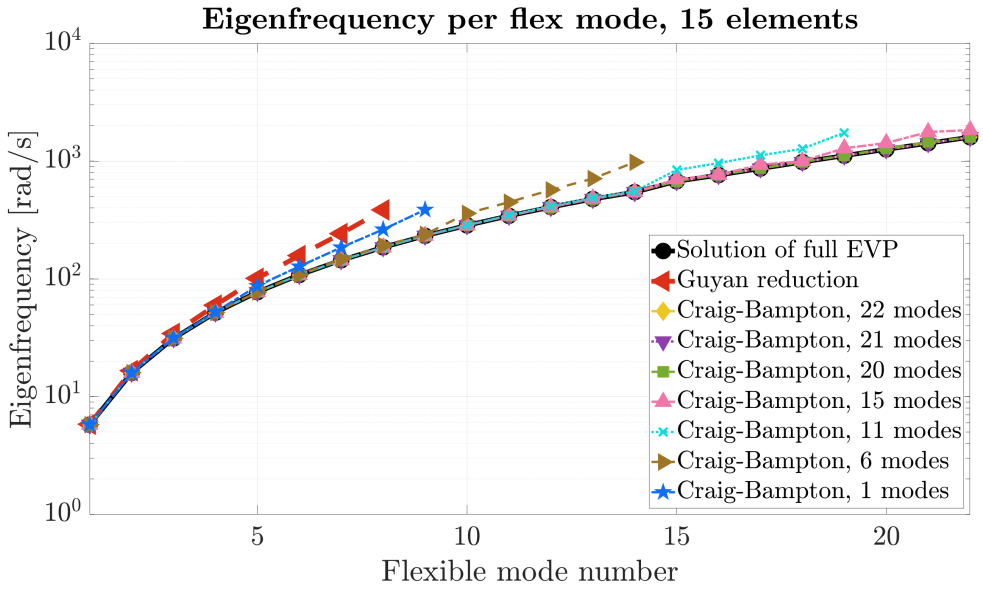

Figure 3.21: Eigenfrequency per flexible mode for different number of fixed interface modes and Craig-Bampton reduction for the ASET distribution in Figure 3.20.

Comparing Figure 3.18 and Figure 3.21 it follows that the calculated frequencies are closer to the expectation from solving the full EVP for all flexible modes represented for the new distribution of Figure 3.21 than for the original ten-DOF distribution of Figure 3.18. A similar representation to the one in Figure 3.19, of the relationship between the number of fixed interface modes and the number of flexible modes that can be accurately represented, is presented in Figure 3.22.

From Figure 3.22 it follows that the relationship between the number of fixed interface modes and the number of accurately represented eigenfrequencies is more complex than for the previous cases. It seems like a second degree polynomial might be needed in order to represent the relationship. An additional linear regression (the solid red line) has been calculated. It has a similar slope as the previously regressed one (the solid red line in Figure 3.19). One interesting observation is that the slope is steeper for the solid red line in Figure 3.19 than for the one in Figure 3.22, which suggest that more fixed interface modes should be included for the new distribution presented in Figure 3.20. This is interesting since the general behavior is that all computed frequencies are closer to the analytical solution in Figure 3.21 than in Figure 3.18. However, as previously stated, the slopes are similar, and the

fact that the values are read from graphical representations, it may be interpreted that the distribution of ASET DOFs has a minor impact on the number of modes that can be accurately represented in the case of Craig-Bampton reduction.

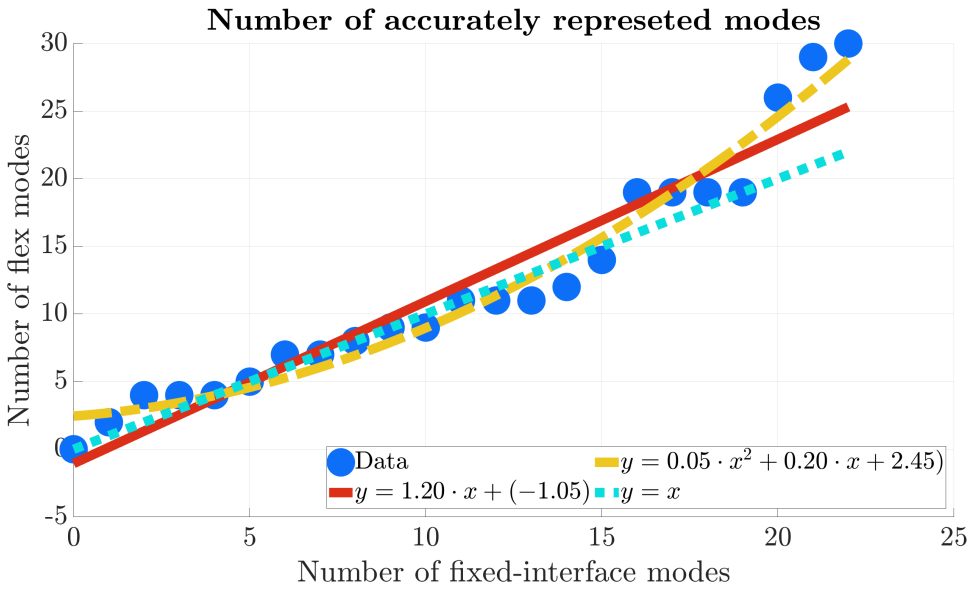

Figure 3.22: Number of flexible modes that can be accurately represented vs. fixed interface modes included in the reduction for the distribution of Figure 3.20. Number of flexible modes read from Figure 3.21 complemented by Appendix B.2.

3.4 Rigid body motion test

To understand how a RBM can be identified in measurements and how it connects to the simulated measurements, a simple test rig of a beam was built in steel with the length of one meter, see section 2.6.1. During the test, two accelerometers, one at each end, were placed on the test rig. The accelerometer at the far right end in Figure 3.23 is referred to as the master accelerometer since it experiences the largest motions. In contrast, the accelerometer placed at the far left end of the beam is referred to as the slave accelerometer.

The test rig and the accelerometers are shown in Figure 3.23, together with the coordinate frame used for the measurements. As presented in the figure, the X-axis is defined in the direction of the beam, the Y-axis is oriented upwards, and the Z-axis points out of the plane. Studying the figure closely the orientation of the Z-axis is also visible on the accelerometers. The accelerometers used in this test only measure changes of acceleration in the translational directions, i.e in the X-,Y- and Z-directions. There are accelerometers that can measure rotational angles, but this kind of accelerometer have been unavailable during the measurements. Since the used accelerometers can only measure changes in acceleration in the translational directions, the rotations must be taken into consideration and be neglected in the post-processing of the data. For this beam example, the rotation of the master

and slave accelerometers is equal and hence the movement is represented by the difference between the master and slave accelerometers.

(a)

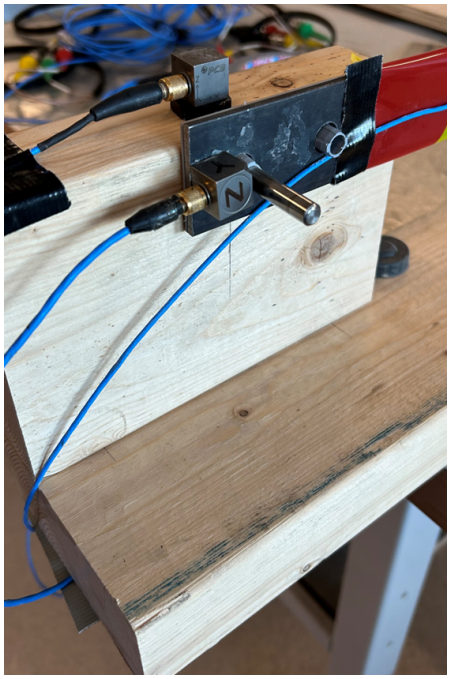

(b)

(c)

Figure 3.23: In (a) physical test rig of the beam, (b) slave accelerometer, and (c) master accelerometer. The circles in (a) indicate the accelerometers.

As a foundation, the analytically expected translations are determined from trigonometry with an assumed angular offset of $\pm 1°$, as illustrated in Figure 3.24. From the trigonometrical calculations, the expected maximum translations are received as approximately 17 mm in the Y-direction and approximately 0.15 mm in the X-direction for a rotational angle of 1°, see Figure 3.24(b). In Figure 3.24(a) it is seen that the maximum value of Y correspond to the uppermost position, and the minimum Y value appear at the bottommost position of the beam. The X coordinate on the other hand, has one minimum at the uppermost position and one minimum at the bottommost position, while the maximum value occurs at the starting point. This means that the frequency of the X-coordinates is twice as large as the frequency for the Y-coordinates. The resulting maximum and minimum values assume that the coordinate origin is placed at the far left side of the beam.

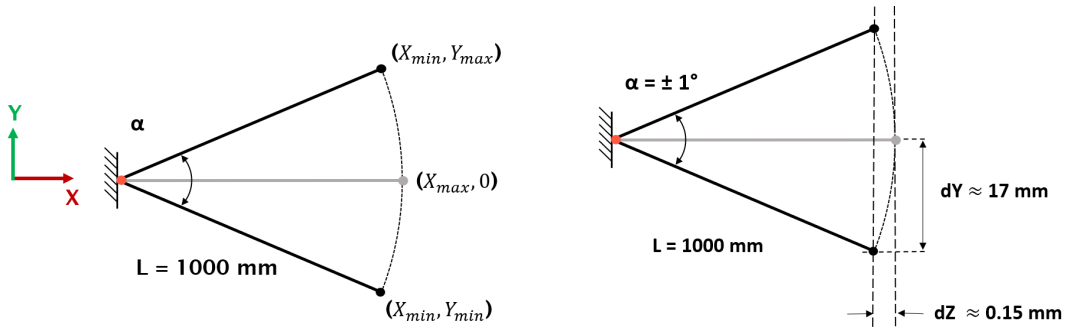

(a) **(b)**

Figure 3.24: Analytical beam representation showing (a) positions corresponding to the extremums in X- and Y-direction and (b) theoretical numerical values for an offset angle of 1°.

For the validation of the imposed RB rotation on the physical test rig, a test indicator watch has been used, see Figure 3.25. The starting value is read to be -2 mm and the value at the end of the imposed circular path is read to be 18 mm, which corresponds to a difference of 20 mm. From the analytical example, the difference is predicted to be 17 mm, which is close to the observed 20 mm. Since the angular offset might have been larger than 1° on the test rig, the differences are considered to correspond to each other. Hence, the difference is a result from a pure rotation around the pivoting point, where the slave accelerometer is placed, and the resulting distance is then a so-called artificial contribution, see section 2.6.1.

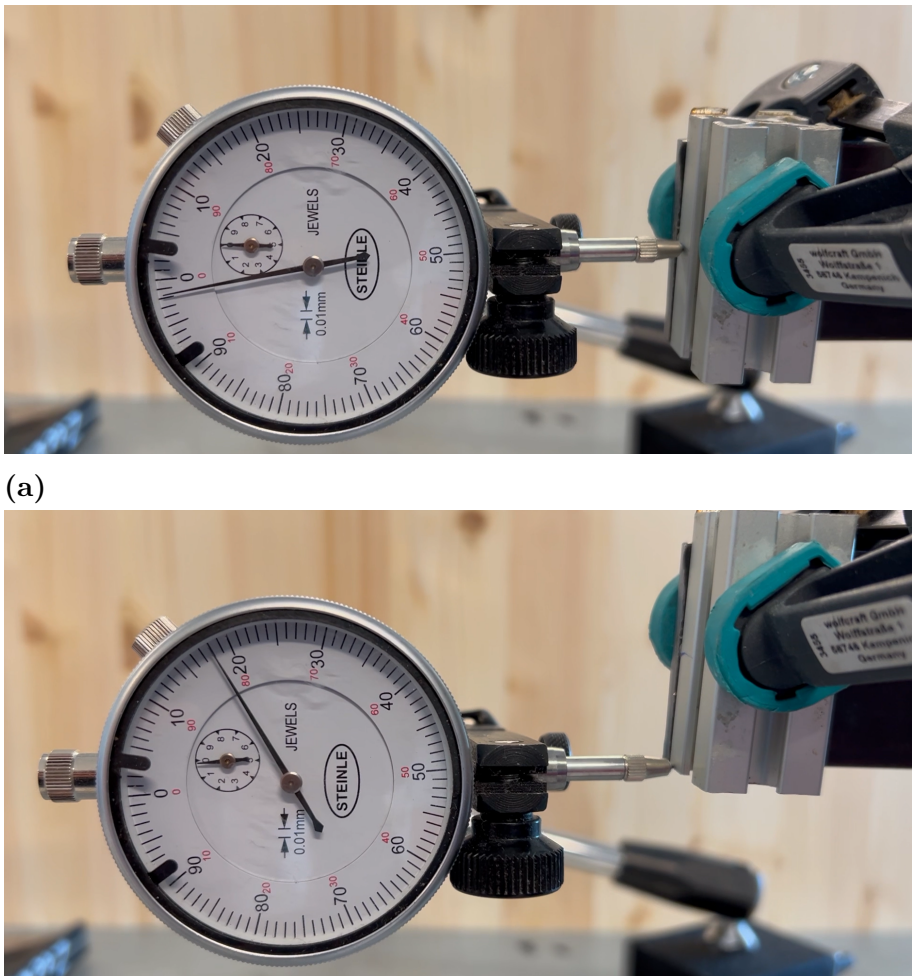

(a)

(b)

Figure 3.25: The beam test rig with a test indicator watch next to the master accelerometer at (a) its starting point and (b) its end point.

3.4.1 Displacements to accelerations

In order to transform the accelerations into displacements, the raw data needed to be filtered, integrated, filtered, integrated and finally filtered once again. The filtration is needed to shift the data such that it fluctuates around zero, which in turn allow disregarding of the integration constant that would otherwise appear. Additionally, the filtration removes high-frequent noise.

The raw acceleration data in the X- and Y-directions are visualized in Figure 3.26, where the red lines represents the master accelerometer, and the blue lines represents the slave accelerometer. In Figure 3.26(a) it is seen that both accelerometers have similar magnitude in the X-direction, while it in Figure 3.26(b) is observed that the master and slave accelerometer readings differ significantly in magnitude in the Y-direction. It makes sense that the the magnitude of the observed acceleration in the Y-direction is larger for the master accelerometer than for the slave accelerometer considering the imposed circular path. However, considering the an-

alytical expectation of the master accelerometer experiencing a translational offset of 0.15 mm in the X-direction, the magnitude of the read accelerations appear to be large.

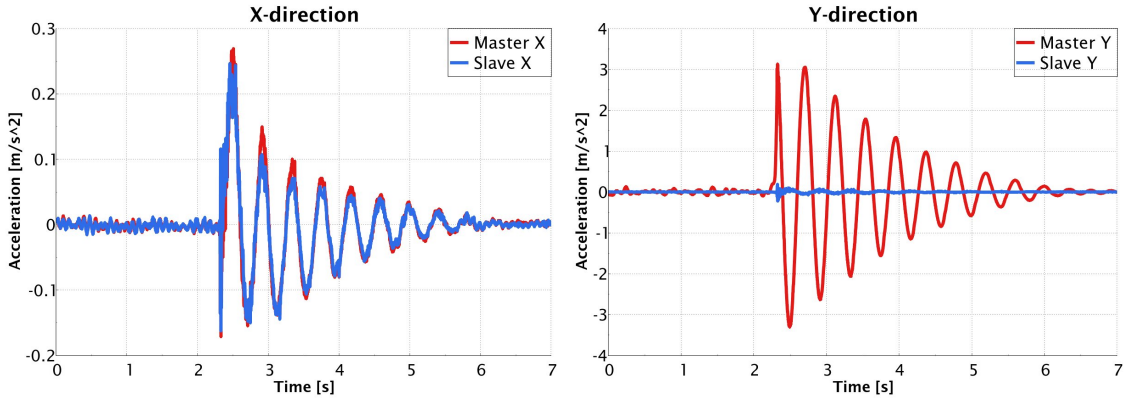

(a) **(b)**

Figure 3.26: Master and slave acceleration time history (a) in X-direction, and (b) in Y-direction.

Filtration of the raw data with a band-pass filter between 1 and 1000 Hz is shown in Figure 3.27. From the filtering, there is a small visible difference compared to the raw data. When integrating the filtered data, velocity time histories is obtained, see Figure 3.28. The filtered velocities are presented in Figure 3.29. Similarly, as observed for the accelerations, the master velocity is considerably larger than the slave velocity in the Y-direction. Considering the circular path, this is expected. Again, similarly as for the accelerations, the magnitudes of the master and slave velocities are very similar in the X-direction. As for the accelerations, the velocities are considered to be large since the maximum magnitude constitute approximately one tenth of the magnitude in the Y-direction, while the analytical expectation is approximately one hundredth of the magnitude in the Y-direction.

The results after the final integration to displacement and the final filtering are presented in Figures 3.30 and 3.31, respectively. For easier comparison with the theoretical calculations, the displacements are multiplied by 1000 to obtain measures in millimeters, see Figure 3.32. As for the accelerations and velocities, it is observed that the expected X-displacement is approximately 0.15 mm, which is considerably smaller than the measured 1 mm. The higher magnitude could originate from how the accelerometers operate. Recalling that the accelerometers measure changes of acceleration in the translational directions, the fact that the accelerometers are rotated and considering that the gravity is an acceleration field, the higher values could be a result of the accelerometers measuring the gravity field. Hence the large magnitude may be a so-called artificial contribution from the pure rotation on both slave and master accelerometers. Since the master and slave accelerometer rotate equally, see Figure 3.32, the artificial contributions should cancel eachother out when subtracting the slave contribution from the master accelerometer data.

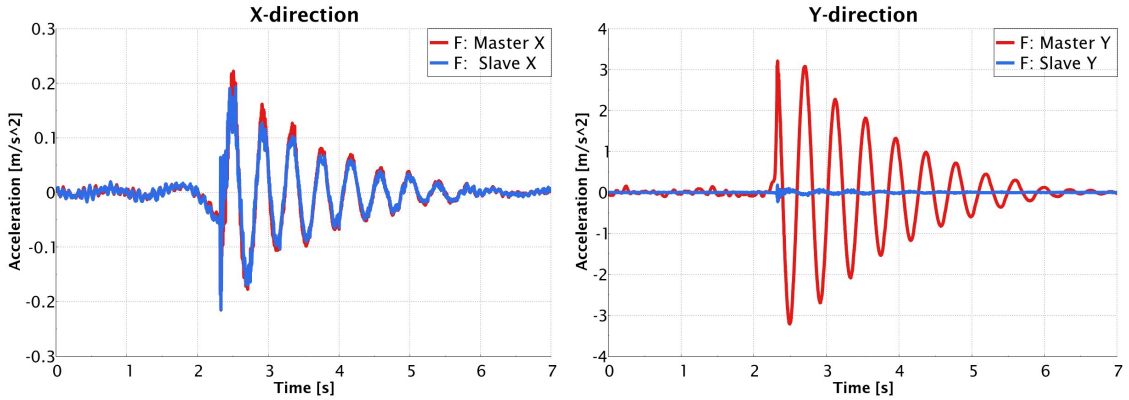

(a) **(b)**

Figure 3.27: Filtered master and slave acceleration time history (a) in X-direction, and (b) in Y-direction. In the legends, F stands for filtered.

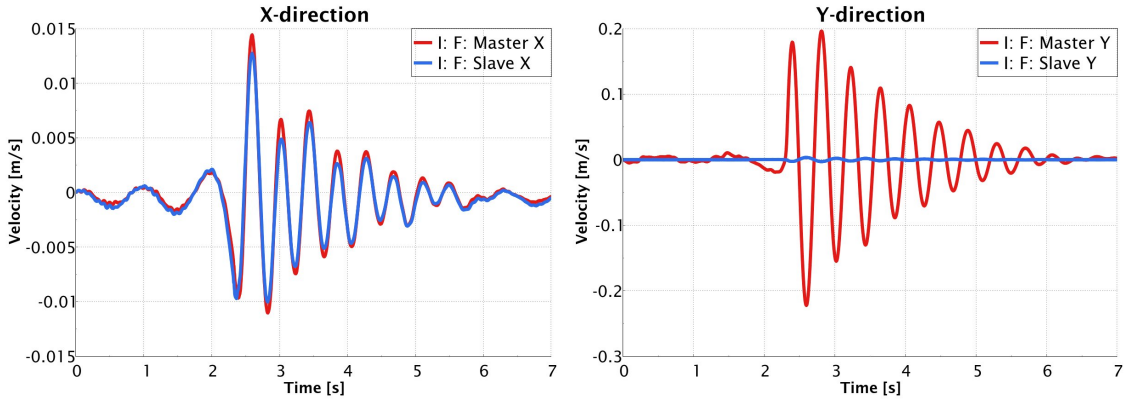

(a) **(b)**

Figure 3.28: Velocity time history of master and slave (a) in X-direction, and (b) in Y-direction. In the legends, F stands for filtered, and I for integrated.

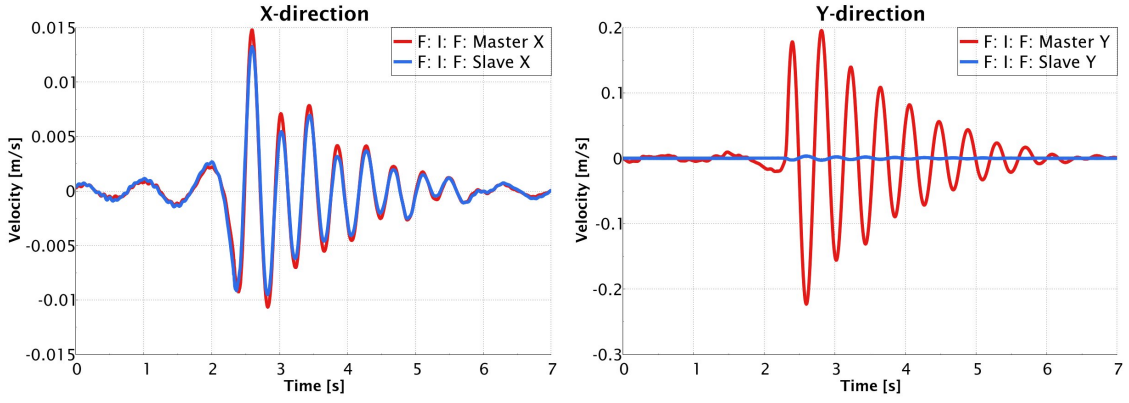

(a) **(b)**

Figure 3.29: Filtered velocity time history of master and slave (a) in X-direction, and (b) in Y-direction. In the legends, F stands for filtered, and I for integrated.

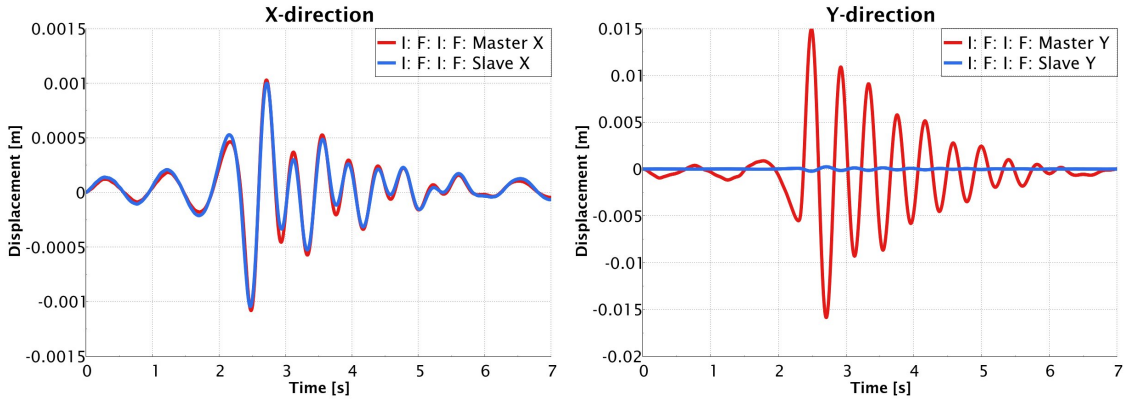

(a) **(b)**

Figure 3.30: Displacement time history of master and slave (a) in X-direction, and (b) in Y-direction. In the legends, F stands for filtered, and I for integrated.

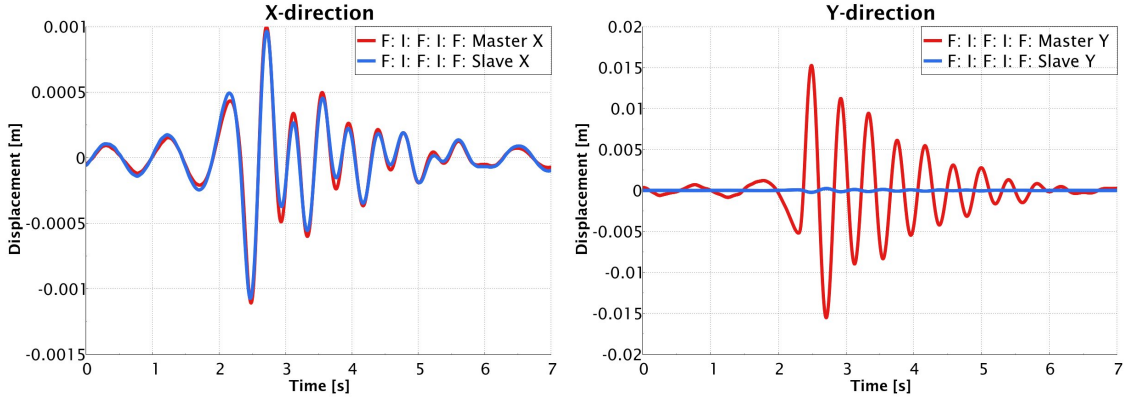

(a) **(b)**

Figure 3.31: Filtered displacement time history of master and slave (a) in X-direction, and (b) in Y-direction. In the legends, F and I for filtered and integrated.

To isolate the imposed circular RB motion, the differences between the master and slave are calculated in both X- and Y-directions. In Figure 3.33, the difference is illustrated. It is observed in Figure 3.33(a) that the magnitude of the Y-difference between the master and the slave accelerometer is considerably larger than in the X-direction. The larger differences in the Y-direction are expected from theory since the master accelerometer experience large movements. However, recalling that the magnitude in the X-direction should be approximately 0.15 mm from a theoretical angular offset of 1°, the observed magnitudes are significantly larger than expected. In the X-direction, the resulting difference is close to zero, which is expected from the analytical calculations. Scaling the X-displacements by a factor 100 in Figure 3.33(b), the magnitude is seen to be about 12 mm, corresponding to 0.12 mm, which is close to the analytically expected value of 0.15 mm. In Figure 3.33(b), it is noted that the phases of the X- and Y-directions are very similar, which constitute a difference to the theoretical foundation where the X-displacement is predicted to have a frequency of two times the frequency of the Y-displacement.

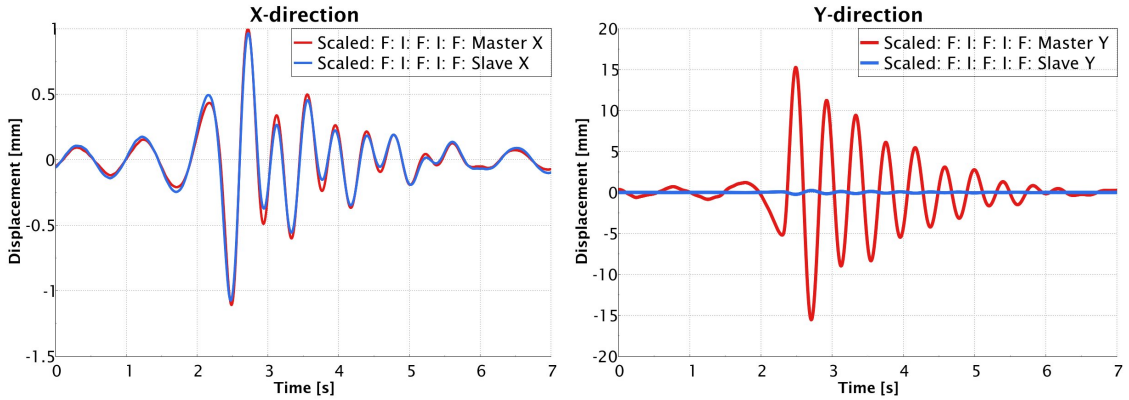

(a) **(b)**

Figure 3.32: Filtered displacement time history of master and slave, scaled to mm, (a) in X-direction, and (b) in Y-direction. In the legends, F and I for filtered and integrated.

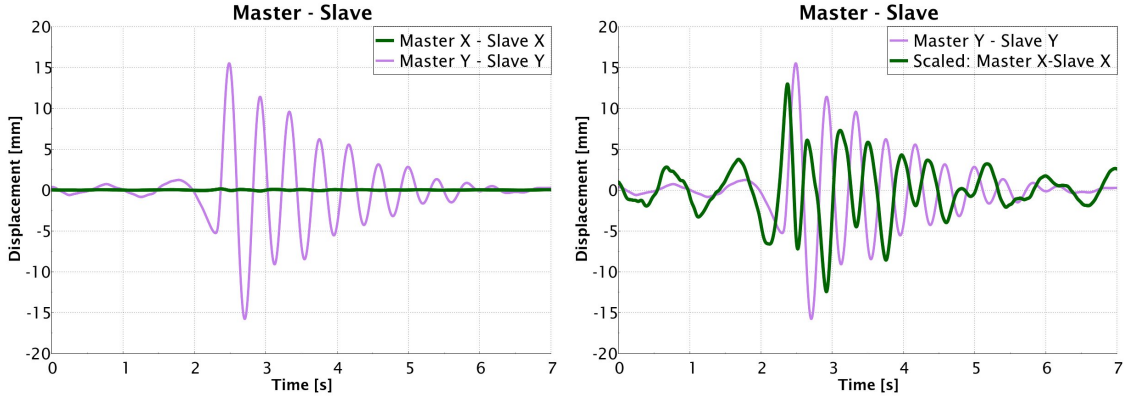

(a) **(b)**

Figure 3.33: In (a) difference between master and slave time history, and (b) the X-displacement time history has been scaled by 100.

For further investigation, the time signal is transformed into the frequency domain through a Fast Fourier Transform (FFT) on the difference between master and slave in X-direction has been performed on raw acceleration data, see Figure 3.34. In the figure there are three clear peaks of approximately 1 Hz, 2.4 Hz and 4.8 Hz, which indicate that something is happening at higher frequencies. If the data is filtered with a high-pass filter above a frequency between 2.4 Hz and 4.8 Hz, the theoretically expected behavior can be observed, see Figure 3.35. The filtering should ensure that the phases of the relative displacement in X and Y directions correspond to the analytical expectation described in Figure 3.24(a). The data in the X-direction is observed to have the doubled frequency compared to the Y-direction in Figure 3.35, which is expected from the theoretical calculations and schematic representation in Figure 3.24(a).

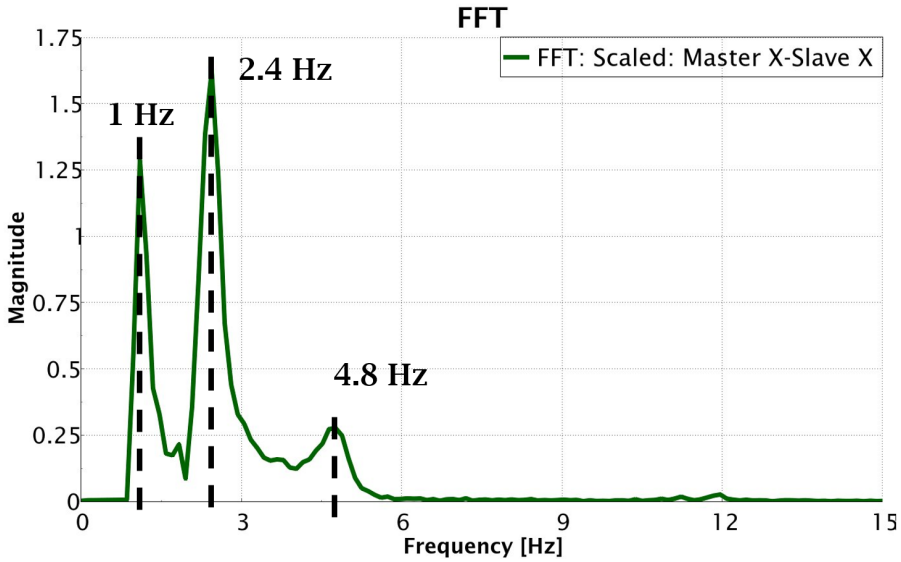

Figure 3.34: FFT of difference between master and slave time history in the X-direction.

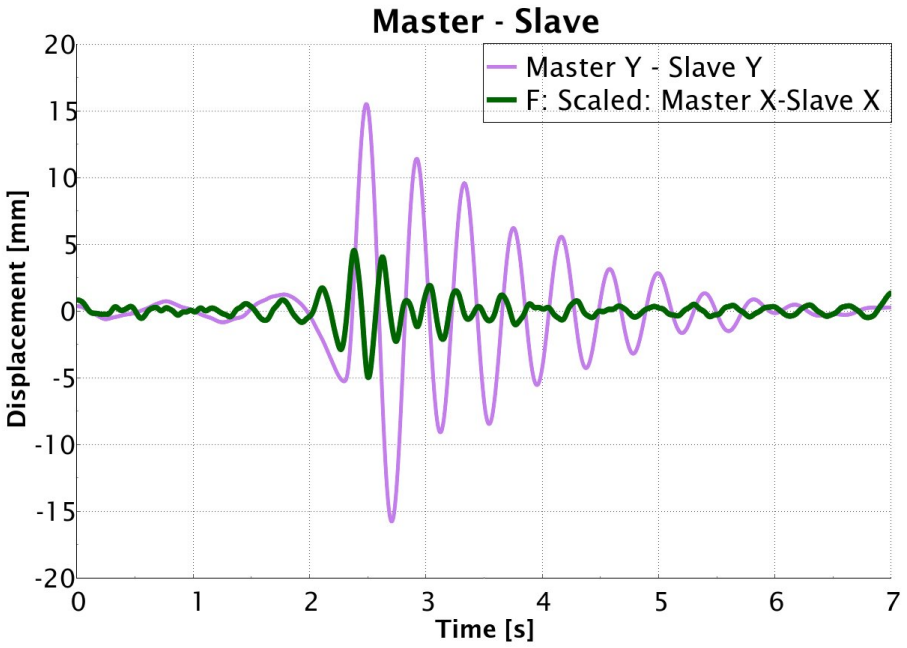

Figure 3.35: Difference between master and slave displacement time history in the Y-direction, and filtered difference between master and scaled slave in X-direction. The displacement time direction in the X-direction is scaled by 100.

For the experimental data presented in Figure 3.35, the difference between the lowest and highest value in the X-direction is found to be slightly below 0.1 mm considering the green graph, which is close to the theoretical expectation.

4

Methods

In order to avoid misunderstandings regarding too good results and the consequences thereof discussed in section 1.5, transparency of the study is important. Assumptions in the modeling are to be clearly stated together with potential limitations in simulation and test. Addressing the limitations of the results may also be a part of the transparency. Additionally, the measures and interpretation of results intend to be explicitly articulated.

An overview of the project methodology is presented in Figure 4.1. As visualized, the project started with a planning and software introduction phase. During this phase, a planing report including a Gantt schedule was developed for planning purposes. Additionally, this phase included introductions to Ansa, Meta, Nastran and Adams. For the software introduction, simplified models were used to facilitate understanding of critical parameters affecting the ODF.

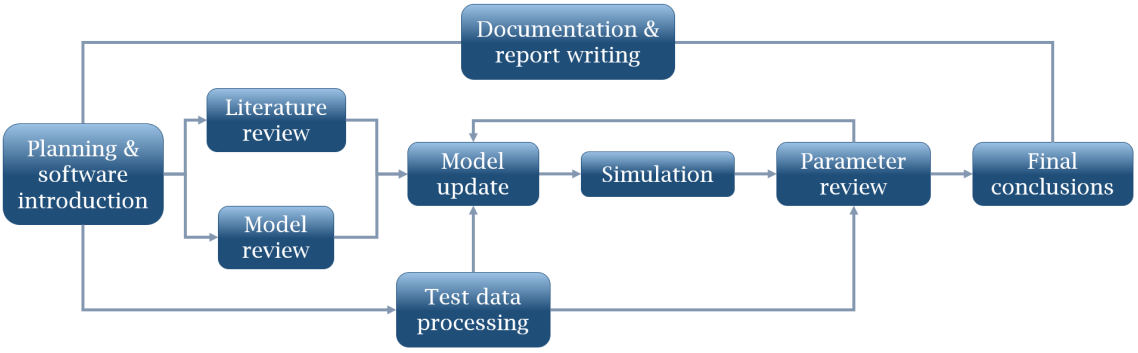

Figure 4.1: Project workflow overview.

After the planning and software introduction phase, a literature review was conducted regarding CMS and how the different parameters in the FE and MDB models could affect the results. In parallel to the literature review, a review of the model representing the Waymo robot-taxi was conducted. This phase included ensuring that the FE and MBD models were up to date considering the test vehicle setup. With reviewed models, the next step of model updating concerned the parameters of interest. During the *model update* phase, the undamped SDE of free vibration ($\boldsymbol{M\ddot{u}}+\boldsymbol{Ku}=\boldsymbol{0}$) was solved and converted to the MNF used in the MBD simulation where the excitation was applied, as illustrated in Figure 1.4.

The resulting ODF of the test data and the simulation data were compared post running the model. After the comparison of the opening distortion fingerprints (ODFs), the project moved back to the *model update* phase in order to study the impact of the next parameter. Finally, when the project approached its end, the results were reviewed and final conclusions were drawn. Documentation and report writing were conducted continuously throughout the project.

4.1 Fully trimmed body into multibody dynamics

For this thesis, a modal analysis by Nastran (SOL 103) was used to create MNFs from the FE model. The modal analysis was also used as a guide for how the fully trimmed body behaves at different frequencies. The modal analysis gave the eigenmodes of the structure, where modes within a frequency range was requested. From the modal analysis, the inertia relief residual vectors [21] and the eigenmodes were orthonormalized [20].

To access the FE model in an MBD environment, the FE model is transformed into an MNF. The MNF includes the fully trimmed body model and information about node locations and mode shapes. When loading the MNF into the MBD software Adams, the MNF represents a flexible body. The binary MNF format can be used on all platforms where Adams's products can be run [30]. Simulations in the MBD environment were run with the road corresponding to the Belgian pavé test track at Hällered Proving Ground, Sweden, where the test was performed. The specific road data was together with the driver instructions for Belgian pavé accessed through Zeekr's database for Adams.

4.2 Correlation approach

For the correlation between simulation and test data, a base simulation model was used. Throughout the parameter study, the base model had fixed parameters of all included parts, such as damping and ASET DOFs. During the parameter study, one parameter was changed at a time in order to assess what parameters have an impact on the correlation. The results were presented in an ODF, to see if there were any differences compared to the base model and the test data. Parameters were changed for the MNF creation, in the MBD model and in the post-processing. The base model was driven on Belgian pavé at 30 km/h with a tire model based on measurements. There are however differences in the simulated tires compared to the measured tires. The simulated tires are larger than the ones on the test vehicle, due to lack of measurements for the correct tires.

4.3 Physical measurements

The acceleration data obtained from simulation and test has been processed in the post-processor Meta. As an initial step in Meta, timesignal data from test or the MBD simulation was read. There is an opportunity to trim the time signal before

the data is processed in time-domain to obtain displacements in the ODF tool. The data processing in Meta includes filtering and integration. The filtration of the data is done through multiple bandpass filters (R. Varela de Albuquerque, unpublished script, 2020). Additionally, using the Meta built-in ODF tool, so-called leakage that might introduce errors, should be prevented. A practical example of filtering and integration of test data is presented in section 3.4. In addition to integration and filtering, the data may also be transformed from global coordinates to local coordinates to find the diagonal distortions (R. Varela de Albuquerque, unpublished script, 2020).

4.4 Use of artificial intelligence

For this thesis, AI has been used for grammatical and formational improvement suggestions of the text in this report. AI has also been used for finding better words or synonyms, but the AI suggested words are not necessarily used in this final text. In addition to finding appropriate words, AI has been used to find functions and libraries for programming. For pure code generation of bigger snippets, AI has not been used.

5

Results & Discussion

The chapter includes the results from the performed parameter study. Unless otherwise stated, all ODF results originate from the E-line method in the z-direction with an SEP of 20%. An overview of the studied parameter setups are presented in Table 5.1. The studied variant families denoted *0100-0900* includes changing one parameter at the time. For some of those, i.e. *0700*, only one parameter change has been applicable, due to for example lack of valid tire models. The results of the performed studies presented, are compared to the base model *0000* and discussed in section 5.1.

Result sections and specific result figures are linked in the column denoted *Description* in Table 5.1. In the two rightmost columns, the simulation times presented refer to the elapsed time of creating the MNF through Nastran and the elapsed time to run the model in Adams using 12 cores. In case of simulation failure, the simulation time is presented as *Sim. fail.* and not applicable (N/A). For the changes in the ODF tool that do not require re-runs of the model or model creations, the times are set to *BASE*. After changing one parameter at the time, the sensitivity and a final discussion are presented.

Table 5.1: Overview of simulation variants.

Variant	Description	Time [s] (Nastran)	Time [s] (Adams)
0000	**Base** Results: Figures 5.1, 5.2, 5.3 & 5.4, and section 5.1.1.		
	Reference for simulations.	7246	3803
0100	**Frequency** Results: Figures 5.6 & 5.7 and section 5.1.2.		
0101	Include flexible modes with frequencies up to 9% of the reference. As reference, the base model includes one flexible mode.	Sim. fail.	N/A
0102	Include flexible modes with frequencies up to 682% of the reference.	18958	3947
0103	Include flexible modes with frequencies up to 91% of the reference.	7301	3887

Continued on next page

Table 5.1 – continued from previous page

Variant	Description	Time [s] (Nastran)	Time [s] (Adams)
0104	Include flexible modes with frequencies up to 1364% of the reference.	49276	8457
0105	Include flexible modes with frequencies up to 273% of the reference.	8749	4522
0106	Include flexible modes with frequencies up to 454% of the reference.	12863	4964
0200	**Battery stiffness** Results: Figures 5.8 & 5.9 and section 5.1.3		
0201	Battery stiffness decreased to 6% of the reference.	7345	3827
0202	Battery stiffness increased to 163% of the reference.	7463	3709
0300	**ASET DOFs** Results: Figures 5.10 & 5.11 and section 5.1.4		
0301	Translational DOFs only in all ASET nodes, which corresponds to 60% of the reference number of DOFs.	5683	3272
0302	All DOFs in all ASET nodes, which corresponds to 120% of the reference number of DOFs.	8184	4132
0400	**SEP value** Results: Figures 5.12 & 5.13 and section 5.1.5		
0401	Changed SEP value to 5% or 25% of the reference.	BASE	BASE
0402	Changed SEP value to 30% or 150% of the reference.	BASE	BASE
0403	Changed SEP value to 10% or 50% of the reference.	BASE	BASE
0404	Changed SEP value to 100% or 500% of the reference.	BASE	BASE
0500	**Signal time length** Results: Figures 5.14 & 5.15 and section 5.1.6		
0501	No trim, i.e. take entire time signal 0-25 s.	BASE	BASE
0502	Trim 1-16 s or use 75% of the original time length.	BASE	BASE
0503	Trim 1-11 s or use 50% of the original time length.	BASE	BASE
0504	Trim 1-6 s or use 25% of the original time length.	BASE	BASE
0505	Offest. Trim 10-15 s or use another 25% of the original time length.	BASE	BASE

Continued on next page

Table 5.1 – continued from previous page

Variant	Description	Time [s] (Nastran)	Time [s] (Adams)
0600	**Frequency range** Results: Figures 5.16, 5.17, 5.18, 5.19 & 5.20 and section 5.1.7.		
0601	Include 1-75 Hz in the ODF tool, or using 125% of original frequency range.	BASE	BASE
0602	Include 5-75 Hz in the ODF tool, or using 117% of original frequency range.	BASE	BASE
0603	Include 10-75 Hz in the ODF tool, or using 108% of original frequency range.	BASE	BASE
0604	Include 20-75 Hz in the ODF tool, or using 92% of original frequency range.	BASE	BASE
0605	Include 25-75 Hz in the ODF tool, or using 83% of original frequency range.	BASE	BASE
0606	Include 30-75 Hz in the ODF tool, or using 75% of original frequency range.	BASE	BASE
0607	Include 1-20 Hz in the ODF tool, or using 32% of original frequency range.	BASE	BASE
0700	**Tire model** Results: Figures 5.21 and 5.22 and section 5.1.8.		
0701	Changing the tire model to a higher rim diameter.	BASE	3856
0800	**Velocities** Results: Figures 5.23 & 5.24 and section 5.1.9.		
0801	Increase velocity to 50 km/h or 167% of the reference.	BASE	5681
0900	**Damping** Results: Figures 5.25, 5.26, 5.27 & 5.28 and section 5.1.10.		
0910	Adjust modal damping applied to the body MNF.		
0911	Modal damping d_1 in Figure 2.5 of 10% of the reference.	BASE	3785
0912	Modal damping d_1 in Figure 2.5 of 50% of the reference.	BASE	3902
0920	Adjust ramp up range of modal damping applied to the body MNF.		
0921	Original damping up to 83% of the reference (i.e. changing f_1 in Figure 2.5), ramp up linearly to 100 % damping at 100% of the reference.	BASE	Sim. fail.
0922	Original damping up to 83% of the reference, ramp up linearly to 100 % damping at 80% of the reference, i.e. also changing f_2.	BASE	3780

Continued on next page

Table 5.1 – continued from previous page

Variant	Description	Time [s] (Nastran)	Time [s] (Adams)
0923	Original damping up to 94% of the reference, ramp up linearly to 100 % damping at 100% of the reference.	BASE	3692
0924	Original damping up to 100% of the reference, ramp up linearly to 100% damping at 95% of the reference.	BASE	3692

5.1 Parameter investigation

The ODFs originating from the parameter study are presented and briefly discussed in the following sections. First, the base model is described and compared to the test results. Then, each section corresponds to changes of a certain parameter following the structure of Table 5.1. All results of the parameter study are compared to the base model and test data. The diagonals over the vehicle are presented in Figures 2.6-2.8, where the diagonals are presented together with the names used in the ODF. In the legend, the variants have been ordered in ascending order of the studied property.

5.1.1 Base simulation model

The ODF resulting from the base model is presented in Figure 5.1. In Figure 5.2 the ODF of the base model is compared to the ODF from test. It can be observed that the base model show major differences in magnitude compared to the test data for some diagonals. The base model shows considerably larger deformations for the diagonals over the front doors, the b-diagonals of the rear doors, and for the A-pillar section diagonals. In comparison, diagonals such as the sunroof, engine and the B-pillar section have a closer magnitude to the test data. Noteworthy tendencies of the difference between the test and base are that some diagonals have higher magnitude than the test, while some magnitudes are lower than the test and some diagonals are similar in magnitude.

As described in the methodology, i.e. section 4.2, the simulation model uses a tire model corresponding to different tires than the test vehicle. The larger dimension of the simulated tires implies a stiffer response, which results in an expectation of higher magnitudes. In Figure 5.2, the ODF of the base model is compared to the measurement from day 1, see section 5.2, with the lower speed from Figure 5.30. Considering the tiny differences between the ODF measurements at lower speed from Figure 5.30, and comparing the differences in magnitude between the test and the base simulation *0000* in Figure 5.2, there are differences observed in the fingerprint.

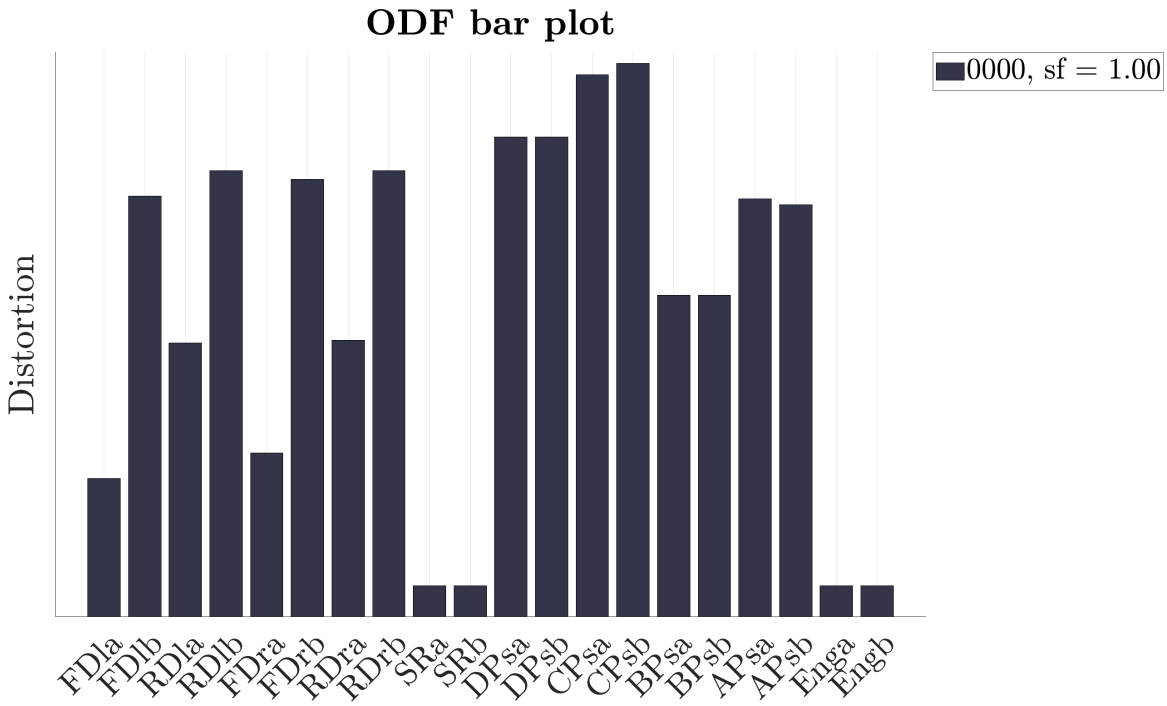

Figure 5.1: ODF of base model (*0000*).

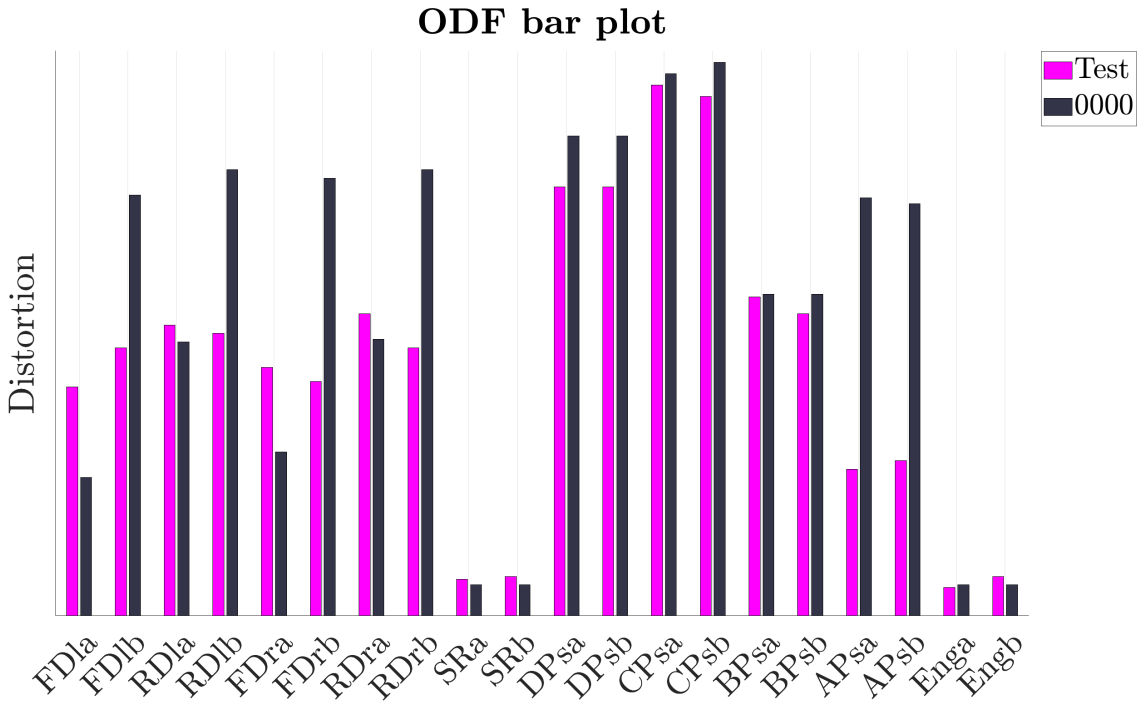

Figure 5.2: ODF of base model (*0000*) together with test data (*Test*).

Similarly as for the ODF in Figure 5.30, the simulation data in Figure 5.2 can be scaled in order to assess how well the fingerprint correlate, see Figure 5.4. From the scaled figure it follows that there are major differences in fingerprint between simulation and test. In Figure 5.3, the fingerprints of the base model and test

data are visualized as lines between the bars over each opening. There are clear differences between the fingerprints considering both magnitude, and angles. The diagonals constituting major differences in fingerprint are highlighted in Figure 5.5.

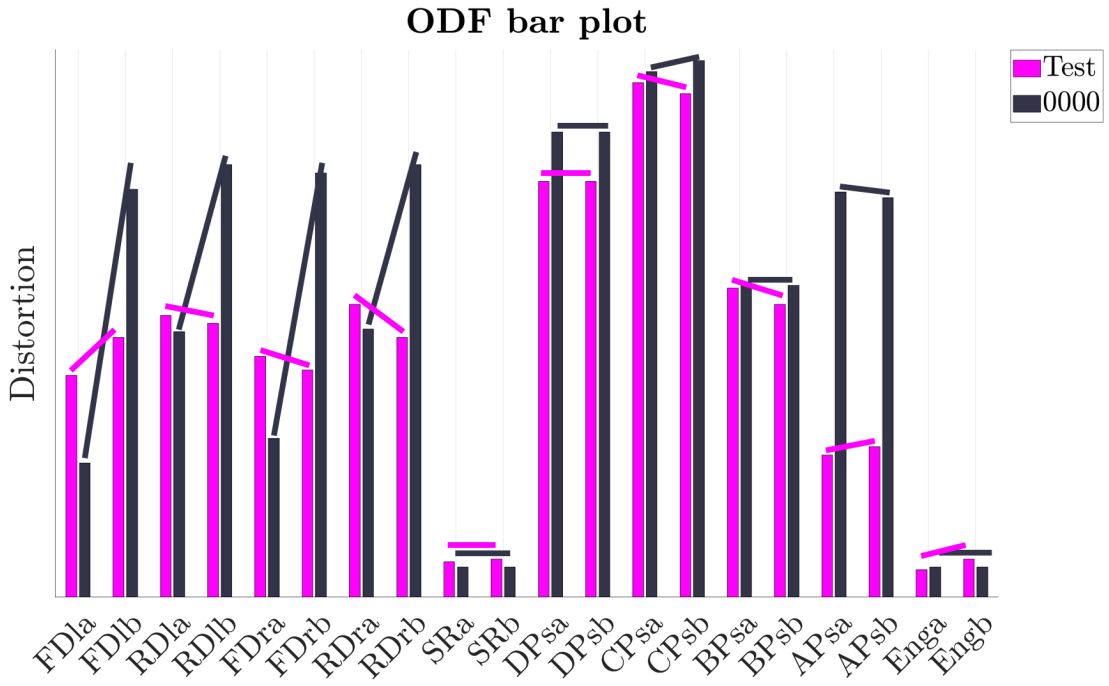

(a)

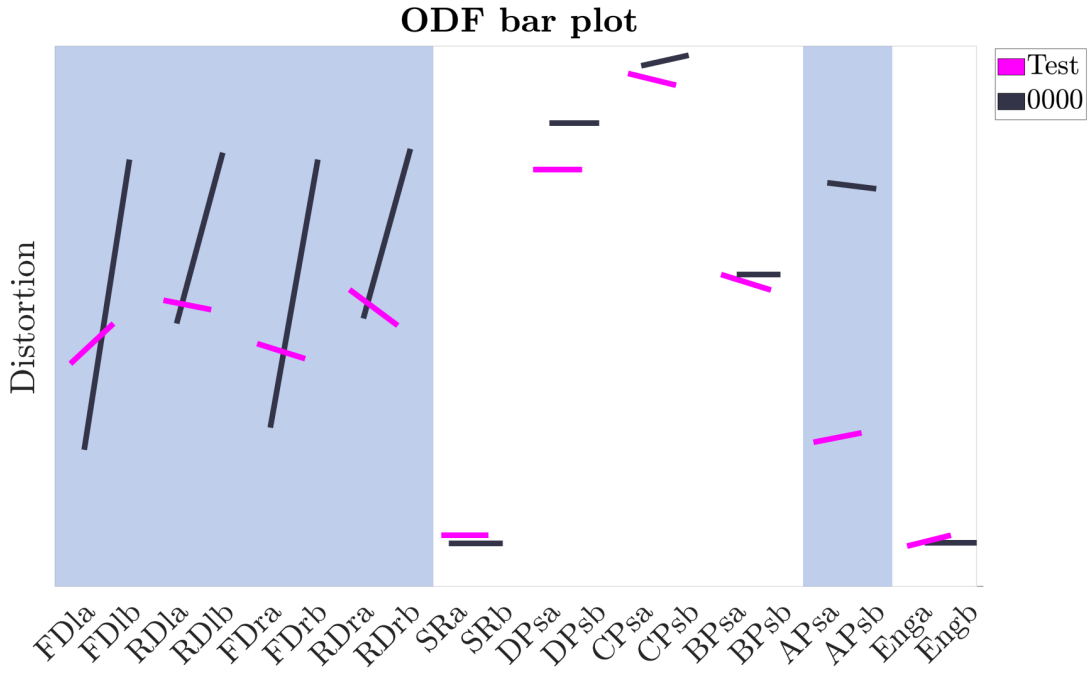

(b)

Figure 5.3: ODF with drawn fingerprint, (a) ODF with the bars, and (b) without the bars. In (b), the deviating diagonals are highlighted in blue.

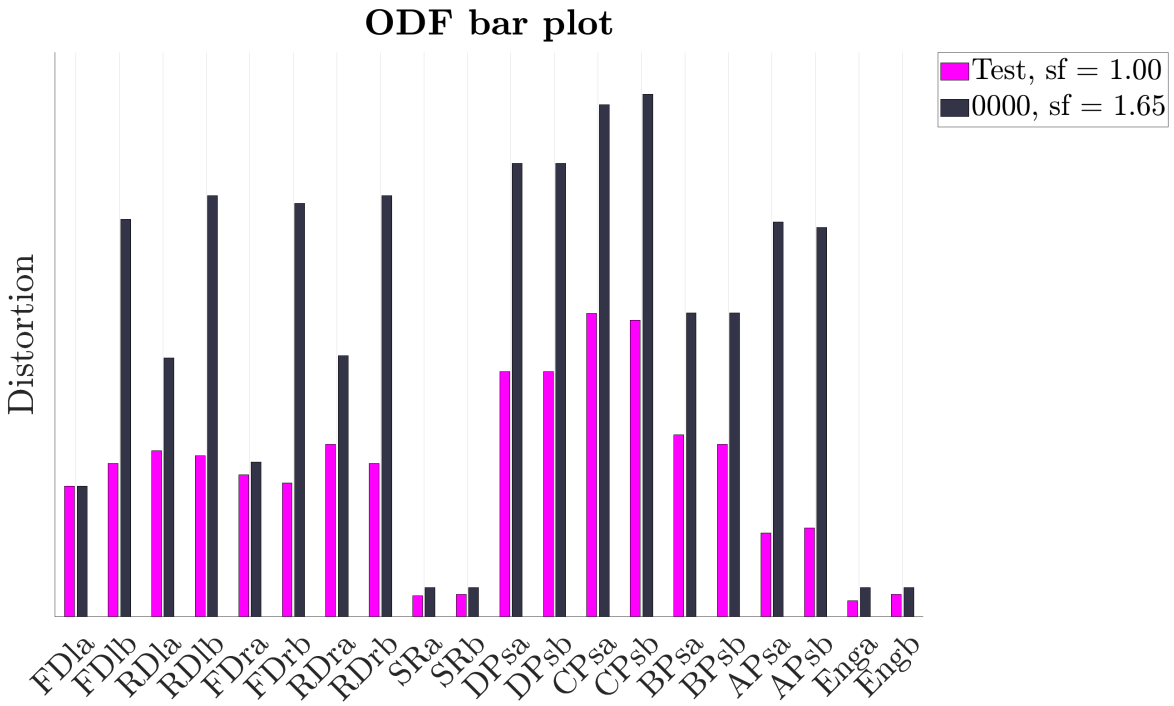

Figure 5.4: ODF of base model (*0000*) together with test data (*Test*). The values are scaled to match the magnitude of FDla.

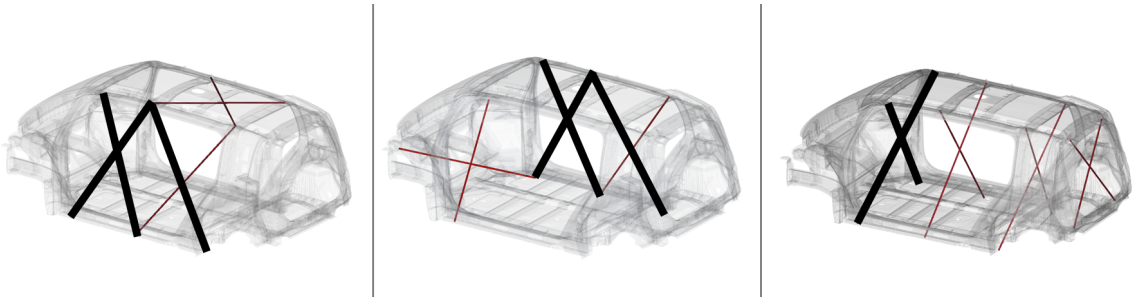

Figure 5.5: MSS diagonals with considerably deviating diagonals from the ODF in Figure 5.3 emphasized in black.

5.1.2 Frequency interval of the modal neutral file

The ODF resulting from the frequency variations *0100* in Table 5.1 are presented in Figure 5.6. In variant *0101*, modes up to 9% of the reference have been taken into account for in the MNF generation. No MNF was received, and the bars are non-existing in the figure since they result in not-a-number (NaN). From the Craig-Bampton reduction example, it is seen that the frequency of the fixed interface modes equal the ones of the lowest structural modes. Since there is no flexible mode below the set frequency, the NaN results suggests that at least one flexible modes included in the reduction.

From Figure 5.6 it follows that the maximum frequency specified in the MNF creation file has an impact on most diagonals and thereby on the resulting ODF. It is

seen that the diagonals over the doors and the cross-sections vary with the different maximum frequencies. Furthermore, it is noticed that the magnitudes of these diagonals are close to the magnitude of the base model, which means that they differ from the test expectations.

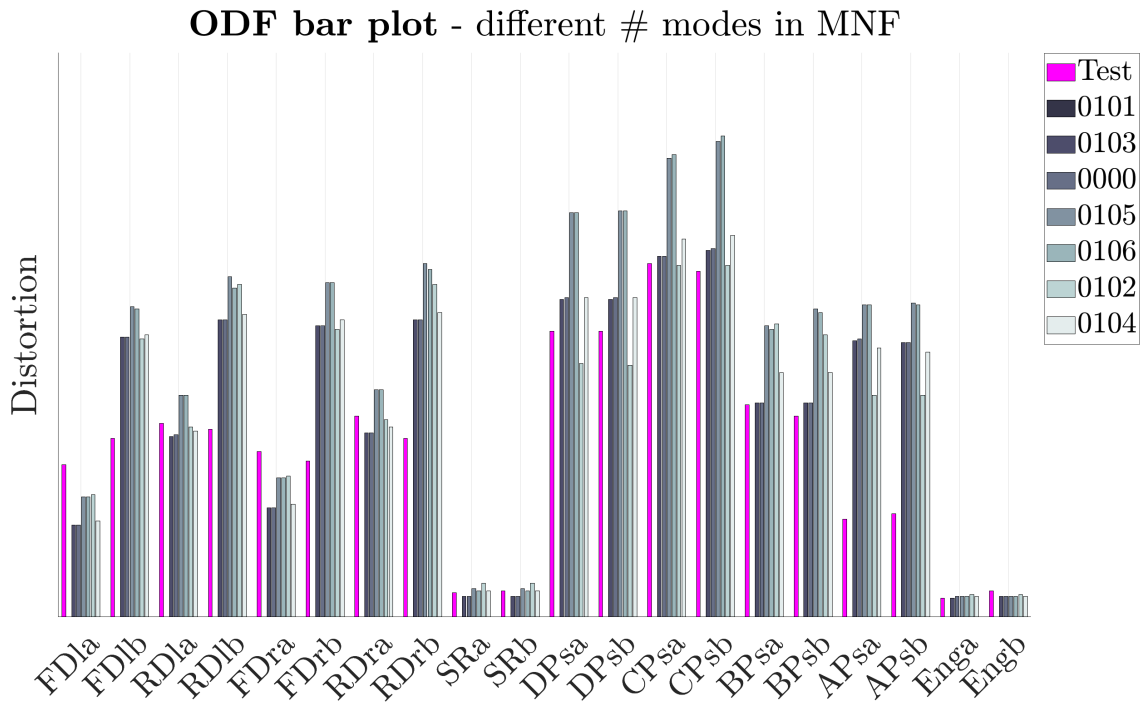

Figure 5.6: ODF of base model, test data and MNFs generated with different frequency intervals for the flexible modes. The frequency intervals are defined in Table 5.1.

Interesting in Figure 5.6 is that there is no obvious pattern for how the fingerprint changes when the maximum frequency is increased. For the b-diagonals on the doors, the distortion increases up to base or variant *0105*. The variant *0106* show no clear tendency to be of higher or lower distortion than *0105*. For example, the diagonals FDlb and RDla have a similar magnitude as variant *0105*, while the diagonals RDrb and BPsb have slightly lower magnitudes. When including higher flexible modes in the MNF (variants *0102* and *0104*), the distortion is of equal magnitude as the variants *0101* and *0103*, which only include one flexible mode. Over the cross-sections, the behavior of variant *0102* does not follow the pattern of increased distortion with increased maximum frequency in the MNF. The underlying cause of this requires further investigation. The same behavior of lower distortion is also observed for variant *0104*, which has a maximum frequency twice as high as for variant *0102*.

Scaled ODF bars are presented in Figure 5.7, where the fingerprint may be easier to detect. In the figure, it is observed that the fingerprint changes with the different variants. All variants still behaves similar to the base model regarding the high distortion on the b-diagonals of the doors. Besides, all variants have an insignificant impact on the diagonals on the sunroof and over the front of the vehicle. In general,

the results from the base model and the variant *0103* are very similar, which is expected since the difference in mode frequency included in the models is very small. In fact, one flexible mode is included in both cases, which implies that equal results are expected.

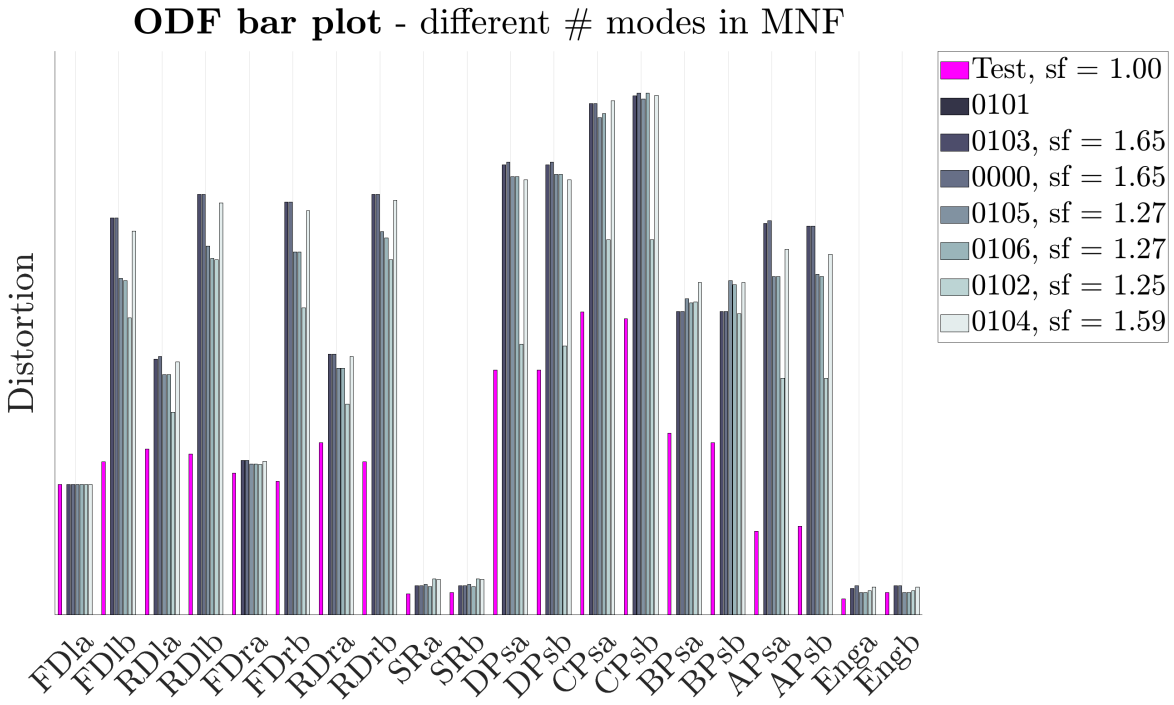

Figure 5.7: ODF of base model, test data and MNF files generated with different frequency intervals for the flexible modes. The values are scaled to match the magnitude of FDla. The frequency intervals are defined in Table 5.1.

5.1.3 Battery stiffness

The ODF impact of the battery, which is located at the bottom of the vehicle model, is presented in Figure 5.8, where the variants represents different battery stiffnesses. The figure illustrates that the distortion magnitudes are affected by the battery stiffness. The variant *0201* represents the softer battery stiffness compared to the base model and the resulting magnitude is larger or similar to the base for all diagonals. The variant *0202*, represents the stiffer battery, and shows similarities in magnitude to the base model. Consequently, using a stiffer battery than the base model has an insignificant affect on the fingerprint, and the battery is hence considered to be modeled stiff enough.

The results of changing the battery stiffness presented in Figure 5.8, show no clear convergence towards the test data in terms of the total fingerprint. The diagonals that had a magnitude closer to the test data remain close to the test data, and the diagonals far from the test data remain distant to the test data. The effect of the battery stiffness may be easier to detect by scaling the ODF bars such that all bars have the same magnitude over FDla, as visualized in Figure 5.9. In the figure it can be seen that the fingerprint differs between the studied battery stiffnesses, but there is no overall conclusion to be made.

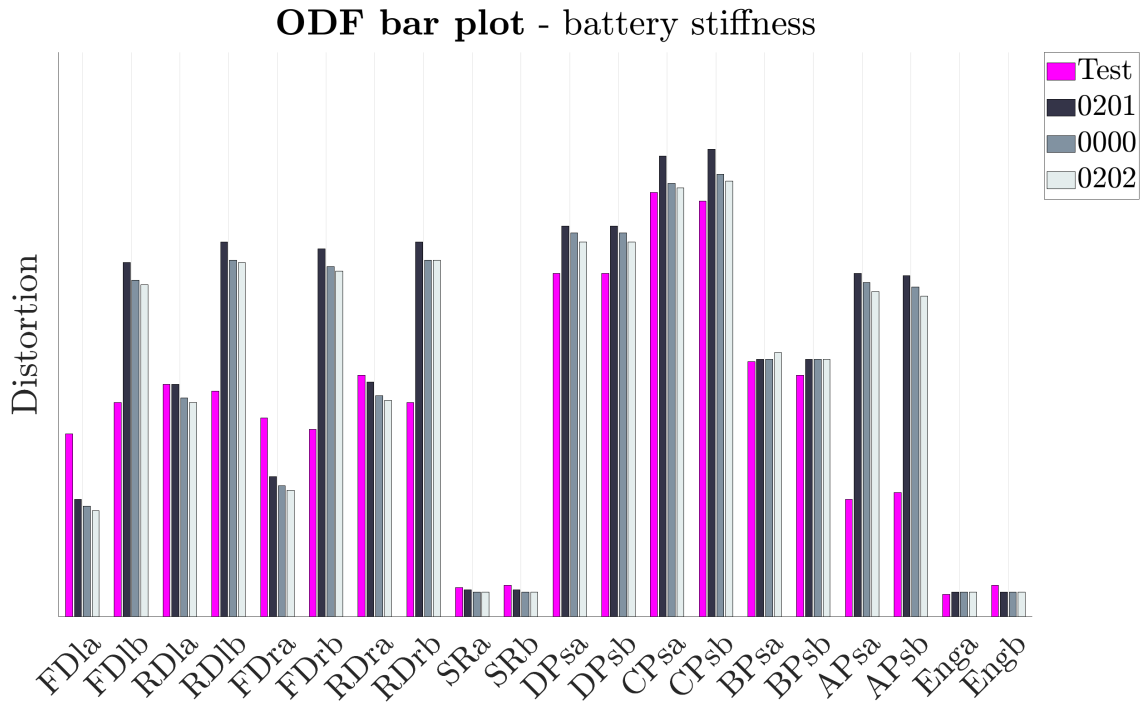

Figure 5.8: ODF of battery stiffness changes (*0201,0202*) together with base model (*0000*) and test data (*Test*). The battery stiffnesses are presented in Table 5.1.

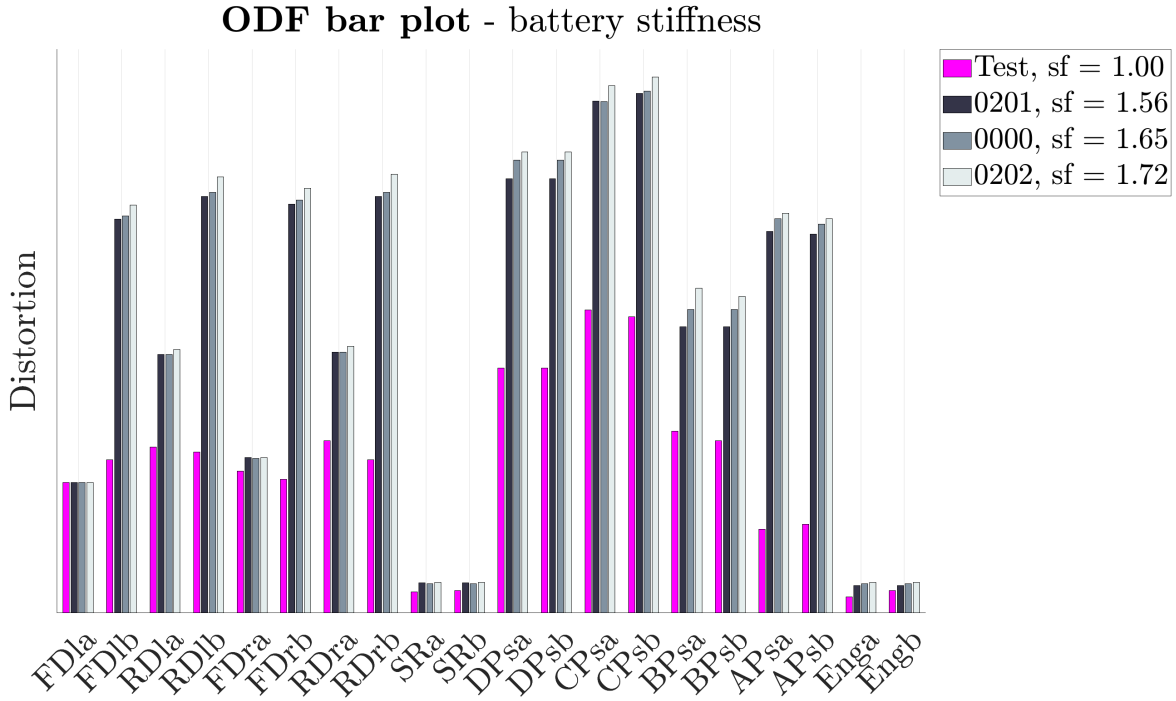

Figure 5.9: ODF of battery stiffness changes (*0201,0202*) together with base model (*0000*) and test data (*Test*). The values are scaled to match the magnitude of FDla. The battery stiffnesses are presented in Table 5.1.

5.1.4 ASET degrees of freedom

For the model of the robot-taxi, the ASET is pre-defined and is considered fixed for the thesis work. For this section, phrases like *including all DOFs* refer to including all DOFs of the pre-defined ASET nodes. The pre-defined ASET nodes constitute a couple of parts per million (ppm) of the total number of nodes in the FE model.

Including all translational DOFs in the ASET as for variant *0301*, and including all translational and rotational DOFs in the ASET as for variant *0302*, shows a minor impact on the result, see Figure 5.10. It can be noted that including all DOFs of the ASET in the MNF, gives higher distortion values than the base model. Only including the translational DOFs in the ASET shows similar, or slightly lower distortion values than the base model. The differences in distortion may differ for another ASET, as observed in the beam examples, see section 3.2.1. However, changing the ASET nodes is considered to be out of the scope of the thesis.

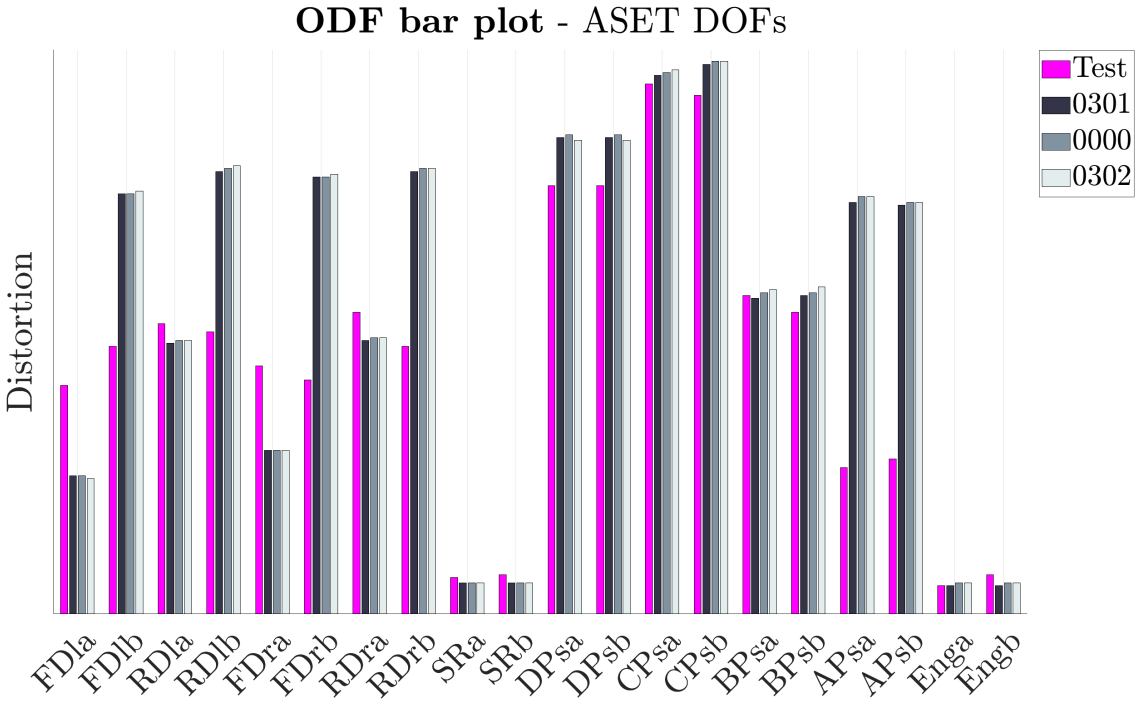

Figure 5.10: ODF of ASET DOFs adjustments (*0301,0302*) together with base model (*0000*) and test data (*Test*). The ASET adjustments are defined in Table 5.1.

In order to simplify the interpretation of how well the fingerprints correlate, scaled ODF bars are presented in Figure 5.11. From the figure it follows that when the number of ASET DOFs are increased, the distortion is also increased. In particular, the difference between including all translational DOFs and the base model are small, in comparison to including all DOFs.

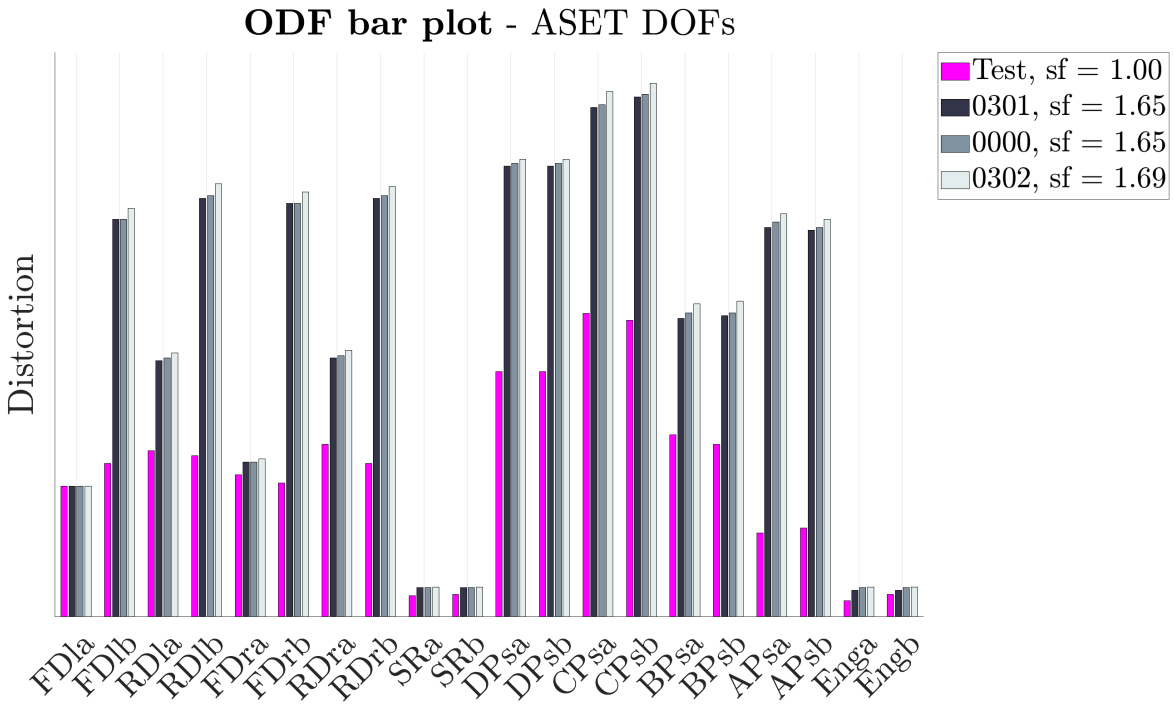

Figure 5.11: ODF of ASET DOFs adjustments (*0301,0302*) together with base model (*0000*) and test data (*Test*). The values are scaled to match the magnitude of FDla. The ASET adjustments are defined in Table 5.1.

From the Guyan reduction example (section 3.2.2) it is seen that including all translational DOFs in all nodes gave a solution very close to the full solution. Furthermore, it is observed that the reduced solution approaches the full solution as the number of DOFs is increased, which suggests that including more DOFs in the ASET would result in an ODF closer to the test data, which suggests that variant *0302* should be considerably closer to the test data than variant *0301*. From Figure 5.10, it follows that including exclusively all translational DOFs or all DOFs of the ASET, show that the resulting ODFs are insignificantly closer to the ODF of the test, compared to the ODF of the base model. However, including all DOFs of the pre-defined ASET means including some ppm of the total number of DOFs in the FE model. Combined with the fact that the translational DOFs have proven to have a larger impact on the frequencies after a CMS, see section 3.2, the similarities in fingerprint can be explained.

5.1.5 Value of the statistical evaluation parameter

In Meta's ODF tool, the SEP (recall section 2.6.2) value is user defined. Decreasing and increasing the SEP value in comparison to the base is presented in Figure 5.12. From the figure it follows that the magnitudes of the bars differ when the SEP value is changed. When the SEP value is lower than base (*0401, 0403*) the distortion is higher. Increasing the SEP as done for variants *0402* and *0404*, the distortions are lower than for the base model.

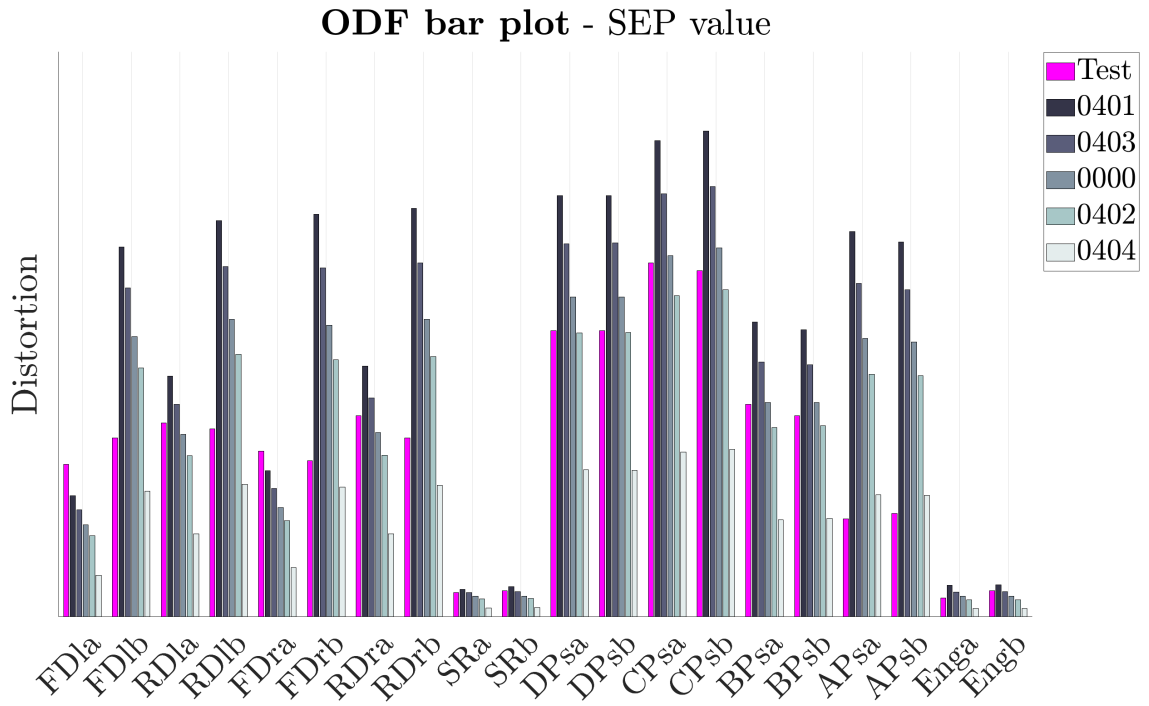

Figure 5.12: ODF when changing SEP values (*0401,0402, 0403, 0404*) together with base model (*0000*) and test data (*Test*). The SEP adjustments are defined in Table 5.1.

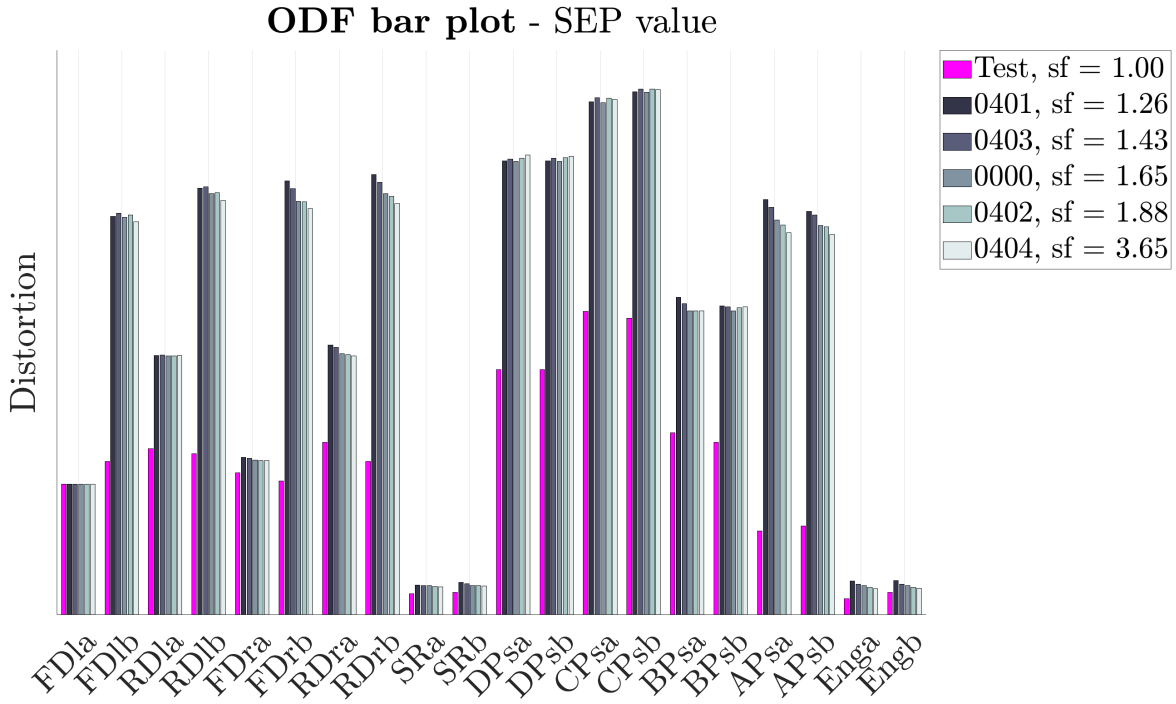

Figure 5.13: ODF when changing SEP values (*0401,0402, 0403, 0404*) together with base model (*0000*) and test data (*Test*). The values are scaled to match the magnitude of FDla. The ASET adjustments are defined in Table 5.1.

For easier interpretation on how the fingerprint is affected, scaled bars are presented in Figure 5.13. As for the previously scaled ODFs, the bars are scaled to match the test data for the diagonal FDla. In the figure it is seen that the SEP value has a minor affect on the fingerprint. It is observed that the b-diagonals of the doors show a greater difference in magnitude between the different SEP values than for the a-diagonals. Additionally, the A-pillar section bars, for example, indicate that the SEP differ from a pure scaling of the data since the magnitude decreases when the SEP is increased for the scaled bar plot. Considering that the SEP values have a small affect on the fingerprint, the SEP here act mainly as a scaling on the data, which indicates that the SEP value of the base model is selected accurately. This is expected according to [38].

5.1.6 Post-processing signal time length

The ODF for different signal time lengths of the base model, are presented in Figure 5.14. From the figure it follows that the ODF is affected by the considered signal time length. In order to assess whether the differences represent a scaling of the ODF or an actual difference in the fingerprint, the bars have been scaled such that the FDla diagonal of each variant has the same magnitude as the test data. The results are presented in Figure 5.15.

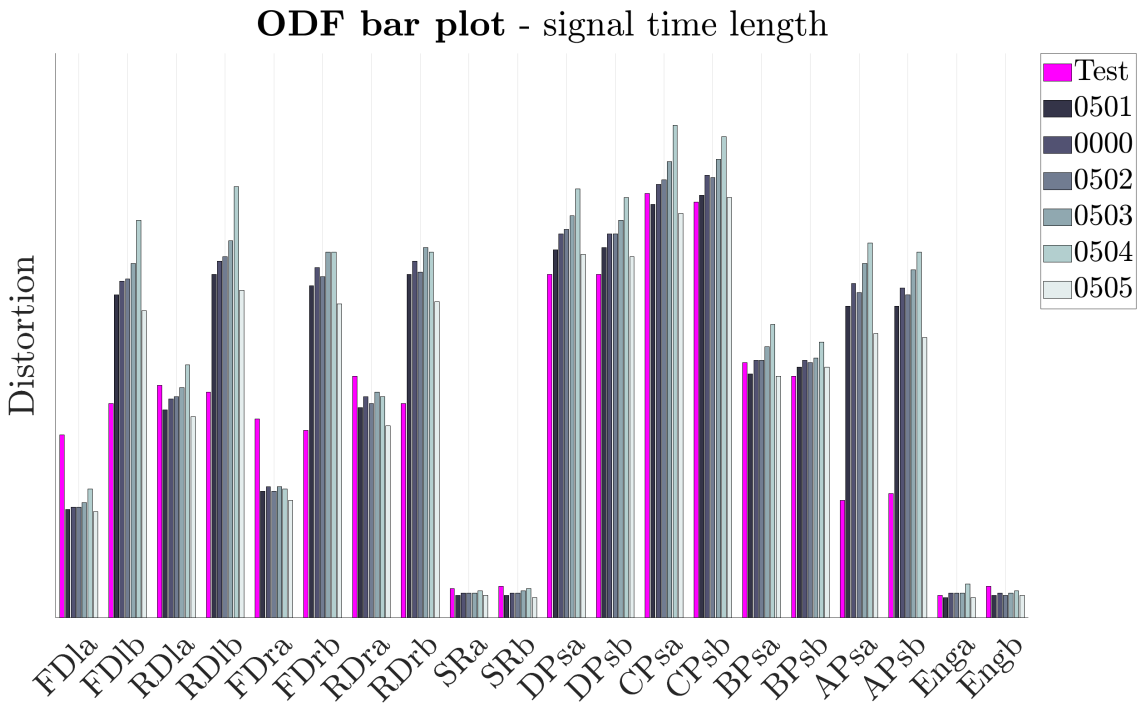

Figure 5.14: ODF of different time length intervals (*0501, 0502, 0503, 0504, 0505*) together with base model (*0000*) and test data (*Test*). The ASET adjustments are defined in Table 5.1.

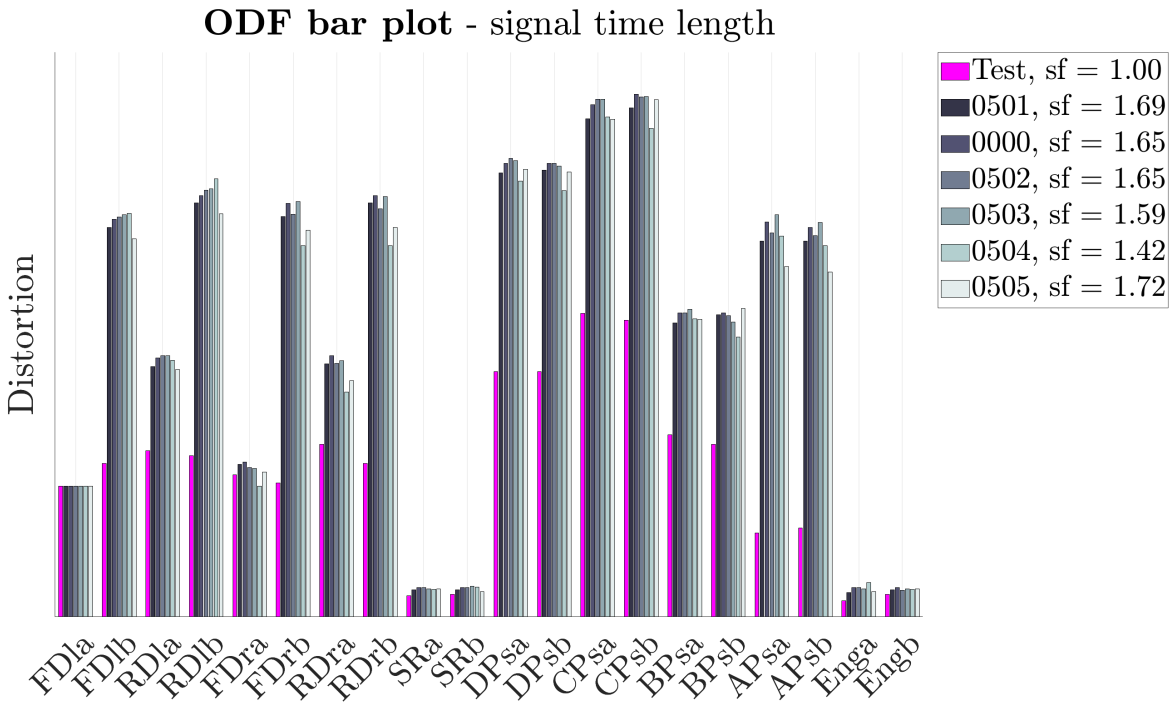

Figure 5.15: ODF of different time length intervals (*0501, 0502, 0503, 0504, 0505*) together with base model (*0000*) and test data (*Test*). The values are scaled to match the magnitude of FDla. The ASET adjustments are defined in Table 5.1.

From Figure 5.15 it follows that the signal time length has an impact on the fingerprint. In particular, for the diagonals RDra and RDrb, the test data has a bar that is greater for the a-diagonal than the b-diagonal while the variant *0504* gives the opposite relationship. Another interesting observation, of the bars corresponding to the C-pillar section diagonals is that the variant *0504* show the same pattern with slightly lower values for the b-diagonal than for the a-diagonal as the test data. The diagonals over the the sun roof, cross-sections and front represent a similar fingerprint as the test data and base model. However, the previously observed large magnitudes of the b-diagonals in the front and rear doors, are prominent also when changing the signal time length.

The fact that the fingerprint is very similar between the base model and the variant *0502* indicates that that the time length of variant *0502* might be enough. In contrast, the fact that the base model deviates from including the full time history (as done in variant *0501*) indicates that the time length of the base model hight be too short. Considering the fact that the entire time signal could include deviations at the ends, could however be used in arguing that the signal time length of the base model could be too short. In order to assess whether the time signal is of accurate length in the base model or not, a longer simulation could be run.

5.1.7 Post-processing frequency range

By changing the frequency range to be considered in the ODF tool, the fingerprint and magnitudes change, see Figure 5.16. In the figure, variants *0601* and *0607* includes frequencies from 1 Hz up to 75 Hz and 20 Hz, respectively. Since they show a similar magnitude, no significant behavior seem to be missed when neglecting the frequency response over 20 Hz. However, the high magnitudes could be a result of the RBMs, which are out of interest in this case, see section 2.6.1. Another interesting observation, considering variants *0601* and *0607*, is that the frequencies between 20 and 75 Hz seem to have a minor impact on the fingerprint. The minor impact on the fingerprint could be a result of too few modes being included in the base MNF, but further investigation is needed in order to understand why these variants are similar.

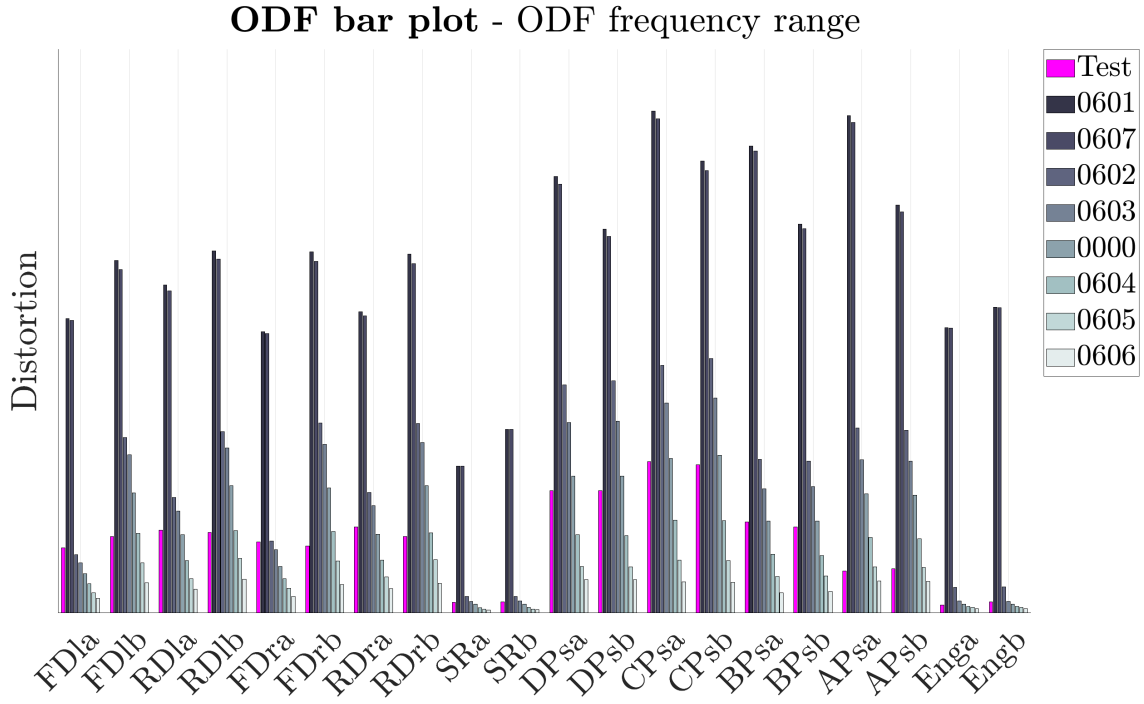

Figure 5.16: ODF of different frequency ranges included in the ODF tool (*0601-0606*) together with base model (*0000*) and test data (*Test*). The frequency ranges included are defined in Table 5.1.

For the variants *0603-0606*, the frequency range is decreased by 5 Hz by increasing the lower frequency limit for each iteration. In Figure 5.16, it is observed that the magnitude decreases. Some reasons for the decreasing magnitude could be that information is lost when the lower cut-off frequency is increased. Scaling of all variants such that they have the same magnitude for the FDla diagonal, is presented in Figure 5.17. From the figure it follows that the fingerprint is affected substantially.

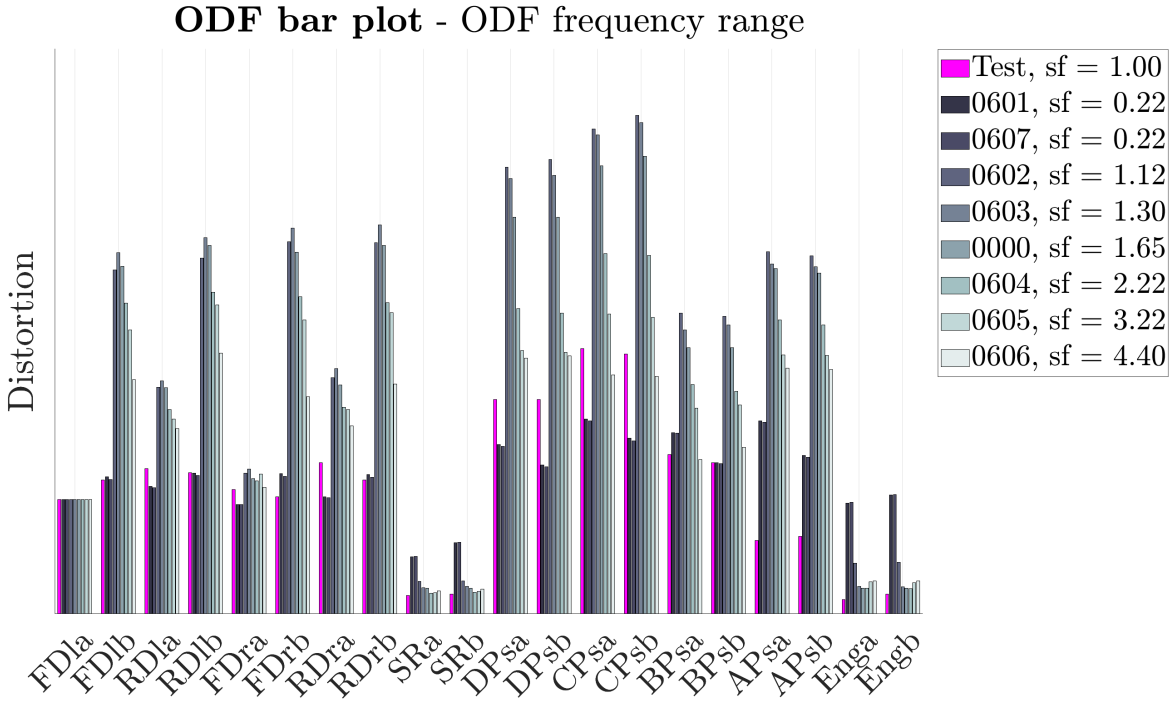

Figure 5.17: ODF of different frequency ranges included in the ODF tool (*0601-0606*) together with base model (*0000*) and test data (*Test*). The values are scaled to match the magnitude of FDla. The frequency ranges are defined in Table 5.1.

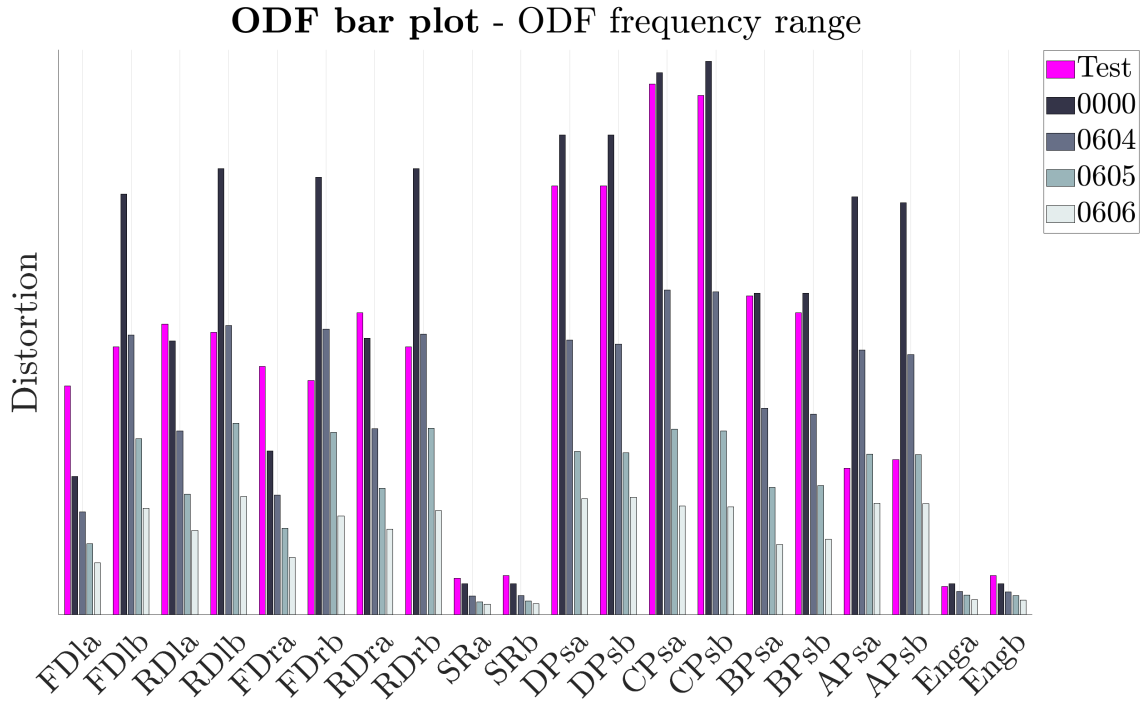

Figure 5.18: ODF of different frequency ranges included in the ODF tool (*0601-0606*) together with base model (*0000*) and test data (*Test*). The frequency ranges included are defined in Table 5.1.

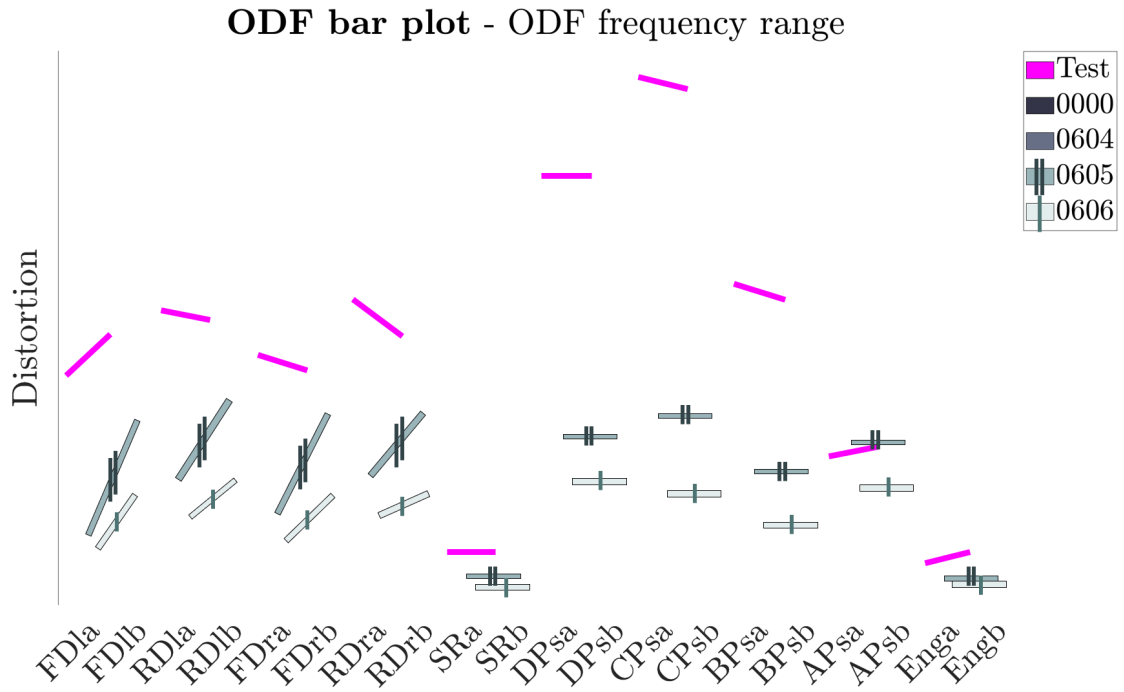

Figure 5.19: Drawn fingerprint of variants *0605* and *0606* from Table 5.1.

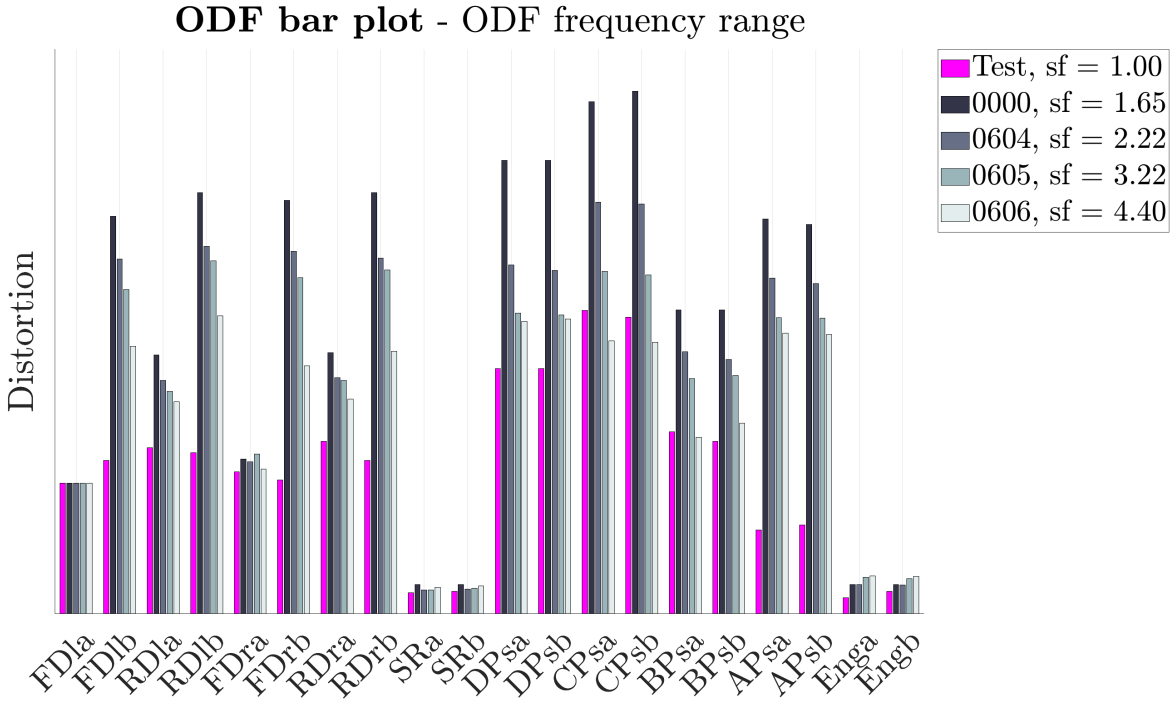

Figure 5.20: ODF of different frequency ranges included in the ODF tool (*0601-0606*) together with base model (*0000*) and test data (*Test*). The values are scaled to match the magnitude of FDla. The frequency ranges included are defined in Table 5.1.

In order to study the bars with lower magnitudes in Figure 5.16, the bars that that include low frequencies imposing large magnitudes (i.e. variants *0601*, *0607*,

0602 and *0603*), are removed in Figure 5.18. In the figure, it is seen that the magnitude decreases as the lower frequency in the frequency range is increased. More interestingly, studying variants *0605* and *0606* in Figure 5.18, it seems like the lower cut-off frequency applied in the ODF tool has an impact on the relation between the height of the a- and b-diagonals of the doors. The fingerprints of the test data and variants *0605* and *0606* are drawn in Figure 5.19. The fact that the slope of the door diagonals are significantly impacted by the lower cut-off frequency suggests that the simulation creates some kind of artificial mode between the lower cut-off frequencies of variants *0605* and *0606*. Therefore, studying the mode shapes in this interval would be of interest as a topic of future research.

When scaling the bars, as done in Figure 5.20, the fingerprint is seen to differ between the variants. However, the magnitude of the fingerprint of the different variants are still far away from the fingerprint of the test data.

5.1.8 Tire model

Changing the tires in the MBD model to tires with similar outer diameter and width compared to base in order to study whether the tire model has an impact on the correlation, shows differences in measured distortion magnitude compared to the base model, see Figure 5.21.

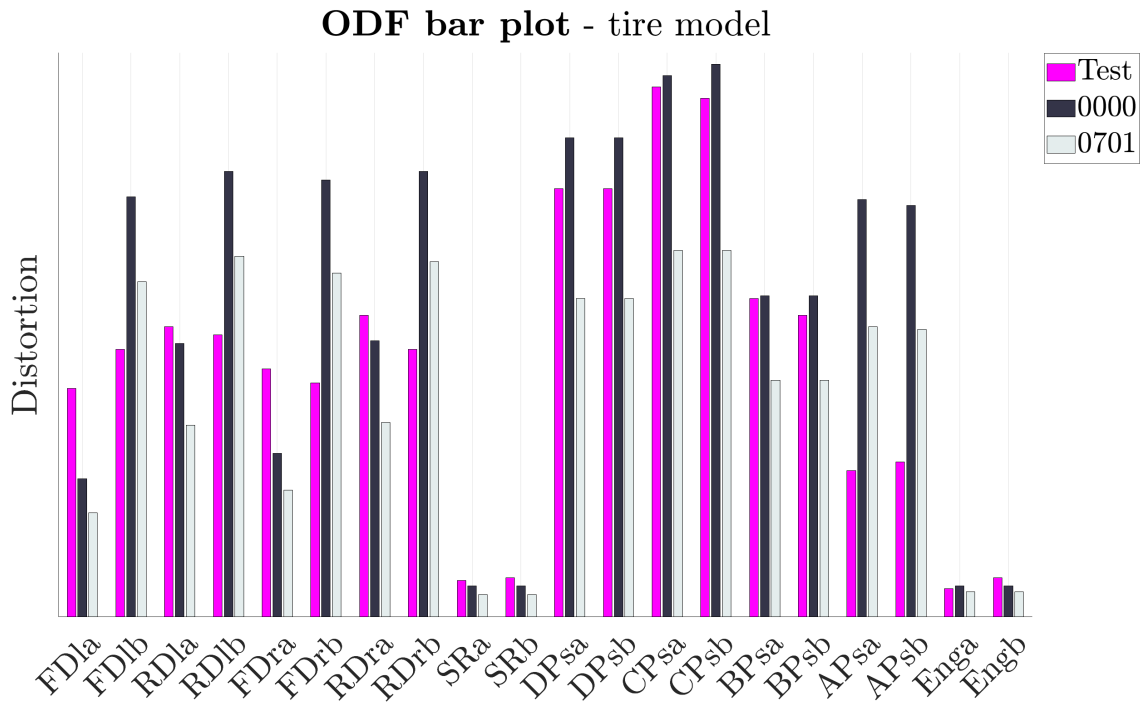

Figure 5.21: ODF of changed tires together (*0701*) with the base model (*0000*)and the test data (*Test*). The tire changes are specified in Table 5.1.

From Figure 5.21 it follows that the difference of tire model has an impact on the resulting magnitude of the ODF. It can be noted that all diagonals obtain a lower magnitude than the base model. In addition, some diagonals such as the *D*-, *C*- and *B*-pillar section diagonals receive a lower magnitude than the base model. From the figure it follows that the fingerprint appear to be similar between the base model *0000*, and the changed tire model *0700*, but with some differences in magnitude. Scaling the bars as presented in Figure 5.22, differences in the fingerprint are observed for the different tires, but the slope of the defining the fingerprint correspond to the base. In total, the variant *0701* show a similar fit of the fingerprint to the test data as the base model.

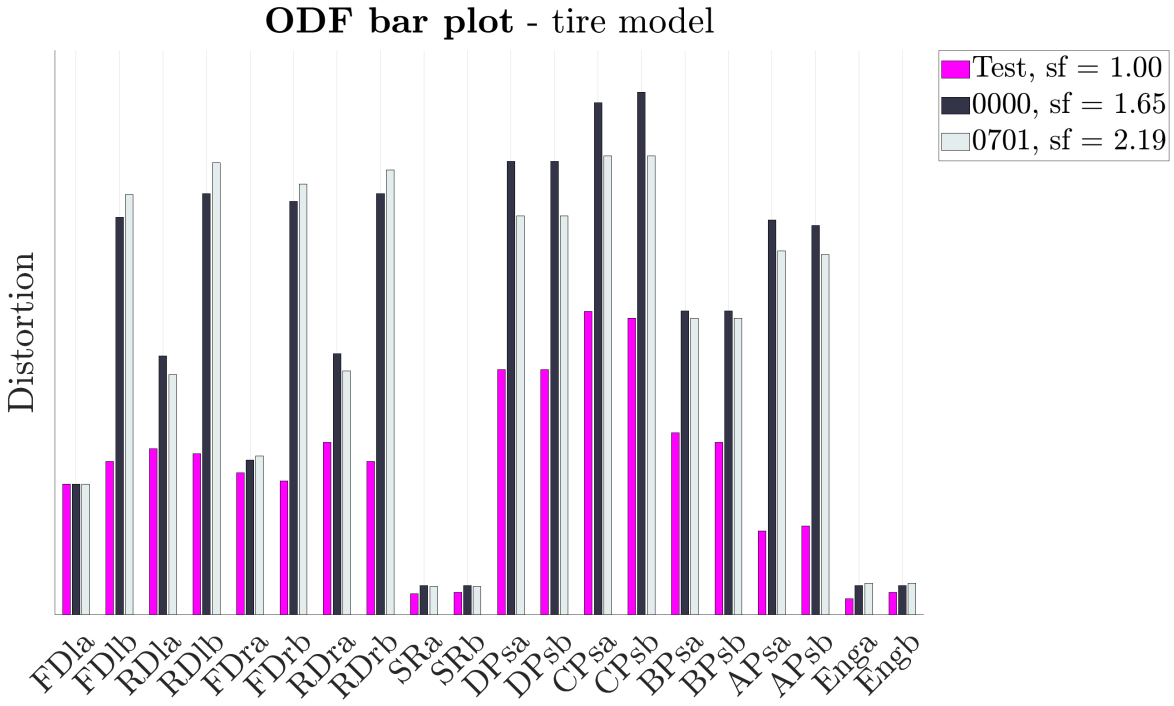

Figure 5.22: ODF of changed tires together (*0701*) with the base model (*0000*)and the test data (*Test*). The values are scaled to match the magnitude of FDla. The tire changes are specified in Table 5.1.

The fact that the tire model can be considered to have a minor impact on the fingerprint can justify the choice of modeling the base model with a different dimension compared to the tires of the test vehicle. The justification would be based on the fact that the actual fingerprint is minorly affected by the tire model. Besides, a tire model based on measurements is considered being more representative than a purely simulated model. However, it could be of interest to study measured tires with dimension and properties of the physical vehicle since the ODF of the base model and test data differ. Additionally, as observed, the tire model can affect the ODF magnitude. Furthermore, a limited amount of tire models have been tested, which further emphasizes the need for further investigation of the tire model.

5.1.9 Simulating different velocities

Driving faster in the MBD simulation, 50 km/h instead of 30 km/h as for the base, shows larger distortion magnitudes for all diagonals presented in Figure 5.23. The larger distortion should be a result of wheel hop being more dominant at higher velocity.

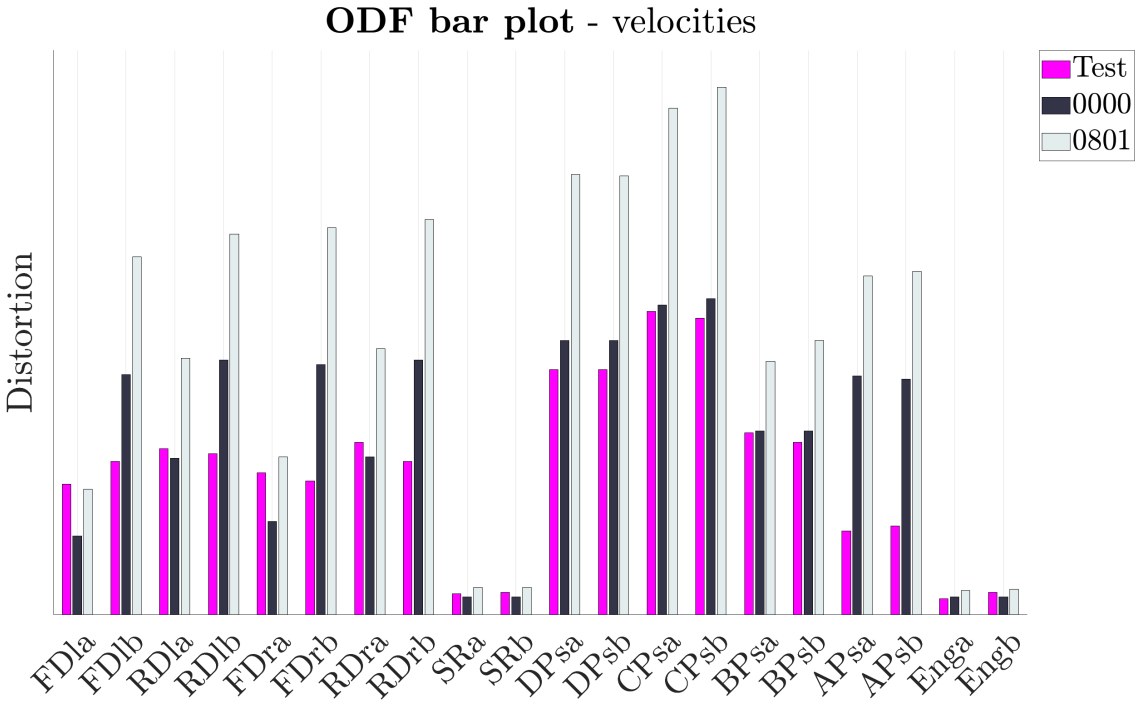

Figure 5.23: ODF results from driving faster (*0801*) together with the base model (*0000*) and test data (*Test*). The velocity is stated in Table 5.1.

With the different velocities, the fingerprint shows differences in magnitude only, which can be seen in Figure 5.24 in which the variants have been scaled such that the magnitude of the diagonal FDla is equal. In Figure 5.24, the fingerprint is very similar for the different variants, which shows that the velocity only result in a scaling of the distortion. The lack of change in fingerprint indicates robustness in the ODF on the same vehicle structure, since nothing on the vehicle has changed from the base model.

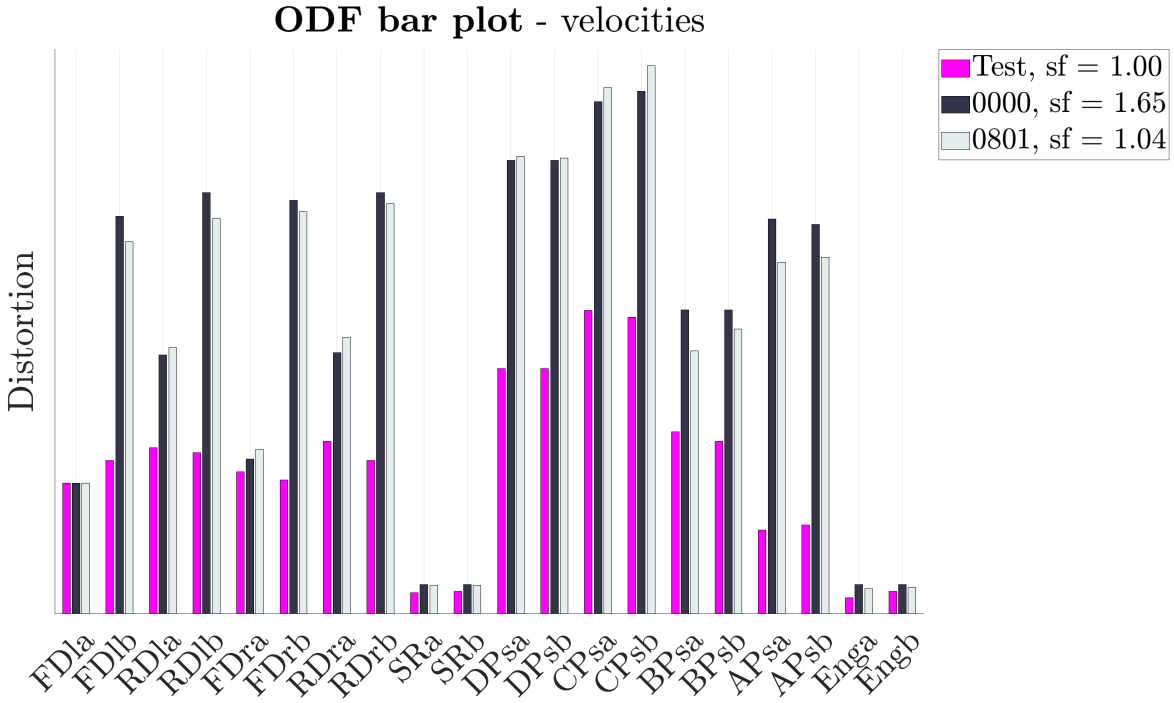

Figure 5.24: ODF results from driving faster (*0801*) together with the base model (*0000*) and test data (*Test*). The values are scaled to match the magnitude of FDla. The velocity is stated in Table 5.1.

5.1.10 Modal damping of the fully trimmed body

As presented in Table 5.1, the damping has been varied in two different ways. The first studied variants include changing the constant damping d_1 in the damping model presented in Figure 2.5. The results from changing d_1 are presented in Figure 5.25 and section 5.1.10.1. Similarly, the results from changing the ramp-up interval, i.e. changing f_1 and f_2, are presented in Figure 5.27 and section 5.1.10.2.

5.1.10.1 Changing modal damping

From Figure 5.25 it follows that the damping has an impact on the resulting ODF. The overall behavior is that increased damping results in decreased distortion, which makes sense considering that increased damping should result in reduced movement of the vehicle. Scaling of the bars in the ODF are presented in Figure 5.26. In the figure, it is seen that the fingerprint stays similar to the base model for both variants.

However, considering the fingerprint observed in Figure 5.26, it seems like the original damping of the base model is too small for a majority of the diagonals (FDlb, RDlb, FDrb, RDrb, DPsa, DPsb, CPsa, CPsb, BPsb, APsa, APsb) since the bars are higher for simulation than the test data. The fact that the damping may be too small is interesting since the original damping of the base model is considered to be a very large damping, on the border of being non-physical (Weber, J., and Ugale, P., personal communication, April 3, 2025). Another interesting observation

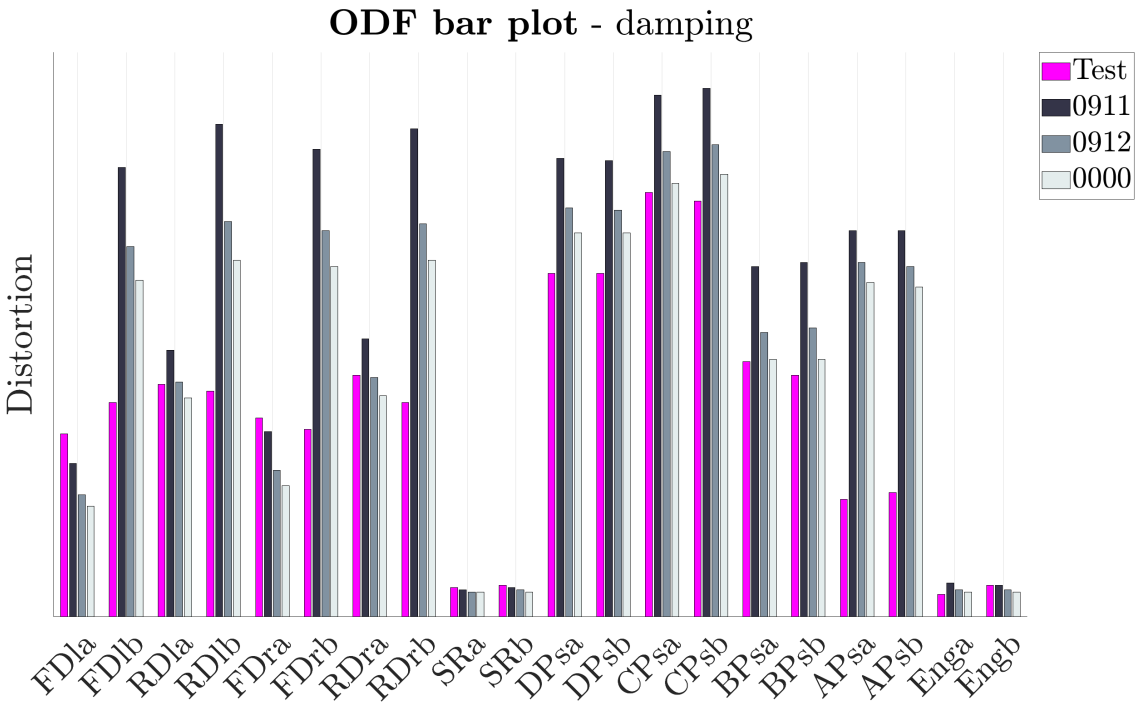

Figure 5.25: ODF results from adjusted damping parameter d_1, i.e. adjusting the constant damping up to 90 Hz. Damping reduced to half the original damping (*0912*) and to a tenth of the original damping (*0911*) along with the base (*0000*) and test data (*Test*). Further description of variants are included in Table 5.1.

is that the trend of too small damping only exist for the b-diagonals of the front and rear doors. Since the b-diagonals are also further from the test results, this could indicate some kind of modeling issue. Furthermore, it is noticed that the diagonals over the cross-sections of the car show a tendency to require non-physically large damping, if the damping is assumed to be the only parameter to change to obtain results similar to the test results.

Apart for some diagonals appearing to approach the test data by defining non-physically large damping, some diagonals match the test data very well for the more physical damping of half of the damping of the base modelfor variant *0912*. Examples of such diagonals are the a-diagonals of the rear doors and over the front of the vehicle. The fact that some diagonals behave as expected for a physical damping suggests that the model could be tuned to behave accurately for physical values of the damping. Furthermore, some of the remaining diagonals (FDla, FDra, SRa, SRb, ENGb) approaches the test data for the low modal damping. Since there is always some damping in a mechanical system, a too low modal damping could be seen as non-physically low instead. However, all studied values of the modal damping can be seen as physical.

In total, from Figure 5.25 it follows that different diagonals, and thereby different parts of the vehicle, may require different damping (or other material and modeling parameters) in order to behave in accordance with the observed behavior from test.

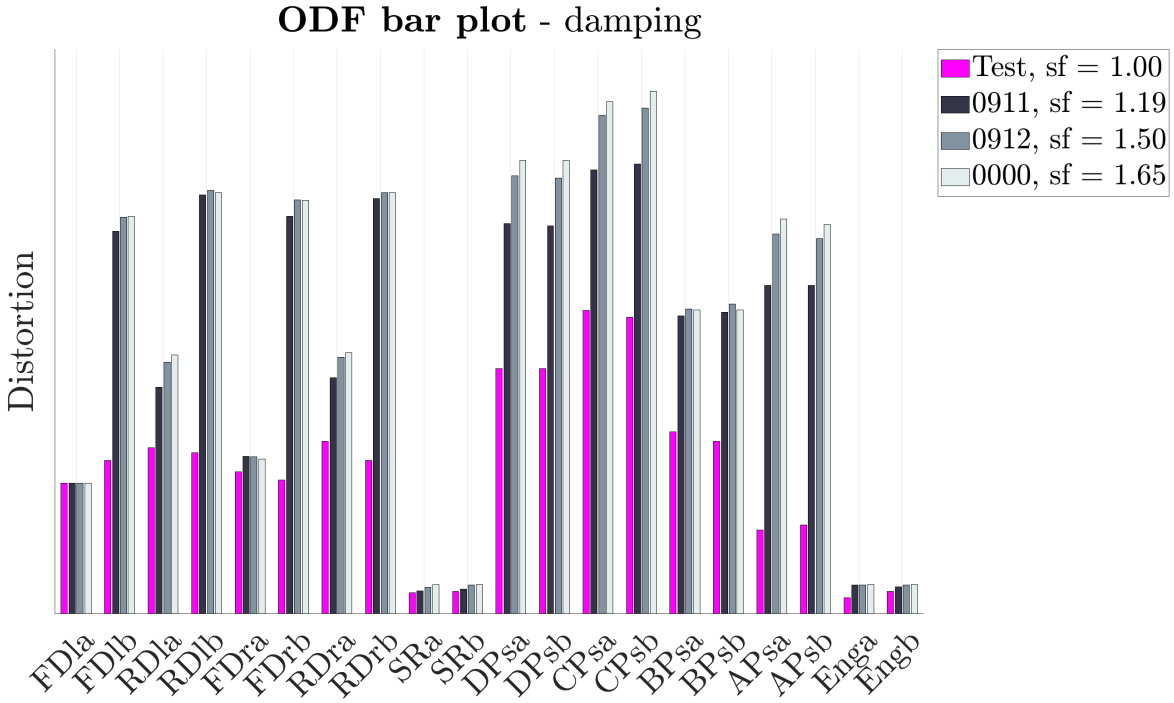

Figure 5.26: ODF results from adjusted damping parameter d_1, i.e. adjusting the constant damping up to 90 Hz. Damping reduced to half the original damping (*0912*) and to a tenth of the original damping (*0911*) along with the base (*0000*) and test data (*Test*). The values are scaled to match the magnitude of FDla. Further description of variants are included in Table 5.1.

If attempts with different damping on different components (or even different damping on different parts of the same component) should be applied, modal damping can no longer be applied to the fully trimmed body. Therefore, applying different damping on different components is considered being a too large violation of the model to be performed within the scope of this thesis work. However, it could be of interest for future research.

5.1.10.2 Changing ramp-up interval

The results from varying the interval during which the damping is increased from the original damping to 100% are presented in Figure 5.27. Considering the NaN-results of variant *0921*, it seems like the ramp-up interval should not be too large. Additionally, from the figure it follows that the results of the different damping intervals *0922-0924* are very similar. Hence it seems like the way in which the damping is ramped up has a negligible impact on the ODF, at least as long as the constant modal damping as for the base model is applied and all high frequencies are completely canceled (100% damping). In Figure 5.28, scaled bars are presented, and the fingerprints are observed to be very similar between the different variants. Noteworthy is that this behavior could for example change for other values of constant modal damping.

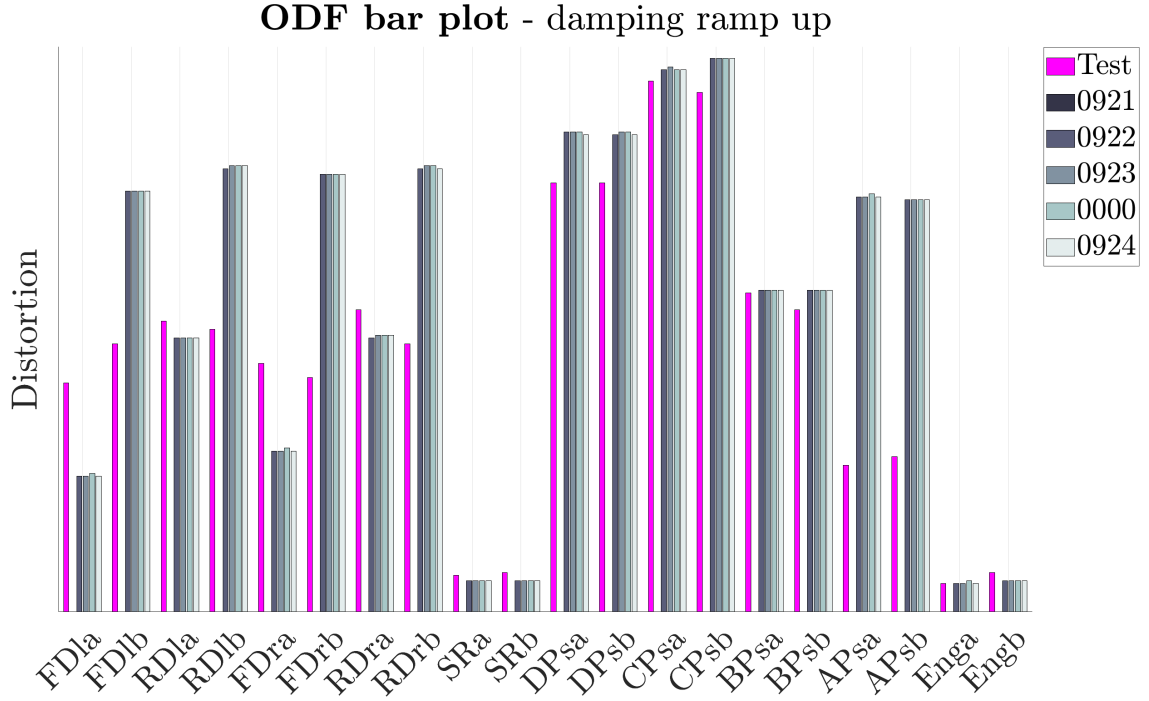

Figure 5.27: ODF results from adjusted ramp-up interval, i.e. adjusting the frequencies f_1 and f_2 from Figure 2.5. Description of variants are included in Table 5.1.

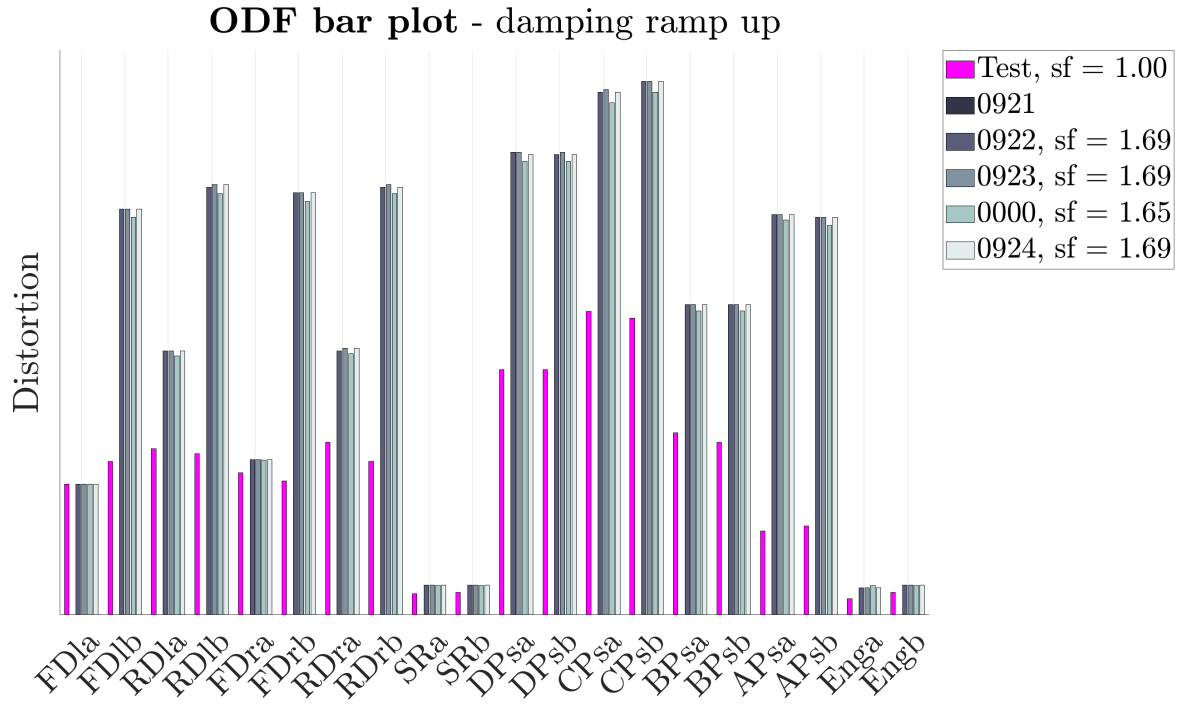

Figure 5.28: ODF results from adjusted ramp-up interval, i.e. adjusting the frequencies f_1 and f_2 from Figure 2.5. The values are scaled to match the magnitude of FDla. Description of variants are included in Table 5.1.

5.2 Opening distortion fingerprint of the test data

Before diving into the results of the parameter study, a few observations from the test data are presented. In Figure 5.29 test data corresponding to different velocities and from different measurement days are presented. From the figure it follows that the distortion is consistently larger for the higher velocity. Another observation, studying the bars corresponding to each velocity, is that there are minor differences in magnitude between the measurements during different days.

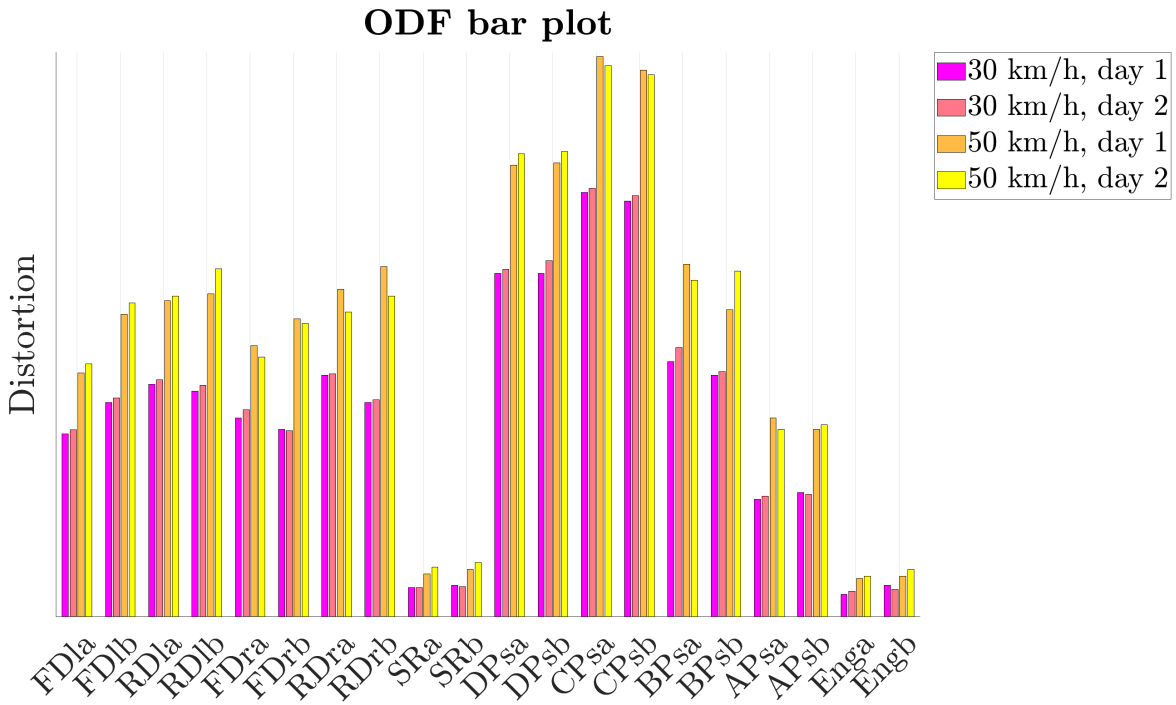

Figure 5.29: ODF of test data at different velocities and different measurements. The different measurements are denoted by *day 1* and *day 2* respectively.

In order to assess how well the fingerprint correlate between the measurements of the different days and the different velocities, the ODF bars have been scaled such that the FDla diagonal is of equal height. The results are presented in Figure 5.30 along with the scale factors used. From the figure it follows that the fingerprint is similar between the different measurements and velocities. The fact that the magnitude differ slightly between measurements of the same speed, indicate the presence of measurement errors. Another possibility would be that the time signal is inaccurately trimmed, see section 5.1.6. However, in total, the bars provide an estimation on the accuracy that can be expected from tests. This accuracy should be considered when comparing the test ODF to the simulation ODFs. The test data from day 1, with the lower velocity, constitutes the reference of test data for the ODF comparison.

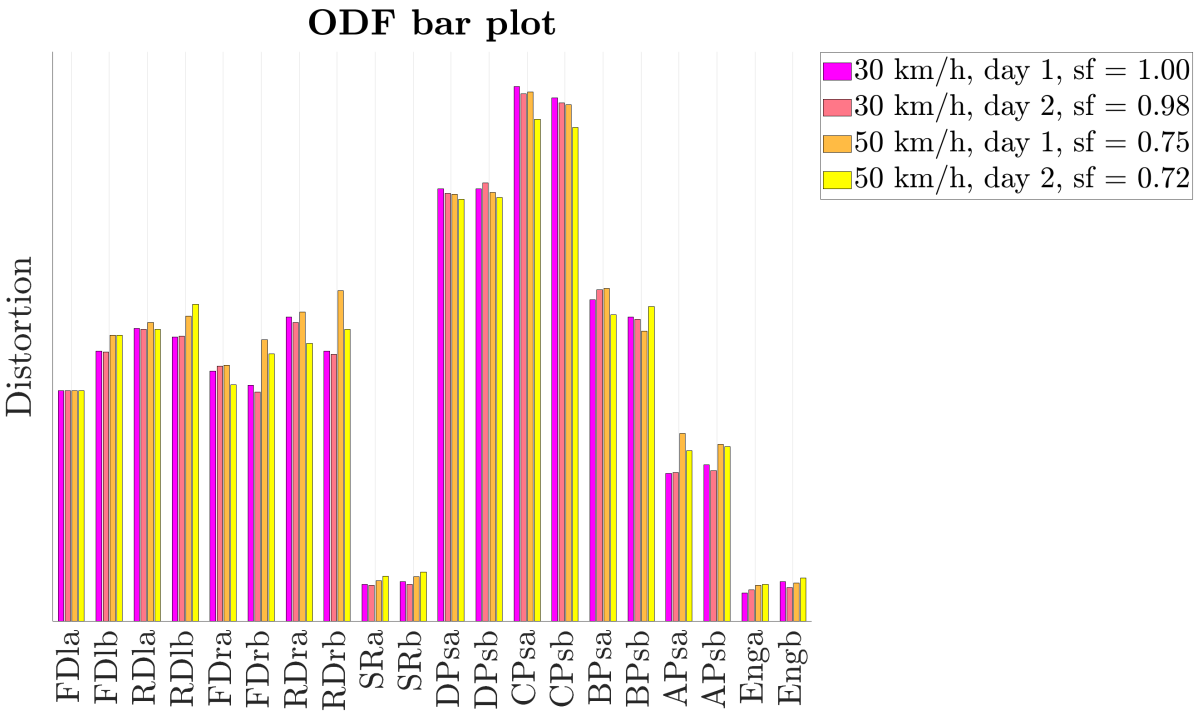

Figure 5.30: ODF of test data at different velocities and different measurements. The different measurements are denoted by *day 1* and *day 2* respectively.

5.3 Final discussion

Some aspects of the individual parameter contributions have been discussed in section 5.1. However, there are more aspects - such as measurement uncertainties, numerical errors, the CMS approach, mode shapes, computational cost, ethical transparency and combination effects - to be discussed within the scope of this thesis.

5.3.1 Measurement uncertainties and numerical errors

In section 5.1.1, differences in the ODF of test and simulation, were observed for most diagonals. In particular, for the ODF of the base model presented in Figure 5.3, only the diagonals over the sunroof and the D-pillar section, show an equal fingerprint when neglecting the magnitude of the bars. However, for the diagonals over the C-, B- and A-pillar sections, the slopes of the fingerprint lines are small. Considering the accuracy of the test data between different measurements presented in Figure 5.30, the difference in slope of the a- and b-diagonals in the test data could be considered within the error margin and hence it could be considered more accurate to draw horizontal lines between the diagonals of the C-, B- and A-pillar sections.

Apart from the test data including measurement errors, the simulated data is affected by numerical errors originating from for example the MNF creation and the ODF toolbars in Meta. The fact that the MNF creation uses ACMS (described in section 2.4.2.2), most likely introduce numerical errors since it constitutes an

approximation of Lanczos method for solving an EVP. Numerical errors are (most likely) introduced in Meta since only eight characters can be stored at the time. The errors from Meta should however exist on both the test data and the simulated data, which could result in equal numerical errors and a negligible effect on the ODF.

Considering the presence of numerical errors in the simulated data, it could be considered more accurate to represent the fingerprint of the C-, B- and A-pillar section diagonals with horizontal lines for the simulated data as well. A representation with horizontal lines of both the test and simulation data would imply a correlation in fingerprint for the C- and B-pillar sections diagonals considering both slope and magnitude. Furthermore, the horizontal representation would imply a correlation in slope of the A-pillar section, even though there are major differences in magnitude. The fingerprint with horizontal lines is presented in Figure 5.31. The diagonals over the doors, however, show similarities in average magnitude, but the slopes of the lines constituting the fingerprint show major differences between the test and simulation. These major differences are too prominent to be considered within the error margin of the measurements.

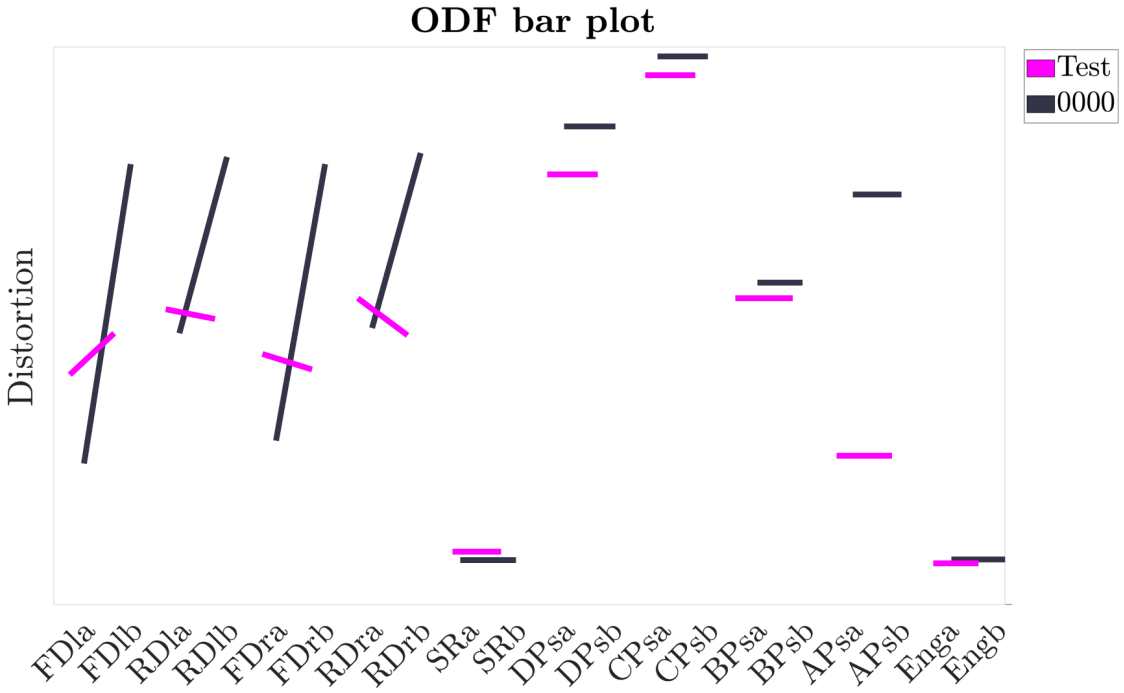

Figure 5.31: ODF of the base model *0000* from Table 5.1 adjusted such that the cross-sectional diagonals are horizontal.

5.3.2 Numerical errors from component mode synthesis

The combination of the fact that the ACMS solver introduces numerical errors and the observation that the doors shows a poorer correlation to the test data than the other diagonals, suggests that either there is an issue with the model setup, or the numerical errors become more prominent on the doors. In relation to this, it

is important to keep in mind that the CMS itself constitutes an approximation of the solution to the full EVP. From the examples of Guyan reduction in section 3.2, follow that the CMS has a major impact on how well the eigenfrequencies can be captured, which could have an impact on how well the simulated ODF correlate to the test data.

The hypothesis of the ability to represent eigenfrequencies corresponds to the ability of capturing eigenfrequencies through CMS, could explain the ODF results of the frequency variation presented in section 5.1.7. Considering the red, yellow, purple and green graphs in Figure 3.12 representing Guyan configuration 1-4, it is observed that the eigenfrequencies from CMS may be far from the analytical eigenfrequencies. Comparing the ability of the Craig-Bampton CMS to capture the eigenfrequencies of the initial configuration in Figure 3.16 to the one in Figure 3.18, indicates that accounting for more modes has a positive effect on the ability to represent eigenfrequencies accurately, but that the ability is also highly affected by the ASET DOFs.

5.3.3 Component mode synthesis and ASET selection

Recall that for the vehicle model, the ASET is fixed since it should be kept physically meaningful. The ASET of the FE model constitute some ppm of the total number of nodes, which suggests that the ability to capture eigenfrequencies without fixed interface modes should be poor, especially for the base simulation where only one mode is accounted for. However, the ODF of the base model and the test data are of similar magnitude and show major similarities for some diagonals such as the C- and B-pillar section diagonals. Hence, the fingerprint correlation between the base model and the test data could be seen as surprisingly good, which in turn could indicate that a Guyan reduction could be accurate. However, when increasing the number of modes the fingerprint changes, see Figure 5.7. The fact that the fingerprint changes unexpectedly when more modes are included in the CMS then contradicts the hypothesis of Guyan reduction being accurately enough to represent the fully trimmed vehicle.

The fact that variant *0102* shows a different fingerprint than the other variants of different maximum frequency for the MNF creation in Figure 5.6, indicate that some modes may include mode shapes canceling each other out. However, without studying the mode shapes, it is impossible to judge whether this is the case. Therefore, further investigation is of interest, see section 6.1.3. Another option would be if there is some kind of transition in the ACMS routine, e.g. the block size, which has an impact on the representation of eigenfrequencies and thereby the number of modes accounted for in the CMS.

5.3.4 Computational time

Considering the computational time for the MNF creation in Table 5.1, the computational cost increases when the number of modes is increased, which is expected since a larger part of the EVP needs to solved. It appears to be a particularly high jump in computational time between variants *0106* and *0102*, which indicates

that there could be a change in computational routine. However, it is considered unlikely that this alone would explain the deviating ODF results of variant *0102*, which suggests that the frequencies and corresponding mode shapes need further investigation.

Accounting for the computational time in Table 5.1 in a more general sense, it can be observed that the the computational cost of creating an MNF is considerably larger than the cost of the MBD simulation. Furthermore it is observed that the computational time of the MBD simulation is almost unaffected by the number of modes included in the MNF. The only exception is variant *0104*, which includes significantly more modes than any of the other variants, and in turn could indicate that the number of modes included in the MNF has a minor impact on the computational cost of the MBD simulation. The minor impact on the computational time makes sense since an MBD simulation is expected to include a considerable amount of rigid bodies. However, in relation to the MBD model used for the thesis work, the minor impact is interesting since the MNF visually constitutes a large part of the vehicle model.

One important observation from the solution of the full EVP for the beam examples (see e.g. Figure 3.12) is that the difference in eigenfrequencies between two constitutive modes is more prominent for flexible modes with low mode numbers. Interesting here is that the Guyan reduced solution can show a similar behavior of a seemingly stable shape with a similar difference between constitutive eigenvalues as observed for the solution of the full EVP, but with the difference that all eigenfrequencies are considerably larger than expected from the full solution, which is the case for e.g. configuration 3 and 4. Other configurations, such as configuration 6, show a considerably more volatile shape with some constitutive eigenvalues of higher mode numbers being very close in magnitude. Interesting in this context is that even though the eigenfrequencies stabilize as expected, they are not necessarily a match to the analytical solution. However, the full solution could show poor correspondence to measured eigenfrequencies since the eigenfrequencies have been highly affected by the discretization (see Figure 3.3(a)).

5.3.5 Ethical aspects of the thesis

In section 1.5, the importance of transparency in the data handling is highlighted. As described in the methodology (see section 4.3), the data has been filtered and integrated through usage of the ODF tool, which since the source code is confidential, reduces the transparency of the operations. Combined with the fact that the data is heavily processed in order to obtain accurate displacements that need even processing in order to obtain an ODF, the usage of the ODF tool transparency could be considered to violate the transparency of the data processing. Nevertheless, the fact that the ODF tool is used could have a positive impact on the reliability of the results since the tool is developed and tested by an experienced company.

Another dimension of the transparency is the usage of industrial softwares in general. However, applying the same reasoning as for the ODF tool, the benefits of having

a tested and developed software should increase the reliability of the calculations instead of being seen as violating the transparency of the study.

5.3.6 Fulfillment of purpose and goal

The purpose of the thesis is, as described in section 1.2, to perform a comprehensive parameter study and investigate what parameters have an impact on the ODF. Below follow a brief discussion how well the purpose and goals of the study have been fulfilled.

5.3.6.1 Evaluation of preparatory goals

The first preparatory goal defined in section 1.3 is to investigate CMS. Through the CMS theory presented in section 2.3 and the beam examples in section 3.2 and 3.3, this preparatory goal is considered being fulfilled.

Understanding of the numerical methods used by the solvers, which constitutes the second preparatory goal, has been gained through the CMS investigation and beam examples thereof. However, in order to deepen the understanding, user guides have been studied. Since the softwares have been developed over more than half a century, the routines are complex and some of them require a thorough mathematical background. With this in mind, there are several aspects of the numerical methods left to understand. Since this is a master thesis in Applied Mechanics, the summary of numerical methods presented in section 2.4.2, is considered to fulfill the second preparatory goal.

The final preparatory goal of gaining understanding of the numerical methods used during post-processing is considered fulfilled through the example of data processing on the physical beam described in section 3.4.

5.3.6.2 Evaluation of goals concerning the parameter study

Moving on to the goals of the parameter study, the first goal is defined to investigate the impact of at least five parameters to the correlation. Considering Table 5.1, ten parameters have been investigated and hence the goal of investigating at least five parameters is viewed as fulfilled. Yet, the parameter study could be expanded by E-line ODFs in the x- and y-directions as a topic of future investigation. Similarly, the second goal of stating the impact of the studied parameters can be considered fulfilled.

The final goal of the thesis work is defined as identifying parameters with major impact on the correlation. This goal can be considered fulfilled in the sense that the impact of each parameter has been stated. However, it has been seen in section 5.1 that none of the studied parameters has a significant impact on the fingerprint of the diagonals corresponding to the doors. Since the diagonals over the doors constitute the largest deviation in the ODF between the base model and test data, the goal of identifying parameters with major impact on the correlation can only be considered being partly fulfilled.

As observed in section 5.1, none of the studied parameters has shown a major impact on the diagonals over the doors. Hence, this major difference in fingerprint, see Figure 5.3, may require further investigation in order to asses whether this is a result of the structural representation or the modeled forces. Although none of the studied parameters individually has shown to significantly impact the fingerprint of the diagonals over the doors, yet the MBD model could be correlated to the test data, but it would require comprehensive investigations on the model setup or a parameter study on combination effects. More suggestions of future investigations are presented in section 6.1.

6

Conclusion

As stated in section 5.3.6, all goals of the thesis work have been treated and at least partly fulfilled. More importantly, most goals are considered to be fulfilled. One observation of the parameter study is that none of the studied parameters changed the fingerprint to be significantly more similar to the fingerprint of the test data. The fingerprint over the cross-sections, the sunroof and over the front of the vehicle are of similar slope as the test data for a majority of the studied parameters. One major difference between the fingerprints of the simulation data and the test data is that the b-diagonals of the doors are of a significantly higher magnitude compared to the a-diagonals of the doors. The magnitude of the b-diagonals have only been affected by the frequency range specified in the ODF tool and the SEP value of variant *0606* gives the most similar slope of the diagonals on the side doors compared to the test data.

The studied parameters are illustrated as a function of adjustment effort and the impact on the ODF in Figure 6.1. On the x-axis, the ODF impact indicates how much the fingerprint is considered to be changed adjusting a certain parameter. The further to the right, the bigger influence on the fingerprint. On the y-axis, the *Adjustment effort* indicates how complicated the parameters is to change. Here, a higher value means that a higher effort is needed. As seen in the figure, the parameters can be divided into the three categories of changes in the *MNF creation*, *Adams modeling* and *ODF tool*. As illustrated, the ODF tool is easiest to change and has a varying impact on the ODF result. All parameters that are changed in the ODF tool only require a few clicks in the interface of Meta, and no extra simulation time. For the changes in Adams, the model must be re-run and hence the effort is increased. The parameters that influence the MNF creation require re-runs of both the MNF creation and the Adams model, therefore the effort is even higher.

For the parameters regarding the MNF creation, the ASET DOFs and the frequency range in the MNF can be changed in the same main file. The battery stiffness is changed in an input file to the main file. Therefore, the adjustment effort is estimated to be similar. In the Adams modeling, small differences in the adjustment effort between the damping ramp-up and the modal damping has been set due to the risk of simulation failures, which has occurred for the variant *0101* in Table 5.1. Changing the damping ramp-up interval and the modal damping require the same amount time and effort by changing a number in a subsystem, but in this study,

an appropriate damping range was slightly harder to find due to the simulation failure of variant *0921*. Thereby, the adjustment efforts in Figure 6.1 alter slightly. Changing tire model is also made in a subsystem, but the change requires another input file. The velocity is considered to have a lower adjustment effort than the other Adams modeling parameters since the velocity must be specified for all runs.

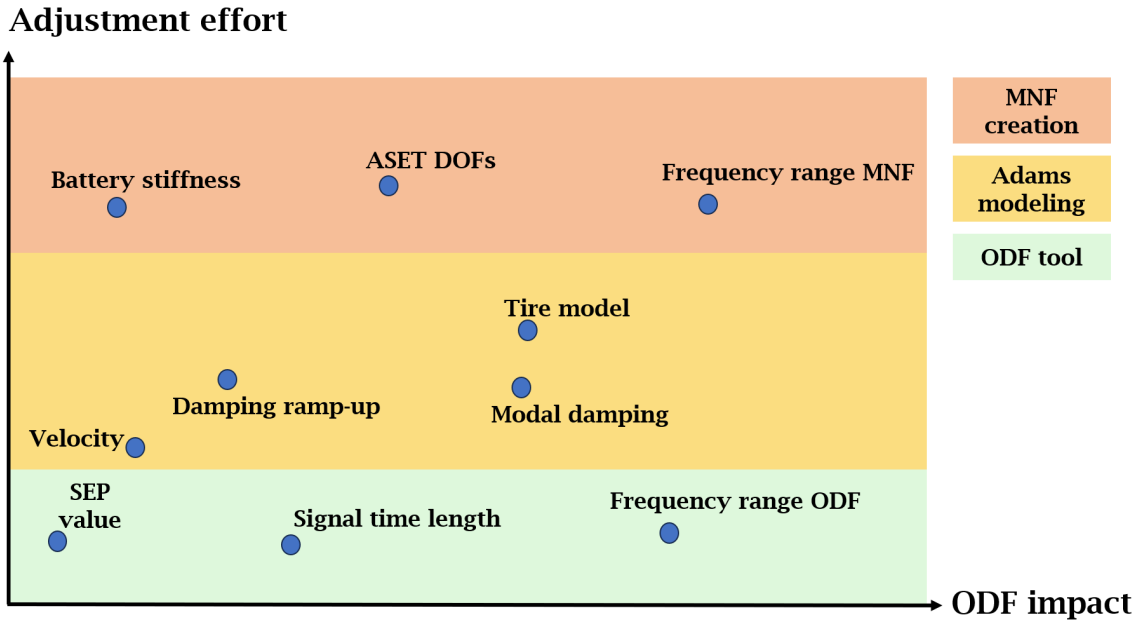

Figure 6.1: Relationship between adjustment effort and ODF impact for the studied parameters.

As presented in Figure 6.1, the parameters in the ODF tool can be changed as a first step, with low adjustment effort, to see if the ODF changes. The parameter with the highest adjustment effort and lowest ODF impact, and therefore least effective parameter to change is the battery stiffness. Changing the frequency range in the MNF is ranked as having the most impact on the ODF, but it also requires a high adjustment effort.

6.1 Future research

With the constrained time frame of the project and the defined demarcations, several aspects of future correlation can be more thoroughly treated. Examples of such aspects are how the simulation model is built up, the model stiffness, the tire model, combination effects, used CMS and the frequency range in the ODF tool. Another interesting aspect of the correlation of the test vehicle and the simulation models may be to find the reason behind the differences in magnitude for the b-diagonals of the doors. It could also be of interest to broaden the study to include the x- and y-direction in the ODF evaluation, and also analyze the model in the so-called operational deflection shape (ODS) tool in Meta. Through the ODS tool, the motion of the vehicle at different frequencies can be studied. The proposed investigations could advantageously be performed on a simpler model before moving on to the full model.

6.1.1 Simulation modeling

How the MBD model is built up could be considered as a future investigation of the parameters study. The MBD model is affected by the architecture of the MBD model and the FE model used for the MNF creation. As seen from the beam example in section 3.1, the discretization of the model may affect the eigenpairs and thereby the response, which in turn may affect the ODF. Some modes may be captured better or worse depending on the mesh and which type of modes that should be captured considering the specifications of the MNF creation file. For example, a mode that includes the entire vehicle may require a coarser mesh than a mode on one, single component. The meshing constitute a significant part of the FE model, but the meshing also affects the MBD model since it consists of flexible parts. Since the MBD model contains flexible parts it could be affected by the meshing. However, this is outside the scope of the thesis and has therefore not studied, but it could be of interest for future investigations.

In addition to the meshing of the models, other attributes could be investigated further. Since, for example, the b-diagonals of the doors show significant differences compared to the test data, the stiffness in different parts of the model could be examined. The stiffness may be a part of both the FE model and the MBD model. Considering that vehicles without b-pillars are less commonly simulated, there could be challenges in the modeling approach. Another attribute is the damping of the models. As seen in Figure 5.25, the damping may affect the fingerprint. Although damping may be difficult to correlate, it could be of interest to see how a more thorough damping investigation may impact the ODF results.

Furthermore, usage of a tire model that does not correspond to the tires used in measurements, may have an influence on the ODF. As seen in Figure 5.21, the magnitudes changed for a different tire model. For the studied tire models, the magnitudes were scaled, which illustrates a minor impact on the actual fingerprint. It should be mentioned that even if the tire model represents the tires used in measurements, there may still be uncertainties whether the tire model is representative. However, being able to further correlate the model with correct tire models, could result in a better correlation.

6.1.2 Combination effects of parameters

To build on the findings from the parameter study and examine whether a combination of parameters have au unexpected effect on the ODF, combined simulations should be run. Combination effects between parameters could appear, and therefore it should be recalled that it may result in a non-linear relation of the ODF, i.e. the fingerprint may change. Since none of the parameters studied here has a significant impact on the door diagonals, combination effects could be a next step for further understanding of how the parameters impact the results. In order to perform a study of combination effects in a structured way, a statistical design of experiments could be used.

6.1.3 Understanding eigenmodes

A better understanding of how the flexible modes used in the MNF affect the modeling is also important. In Figure 5.7, the impact of the frequency range in the MNF is seen. Recall that the variant *0102* gives a different pattern than the other variants. To be able to understand what happens at the frequencies included in the MNF of variant *0102*, illustrations of the modes could be beneficial. One way to observe how the vehicle behaves is the ODS tool in Meta. The ODS can illustrate how the vehicle behaves at different frequencies and may therefore be used to find potential aberrations in the model.

From the measurements, the different mode shapes may be further reviewed and compared to the models to investigate how well the simulation models correspond to the test vehicle. This applies to both the full model and the reduced model in the MNF. From test data on what frequencies the different modes have, comparison with the digital models could be considered. A visual comparison may be performed in Meta or Adams directly, but also in the ODS tool in Meta. By comparing the test vehicle and a reduced model, the reduced frequencies and mode shapes may be confirmed. If the modes and frequencies of the reduced model differ from the ones of the test vehicle, the CMS methods may require further investigation. It may also be of interest to study both local and global modes to see if specific modes are harder to capture in the modeling. Local modes refer to modes were only few components are moving, while global modes refer to movement of the entire vehicle. Specifically, it would be of interest to see if the doors show major differences in frequency and mode shape since the b-diagonals of the doors in the ODF show major differences between test and simulation. Studying the motions of the simulation model may also hint on whether the doors are accurately modeled.

In addition to the CMS and ODS investigations, strangely behaving modes can be disregarded in Adams. Neglecting modes that exist in the MBD simulation, but not in real-world tests could improve the correlation. However, this is time-consuming since it require visual inspection of each mode for every model change.

6.1.4 Input to the opening distortion fingerprint tool

Since the frequency range has shown to affect the ODF, it might be worth expanding the study on wether the ODF results change for a different frequency range. With a smaller frequency range for both the simulation data and the test data, the differences in magnitude in the ODF may be identified for a different frequency range than the primarily studied one in this report. If the unexpectedly high magnitudes of the b-diagonals of the doors of the base model are found for a smaller frequency range, the problems with the model may be found as being foremost at higher or lower frequencies. This may facilitate a correlation between the test data and the simulation model. In particular, from the parameter study follows that the frequency range $25 - 30$ Hz is of interest. When comparing simulation and test data, RBMs should be kept in mind for lower frequencies. There could be influences of RBMs, especially in the tests. If RBMs are captured, they result in so-called artificial displacements, see section 2.6, that may misrepresent the results.

When the frequency where the first structural mode occur is located, the frequency range in the ODF may be more accurately chosen. With a more accurately defined lower frequency in the ODF tool, other behaviors than observed in this study could appear. The difference is that the lower cut-off frequency in the ODF tool for this study is purposely set to be higher than the RBMs in oder to avoid capturing so-called artificial displacements.

Lastly, the resulting ODF could also be studied in the x- and y-directions. Some benefits of an expansion of the study in all directions could be that the differences in the fingerprint may be found in multiple directions. If the correlation problems are identified to originate from a certain direction, it may be easier to detect the root of the problem. The problems may also be present in all directions, but the results could still be of use when breaking down the problem. In the best of worlds, the observed error in the z-direction could be canceled out by errors in the x- and y-directions.

6.1.5 Different methods of component mode synthesis

Moreover, the CMS method used for creating the MNF could be further investigated. Creating an MNF with a different CMS may result in a different fingerprint since the reduction may be performed in another way. For this study, the creation of the MNF could, for example, be performed without using ACMS. It would, most likely, result in a longer simulation time since ACMS is supposed to be 100 times faster than a regular Lanczos according to [18], but the reduction could then be made with less approximations. In addition to a longer simulation time, it may also occur difficulties with simulating the model without ACMS due to the model complexity, but it could be worth a run. To start with, a smaller model may also be used to find potential differences between different CMS methods to understand how it may impact the full model.

Other CMS investigations may also be performed on the fully trimmed body. It was for example seen in the beam examples of Guyan reduction (see section 3.2) and Craig-Bampton reduction (see section 3.3) that the ASET distribution and the fixed interface modes included in the reduction matrix affect how well the frequencies can be captured. Therefore, a review of the ASET definition, and possibly re-defining which nodes to constitute the interface, could be of interest. However, re-defining the ASET is a considerable violation of the model set-up, but it could be considered as a last resort.

Bibliography

[1] Aiyan, M., Sagar, S., and Raghav, S. "Design and Optimization of an Electric Car Chassis and Body using Structural Analysis and CFD". In: *Research Square* (2021). DOI: 10.21203/rs.3.rs-575396/v1.

[2] BETA CAE Systems. *Ansa 25.01*. 2024.

[3] BETA CAE Systems. *Meta 25.01*. 2024.

[4] BETA CAE systems. *Vehicle stiffness evaluation with the Opening Distortion Fingerprint (ODF) method*. 2021. URL: https://www.beta-cae.com/pdf/opening_distortion_fingerprint.pdf (visited on 03/20/2025).

[5] Boström, A. *Rigid body dynamics*. Unpublished. School of Mechanics and Maritime Sciences, Chalmers University of Techology. 2018.

[6] BY JU'S. *Galilean Transformation*. URL: https://byjus.com/physics/galilean-transformation/ (visited on 03/04/2025).

[7] Chalmers University of Technology. *Genomföra kandidatarbete*. 2022. URL: https://www.chalmers.se/utbildning/dina-studier/kandidat-och-examensarbete/kandidatarbete/genomfora-kandidatarbete/#samhalleliga-och-etiska-aspekter (visited on 04/27/2025).

[8] Datatas. *The Role of AI in Reducing Bias in Large-Scale Big Data Models - Datatas*. 2025. URL: https://datatas.com/the-role-of-ai-in-reducing-bias-in-large-scale-big-data-models/ (visited on 04/27/2025).

[9] European Commission. *Electric vehicles - European Commission*. URL: https://transport.ec.europa.eu/transport-themes/clean-transport/clean-and-energy-efficient-vehicles/green-propulsion-transport/electric-vehicles_en (visited on 04/27/2025).

[10] European Commission. *High-level expert group on artificial intelligence | Shaping Europe's digital future*. 2024. URL: https://digital-strategy.ec.europa.eu/en/policies/expert-group-ai (visited on 04/27/2025).

[11] European parlament. *Självkörande bilar i EU: från science fiction till verklighet*. 2019. URL: https://www.europarl.europa.eu/topics/sv/article/

20190110STO23102/sjalvkorande-bilar-i-eu-fran-science-fiction-till-verklighet (visited on 04/27/2025).
[12] Flodén, O., Persson, K., and Sandberg, G. "Reduction methods for the dynamic analysis of substructure models of lightweight building structures". In: *Computers & Structures* 138 (2014), pp. 49–61. ISSN: 0045-7949. DOI: https://doi.org/10.1016/j.compstruc.2014.02.011.
[13] Géradin, M. and Rixen, D. *Mechanical Vibrations*. 2nd ed. New York: Wiley, 1998. ISBN: 0-471-97524-9.
[14] Hexagon. *ACMS User's Guide*. 2022.
[15] Hexagon. *Adams Flex User's Guide*. 2023.
[16] Hexagon. *Generating Flexible Bodies in Adams View Environment*. URL: https://simulatemore.mscsoftware.com/generating-flexible-bodies-in-adams-view-environment/ (visited on 02/27/2025).
[17] Hexagon. *High Performance Computing User's Guide*. 2021.
[18] Hexagon. *High-Performance Computing with MSC Nastran*. URL: https://hexagon.com/resources/resource-library/high-performance-computing-with-msc-nastran (visited on 03/26/2025).
[19] Hexagon. *MSC Adams 2019.2*. 2019.
[20] Hexagon. *MSC Nastran 2014 Quick Reference Guide*. 2014.
[21] Hexagon. *MSC Nastran 2021.1 Numerical Methods User's Guide*. 2022.
[22] Hexagon. *MSC Nastran 2023.4 Dynamic Analysis User's Guide*. 2023.
[23] Hexagon. *MSC Nastran 2024.1*. 2024.
[24] Hourdry, R. *Français : Le secteur pavé*. 2018. URL: https://commons.wikimedia.org/wiki/File:Avesnes-le-Sec_Secteur_pav%C3%A9.jpg (visited on 02/05/2025).
[25] Jansson, P-Å., Grahn, R., and Enelund, M. *Mekanik*. 4th ed. Lund: Studentlitteratur, 2019.
[26] Korhogo. *Rare Earth Elements and Their Role in High-Performance Batteries*. 2024. URL: https://korhogominerals.com/rare-earth-elements-and-their-role-in-high-performance-batteries/ (visited on 04/28/2025).
[27] M. L. Soni. "A superelement component dynamic synthesis method". In: NASA. Marshall Space Flight Center, The 58th Shock and Vibration Symposium, 1988.
[28] Meriam, J. L., Kraige, L. G., and Bolton, J. N. *Engineering Mechanics Dynamics*. 8th ed. Vol. 2. John Wiley & Sons Singapore Pte. Ltd, 2013. ISBN: 978-1-119-04481-9.
[29] MSC Software. *Dramatic productivity improvements for large dynamic analysis problems*. 2003. URL: https://www.mscsoftware.co.kr/upfile/pro_pdf/Nastran%20ACMS_604.pdf.
[30] *Nexus Documentation Center*. URL: https://nexus.hexagon.com/documentationcenter/en-US/bundle/adams_2022.4/page/adams_help/Adams_Advanced_Package/flex/flex_welcome/TOC.About.Adams.Flex.xhtml#XREF_37386_About_the_Flexible (visited on 01/24/2025).

[31] *Powering the future of electric mobility.*
URL: https://www.zeekrtech.eu (visited on 01/22/2025).

[32] *Pure Electric Vehicle Brand | Zeekr.*
URL: https://www.zeekr.eu/about (visited on 01/22/2025).

[33] R. R. Craig, Jr. and C. J. Chang. "A REVIEW OF SUBSTRUCTURE COUPLING METHODS FOR DYNAMIC ANALYSIS". In: NASA. Langley Res. Center Advan. in Eng. Sci., Vol. 2, 1976.
URL: https://ntrs.nasa.gov/api/citations/19770003325/downloads/19770003325.pdf (visited on 05/03/2025).

[34] Svenska FN-förbundet. *Globala målen för hållbar utveckling.* 2023.
URL: https://fn.se/globala-malen-for-hallbar-utveckling/ (visited on 04/27/2025).

[35] T. Abrahamsson. *Structural Dynamics and Linear Systems Compute, Test, Calibrate and Validate.* 2019.
CHALMERS UNIVERSITY OF TECHNOLOGY, 2019.

[36] VDI-Gesellschaft Fahrzeug- und Verkehrstechnik, ed.
SIMVEC, aktuelle Herausforderungen bei der Auslegung und Absicherung von Fahrzeugsystemen: 20. VDI-Kongress mit Fachausstellung ; Baden-Baden, 22. und 23. November 2022. VDI-Berichte 2407.
Düsseldorf: VDI Verlag, 2022. ISBN: 9783181024072 9783180924076.

[37] Weber, J. et al. "A New Equivalent Static Load (ESL) Creation Procedure for Complete Vehicle". In: Graz, Austria, 2024.
DOI: 10.4271/2024-01-2944.

[38] Weber, J. et al. "Opening Distortion Fingerprint (ODF) - A New Body Evaluation Method for Perceived Quality and Vehicle Dynamics". In: 2022.
DOI: 10.4271/2022-01-0950.

[39] Zeekr. *Pure Electric Vehicle Brand | Zeekr.*
URL: https://www.zeekr.eu/sv-se (visited on 04/27/2025).

A

MAC

A.1 All DOFs considered in ASET, Guyan reduction

Mode number	Translation	Rotation	Total MAC
1	1.00	1.00	1.00
2	1.00	1.00	1.00
3	1.00	1.00	1.00
4	1.00	1.00	1.00
5	1.00	1.00	1.00
6	1.00	1.00	1.00
7	1.00	1.00	1.00
8	1.00	1.00	1.00
9	1.00	1.00	1.00
10	1.00	1.00	1.00
11	1.00	1.00	1.00
12	1.00	1.00	1.00
13	1.00	1.00	1.00
14	1.00	1.00	1.00
15	1.00	1.00	1.00
16	1.00	1.00	1.00
17	1.00	1.00	1.00
18	1.00	1.00	1.00
19	1.00	1.00	1.00
20	1.00	1.00	1.00
21	1.00	1.00	1.00
22	1.00	1.00	1.00
23	1.00	1.00	1.00
24	1.00	1.00	1.00
25	1.00	1.00	1.00
26	1.00	1.00	1.00
27	1.00	1.00	1.00
28	1.00	1.00	1.00
29	1.00	1.00	1.00
30	1.00	1.00	1.00
31	1.00	1.00	1.00
32	1.00	1.00	1.00

A.2 All fixed-inteface modes included in Craig-Bampton reduction

Mode number	Translation	Rotation	Total MAC
1	0.61	0.70	0.12
2	0.35	1.00	0.86
3	1.00	1.00	1.00
4	1.00	1.00	1.00
5	1.00	1.00	1.00
6	1.00	1.00	1.00
7	1.00	1.00	1.00
8	1.00	1.00	1.00
9	1.00	1.00	1.00
10	1.00	1.00	1.00
11	1.00	1.00	1.00
12	1.00	1.00	1.00
13	1.00	1.00	1.00
14	1.00	1.00	1.00
15	1.00	1.00	1.00
16	1.00	1.00	1.00
17	1.00	1.00	1.00
18	1.00	1.00	1.00
19	1.00	1.00	1.00
20	1.00	1.00	1.00
21	1.00	1.00	1.00
22	1.00	1.00	1.00
23	1.00	1.00	1.00
24	1.00	1.00	1.00
25	1.00	1.00	1.00
26	1.00	1.00	1.00
27	1.00	1.00	1.00
28	1.00	1.00	1.00
29	1.00	1.00	1.00
30	1.00	1.00	1.00
31	1.00	1.00	1.00
32	1.00	1.00	1.00

B

Additional figures

B.1 Craig-Bampton - include more modes and changing ASET distribution

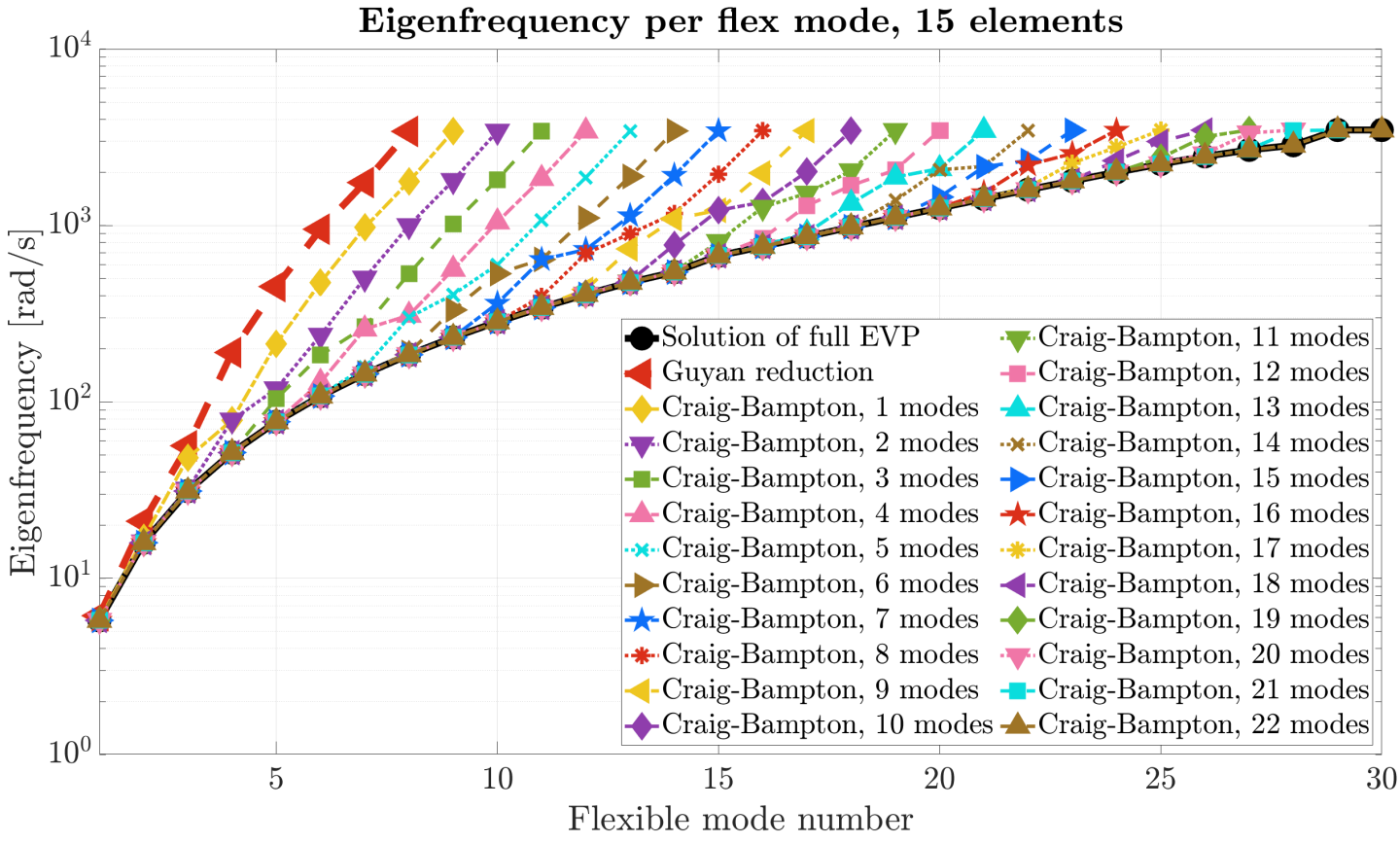

B.2 Craig-Bampton - include more modes and changing ASET distribution

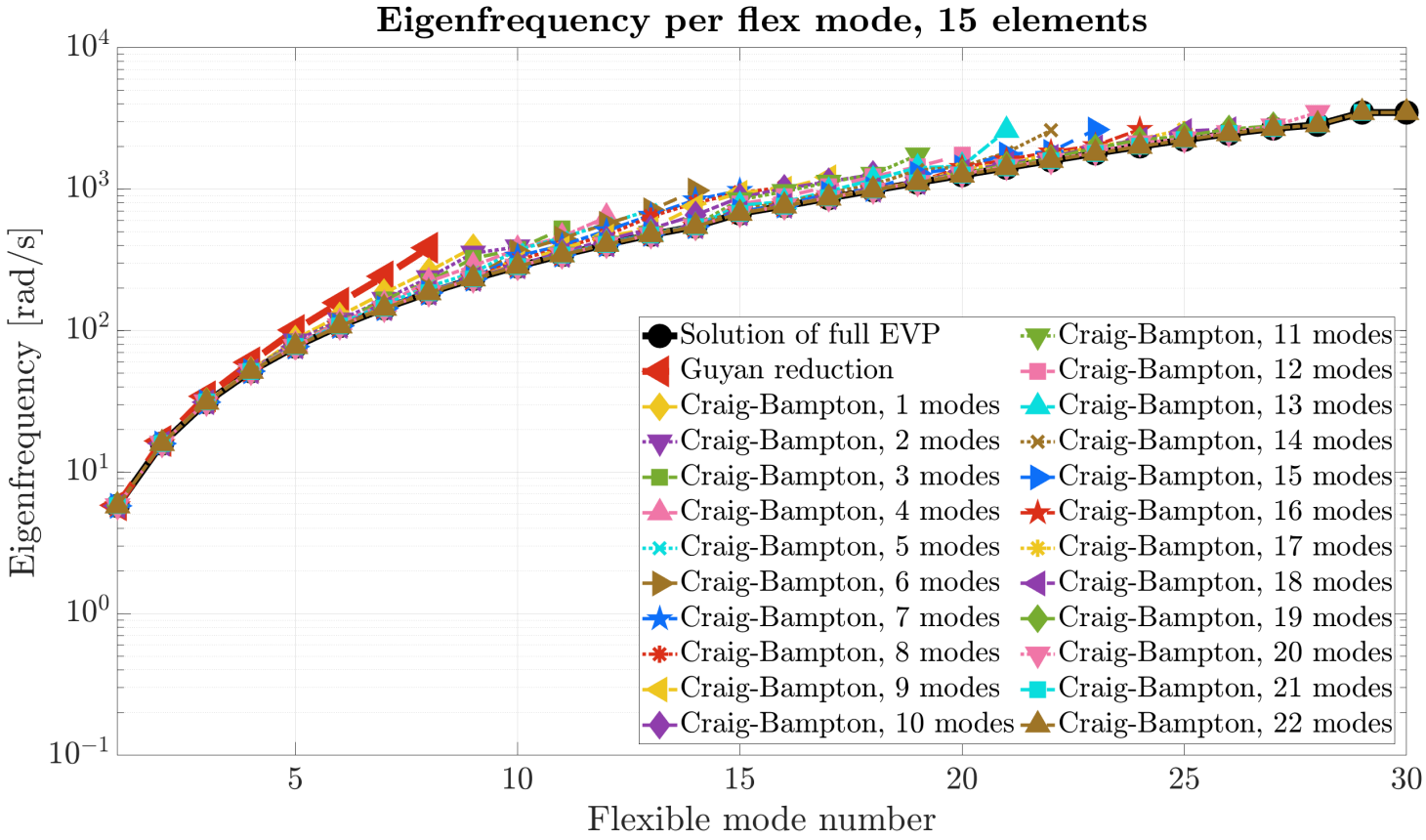

DEPARTMENT OF MECHANICS AND MARITIME SCIENCES
CHALMERS UNIVERSITY OF TECHNOLOGY
Gothenburg, Sweden 2025
www.chalmers.se

CHALMERS
UNIVERSITY OF TECHNOLOGY